ELECTROMAGNETIC SENSORS FOR MEASUREMENTS ON ELECTRIC POWER TRANSMISSION LINES

By

ZHI LI

A dissertation submitted in partial fulfillment of
the requirements for the degree of

DOCTOR OF PHILOSOPHY

WASHINGTON STATE UNIVERSITY
School of Electrical Engineering and Computer Science

AUGUST 2011

To the Faculty of Washington State University:

The members of the Committee appointed to examine the dissertation of ZHI LI find it satisfactory and recommend that it be accepted.

_____

Robert G. Olsen, Ph.D., Chair

_____

Patrick D. Pedrow, Ph.D.

_____

Mani V. Venkatasubramanian, Ph.D.

ACKNOWLEDGMENT

I would like to thank my advisor Dr. Robert G. Olsen for his endless help during my stay in Pullman. He ignited my interest in the research on electromagnetics for power transmission lines. His patient and inspiring guidance always brought me back on the right track when I got lost in my research. Without his help and encourage, this dissertation would not have been possible. Also thanks to his mentoring of my life under the American culture background. I would like to thank my committee, Dr. Patrick D. Pedrow and Dr. Mani V. Venkatasubramanian for the helpful inputs for my research and career pursuits. Special thanks to, but not limit to, Dr. Anjan Bose, Dr. John B. Schneider, and Dr. Aleksandar D. Dimitrovski for help in my research and graduate curriculum.

I would also like to thank my parents and my family for their continuous support and unconditional love, which have always been the source of my courage. Deepest appreciation also to my friends, whose support and encourage have helped shape this amazing journey in my life.

Thanks to Xiaojing for holding my hand, with love.

ELECTROMAGNETIC SENSORS FOR MEASUREMENTS ON

ELECTRIC POWER TRANSMISSION LINES

Abstract

by Zhi Li, Ph.D.
Washington State University
August 2011

Chair: Robert G. Olsen

The emergence of smart grid technology requires changes in the infrastructure of the electric power system. One of these changes is the addition of sensors to the transmission portion of the power system in order to determine useful information about the system such as line sag and direction of power flow. Unfortunately, there are a number of inhibitors to incorporating these additional sensors. These include issues of initial cost and/or maintenance. Therefore, what is needed (especially in sparsely inhabited areas) is new sensors that are inexpensive to manufacture, do not compromise safety, can be installed without taking transmission lines out of service and require low levels of maintenance.

The focus of this dissertation is on electromagnetic (EM) field sensors, a novel type of sensor that can be used for monitoring the state of power lines. These sensors do not require contact with the power lines; rather they utilize electric and magnetic field coupling. Important states (such as voltage, current and phase sequence) and geometric parameters (e.g., line sag) of the power lines can be monitored based on

inherent correlations between those variables and the electromagnetic fields produced by the power lines. While similar sensors have been available for many years, the unique feature of the sensors discussed here is that they utilize the relative phase of the EM fields in the vicinity of the line to provide significantly better sensitivity than has been previously available. In addition, they are inexpensive, easy to install with live working techniques and require only a low level of maintenance.

Three types of sensors, point probes, and perpendicular and parallel distributed sensors will be studied using basic reciprocity theory and developed to the point of application. Several field experiments were conducted for validation. Finally, potential applications of the sensors for monitoring power lines are explored.

TABLE OF CONTENTS

Page

LIST OF FIGURES

LIST OF TABLES

To my mother and father

CHAPTER 1

INTRODUCTION

Since the commercial electric power system started to serve our society in late 1800's, the transmission line has become a significant part of the system. After more than 100 years' development, the modern power system is much more advanced than its ancestor. When the first transmission line in North America was built in 1889, it was only about 13 miles long and delivered power from Willamette Falls in Oregon City to downtown Portland at a voltage of 4000 V [1]. Nowadays, high voltage transmission lines can convey huge amounts of power over hundreds or even thousands of miles from the generation center to the consumer center. Many kinds of devices and sensors are installed to monitor the flow of power through the transmission line and ensure that the power system is operated efficiently as well as reliably. These sensors also play important roles in providing the protection for the power system during abnormal operations and faults. The sensor itself is a testing field for the state-of-art technologies. Many high-tech methods or concepts, such as robotics, GPS technique, and radar imaging, have been adapted in developing the sensors and significantly improve the performance of the sensor network for the power system.

With all these efforts, however, power engineers still cannot help asking this question: Is it enough to operate a reliable, smart as well as economically efficient electric power system? Obviously, the answer is No. Here the focus is on the transmission line system. Fig. 1-1 shows the basic structure of a power system,

containing the subsystem of, from left to right, power generation, transmission, and distribution.

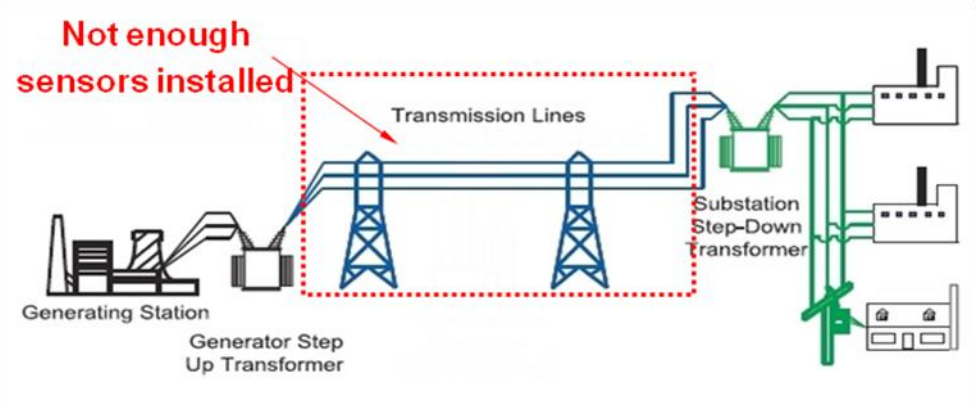

Fig. 1-1 Structure of a typical power system, usually not enough sensors are installed for the transmission lines (Image source: http://www.ferc.gov/industries/electric/indus-act/reliability/blackout/ch1-3.pdf)

As well known, the traditional sensors such as potential transformers (PT's) and current transformers (CT's) are usually installed in the substations. However, on the power transmission lines (shown in the dashed square in Fig. 1-1), which are often spread out over wide areas, an inadequate number of sensors have been deployed. There is useful information, such as line sag, direction of power flow, and environmental electromagnetic field, that are not well monitored in these areas. In the Department of Energy's "Five-year program plan for fiscal years 2008 to 2012 for electric transmission and distribution programs" [2], it is proposed to deploy at least 100 transmission-level sensors by 2009 to enhance the capability of real-time monitoring of the power system. The "transmission-level sensors" in this report include phasor measurement units (PMUs), intelligent electronic devices (IEDs) and sag monitors. It is reported that prior to 2009, more than 200 PMUs have been installed in the North American power system interconnection with more to come [3].

Obviously, compared to the scale of the power system, several hundred sensors are far from enough to significantly improve the sensor networks for the transmission system of the power grid. It is cost which limits the number of the sensors to be installed. Those sensors are usually very expensive and require many of labor hours for installation and maintenance.

Moreover, it has been the common understanding that the 'Smart Grid' will be the future of the electric power system. To build a smarter power system requires reform of the infrastructure, for which the sensor network is an important part. Instead of changing all the existing grid at once, the better and more feasible idea is to gradually replace the old components with new technologies and, at the same time, improve the ability to access and monitor the conditions of the rest of the grid components so that it operates more efficiently and reliably [4], [5]. This brings technical and economic challenges to advancing the sensor networks. The types of sensors chosen for the new sensor networks should have the following characteristics:

- Capable of picking up the desired signals under complicated background conditions, accurately and reliably;
- Inexpensive for manufacture and maintenance;
- Easy and safe to install.

Especially for power transmission lines, which are geographically widely spread in sparsely inhabited areas, the sensors should be inexpensive, easy to install with live line work, and require a very low level of maintenance. Given these characteristics, the sensors can be deployed in large numbers to significantly increase the density of

the sensor networks for transmission system of the power grid.

New sensors and sensing technologies have been developed for transmission lines. For example, a conductor temperature sensor and a connector condition sensor are introduced in [4]. The first sensor measures the conductor temperature and current directly. The second one monitors the condition of the conductor connectors by measuring temperature or resistance of the connector. Sensors based on fiber-Optic and infrared imaging techniques have been used for measuring the leakage current and contamination level of insulators on transmission lines [6] – [9]. [10] shows the automatic visual power line inspection conducted by a robot equipped with cameras. Real-time sag monitoring of the power line conductors is important for the dynamic rating of power lines; they detect dangerous increases in line sag due to overheating or ice covering, and prevent line to ground short circuit faults. Power line sag can be measured by several types of sensors or techniques, such as satellite imaging [11], power-line carrier (PLC) signal analysis [12], global positioning system (GPS) sensor [13], [14], mechanical tension sensor [15], or space potential probe [16], [17].

1.1 Electromagnetic sensors for transmission lines

The sensors to be studied in this dissertation are ones that achieve the desired measurements by means of electromagnetic (EM) coupling with the fields produced by power transmission lines. Basically, these sensors (will be called the ‘EM sensors’ in the dissertation) are the receiving antennas that work with the EM fields due to the power transmission lines. The first pair of transmitting and receiving antennas,

employed by Hertz in 1887, had a very simple design [18]. The receiving antenna was simply formed by a circular loop of wire with a tiny gap. The EM sensors introduced here inherit the characteristic of simplicity from Hertz's antennas. It is not necessary to have complex structures, which means the manufacturing costs are low. In fact, a simple conducting sphere or a loop of conductor can be used as an EM sensor for acquisition of useful information from power lines. An EM sensor made of a styrofoam sphere covered by aluminum foil and the supporting frames made of PVC pipes are shown in Fig. 1-2. When grounded through an ammeter, this sensor can be used to measure the space potential, i.e., the capacitive coupling, due to the power lines. Details of this kind of sensor will be introduced in Chapter 2.

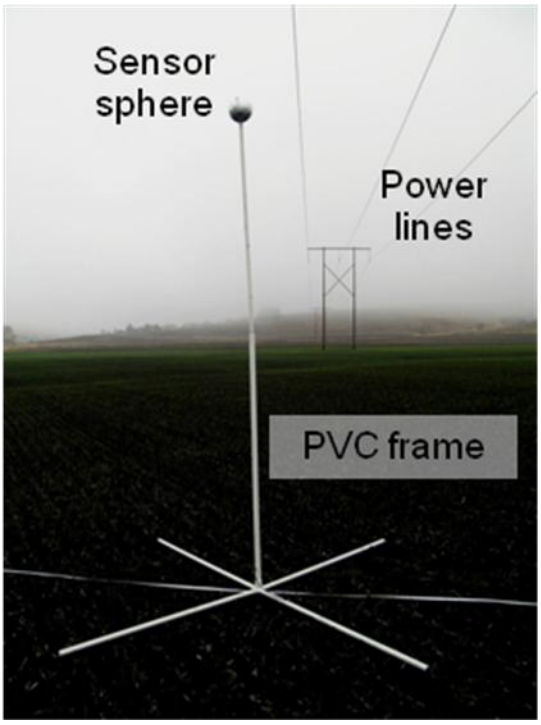

Fig. 1-2 An EM sensor made of styrofoam sphere covered by aluminum foils and the PVC supporting frame

Since the EM sensors work with the EM fields due to the power line, the measurements can be conducted in a non-contact manner, which means that the

sensors don’t have to have physical contact with the power line conductors and can be placed relatively far away from the high voltage parts. This avoids concerns about high voltage insulation, and further, reduces the manufacture costs of the sensor system. The EM sensors with the corresponding meters, data storage, and even communication system still cost much less than many other kinds of sensors in use, such as PTs, CTs, or GPS sag monitors. Benefiting from the non-contact characteristics of the EM sensor, the installation becomes simple and inexpensive. Further, the power line doesn’t need to be shut down when the EM sensor is installed because it is placed far enough (usually on the ground) from the power line conductor.

Usually, the result of the electromagnetic coupling from power lines are the induced current or voltage on the EM sensors. The EM fields due to power lines are determined by the variables such as line voltage, current, and line configuration, which are all very useful pieces of information about the operation and control of the power system. Inherent connections are consequently built between the induced current or voltage and the states or parameters of the power lines. Then, these pieces of information about the power lines can be derived, i.e., indirectly measured, by the measurements from the EM sensor. This is the basic mechanism how the EM sensors work. Therefore, the EM sensors have the ability to accomplish many tasks now done by the traditional sensors. Different from the traditional measurements of EM fields for which only the magnitudes of the fields are measured, the utilization of the phase angle of the fields gives more strength to the EM sensors discussed here, if properly designed. In addition, the EM sensors, with simple design and structure, require very

low level of maintenance, which results in that the sensors can be installed in various areas, including those far away from the population centers. All these advantages imply that the EM sensors have the potential to be deployed in large number in the power transmission system and make the family of EM sensors a good choice for advancing the sensor network for power transmission lines.

The designs of EM sensors vary between different applications. Each kind of the EM sensor is designed to measure the desired variables or states. The types of EM sensors to be studied in this dissertation are the point probes (capacitive coupling sensors), perpendicular linear sensors (capacitive coupling sensors), and parallel linear sensors (capacitive and inductive coupling sensors).

1.2 EM fields due to power transmission lines

As is well known, in the vicinity of an energized power transmission line there exist electromagnetic fields. Though it is usually difficult (if not impossible) for humans to directly perceive the existence of these fields, well-designed sensors can help to detect and measure them. Fig. 1-3 illustrates the patterns of the transverse electric and magnetic field fluxes of a two-conductor transmission line.

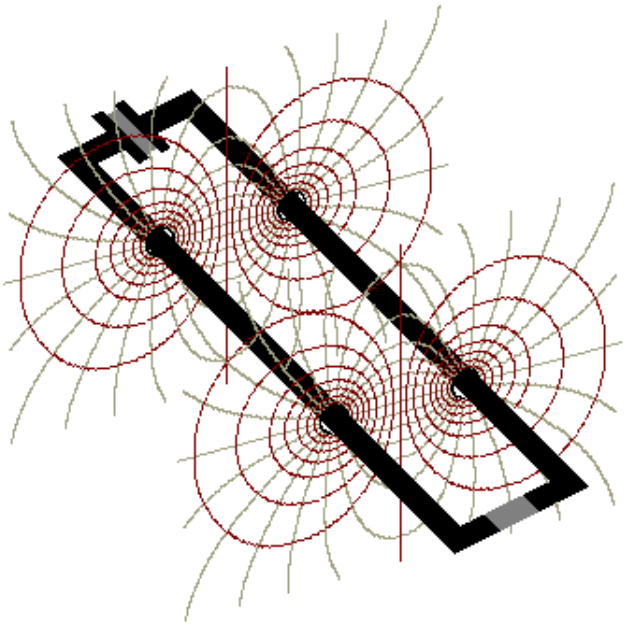

Fig. 1-3 Patterns of electric and magnetic field flux of a power transmission line (Image source: http://amasci.com/elect/poynt/poynt.html)

The radial lines starting from the transmission lines are electric field lines, while the concentric circles around the lines are magnetic field lines. In Fig. 1-4, under energized high voltage power transmission lines, the fluorescent tubes with one end driven into the ground were lighted, without any other sources, by the EM fields (electric field for this case) produced by the power lines. Those tubes, in this case, worked as the EM sensors indicating the status for the power lines of being energized.

Fig. 1-4 Fluorescent tubes lighted by EM field surrounding power lines

(Image source: http://www.doobybrain.com/wp-content/uploads/2008/02/richard-box-field.jpg)

To study EM sensors for power lines and derive the theory for them, it is necessary to have good knowledge of the EM fields produced by the power lines first. The EM fields due to the overhead power transmission lines can be formed by first determining the EM fields due to an infinite long thin wire above the half-space earth at the extremely low frequency (ELF) [19], [20], which have been extensively studied for decades [21] – [28]. The simplified model of an infinite long single-wire transmission line above the half-space earth is shown in Fig. 1-5.

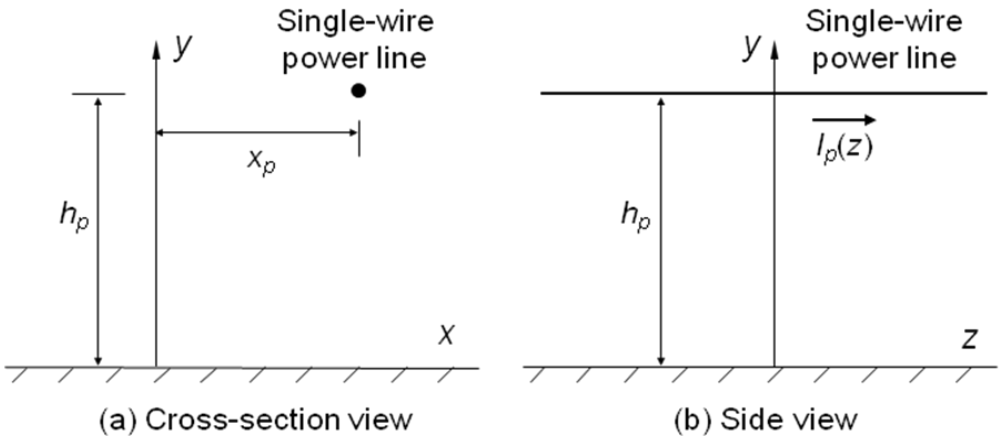

Fig. 1-5 Simplified model for single-wire transmission line above half-space of earth

In the model, the upper half space is free space, characterized by the permittivity ε_0, permeability μ_0, and conductivity σ_0, where $\sigma_0 = 0$. The lower half space is the lossy earth, homogeneous and isotropic, with the permittivity $\varepsilon_g = \varepsilon_{rg}\varepsilon_0$, permeability $\mu_g = \mu_{rg}\mu_0$, and conductivity σ_g, where ε_{rg} and μ_{rg} are the relative permittivity and permeability, respectively. The single-wire transmission line is conducting with a per-unit length resistance of r_p (Ω/m). The line conductor, with radius a_p, is horizontal, extending infinitely in the z direction, and h_p meters above the earth. The coordinates of the line in the transverse plane is (x_p, h_p). It is assumed that the line is energized and the charge density and current on it are denoted as ρ_p (C/m) and I_p. The current can be written as

$$I_p = I_0 e^{\gamma z} \tag{1.1}$$

Where I_0 is the magnitude and γ is the wave propagation constant, arbitrary for now.

The exact solutions to the electromagnetic fields due to the transmission line shown in Fig. 1-5 can be formulated by solving the Maxwell's equations and γ can be determined by matching the boundary conditions on the surface of the line conductor. The results are very complicated and beyond the scope of this dissertation. In practice,

the model of power transmission line is more complicated than that in Fig. 1-5 because of the factors such as unleveled ground, line sag, and height difference between towers. Several analytical or numerical methods to calculate the E and H fields for the more complicated models are introduced in [30] – [34]. Again, they are beyond the scope of this dissertation. Fortunately, if the source energizing the line is at power frequency, i.e., 60Hz, useful approximations can be made to significantly simplify the solutions to the EM fields. The quasi-static approximation is probably the most widely used one in electric power community. For the frequency of 60Hz, the wavelength in free space λ_0 is 5000km (about 3100 miles), much larger than the length scales considered in most power applications. Given that, the spatial traveling property of all the source and field quantities are very small and ignorable. This means the waves of the electromagnetic fields can be assumed to be stationary since the movement of the field distribution has been ignored. In such situation, the fields share many characteristics with the static fields. That is why they are called the 'quasi-static' fields. Being quasi-static, the electric field and magnetic field are treated as decoupled fields (although they are always coupled, in fact [35]) and separately determined, like the static fields, by the charge and current on the transmission line, respectively. The results of the quasi-static approximation are very good. The relative error caused by the approximation is on the order of 10^{-8} when the distance from the observation point to the power line is less than 100m. Finally, it is clarifying to note that quasi-static fields are not equal to static fields, which are strictly time-invariant. For a summary, several facts about the quasi-static approximation are listed below

- Criterion: length scale considered << λ_0;
- Spatial traveling of the fields ignored;
- E and H fields are treated as decoupled fields and separately determined;
- 'Quasi-static' is not equivalent to 'static' (which is exactly time-invariant).

Given the charge density ρ_p on the power transmission line, the quasi-static electric field in the upper half space (free space) can be determined as [35], [36]

$$E_x \cong \frac{\rho_p}{2\pi\varepsilon_0}\left[\frac{(x-x_p)}{R^2} - \frac{(x-x_p)}{(R')^2}\right] \tag{1.2a}$$

$$E_y \cong \frac{\rho_p}{2\pi\varepsilon_0}\left[\frac{(y-h)}{R^2} - \frac{(y+h)}{(R')^2}\right] \tag{1.2b}$$

where $R = [(x - x_p)^2 + (y - h_p)^2]^{1/2}$ and $R' = [(x - x_p)^2 + (y + h_p)^2]^{1/2}$. This result takes exactly the same form of the field obtained by the image theory when the transmission line is above the perfectly conducting earth. Thus, it is implied that the earth can be assumed to be perfect conductor for the calculation of the transverse quasi-static electric field. In practice, the voltage instead of the charge density on the power line is readily known. The power line voltage V_p can be related to ρ_p by

$$\rho_p = \frac{2\pi\varepsilon_0}{\ln\left(2h_p/a_p\right)}V_p = c_p V_p \tag{1.3}$$

where $c_p = 2\pi\varepsilon_0 / \ln(2h_p / a_p)$ (F/m) is the per-unit length capacitance of the power line conductor. For the case of lossy earth, the longitudinal electric field E_z is nonzero and sometimes needs to be taken into account when the inductive coupling is considered. E_z can be found by [26]

$$E_z \cong -\frac{j\omega\mu_0 I_p}{2\pi}\left(1 + \frac{\gamma^2}{k_0^2} - J_C\right)\ln\left(R'/R\right) \tag{1.4}$$

where $k_0^2 = \omega^2\varepsilon_0\mu_0$ and J_C is the Carson's term, defined as

$$J_C \cong \frac{2}{k_g}\int_0^\infty (u-\lambda)e^{-\lambda(y+h_p)}\cos\lambda(x-x_p)d\lambda$$

where $k_g = \omega(\mu_0\varepsilon_g - j\mu_0\sigma_g/\omega)^{1/2}$ (Re(k_g) > 0) and $u = (\lambda^2 - k_g^2)^{1/2}$ (Re(u) > 0). An algorithm for numerical evaluation of Carson's term is provided in [29]. For $k_gR' < 0.25$, J_C can be approximated by

$$J_C \cong \ln\left(k_gR'/2\right) + 0.077 - \frac{2jk_g}{3}\left(y+h_p\right) + \frac{j\pi}{2} \tag{1.5}$$

For the typical lossy earth, magnitude of k_g is on the order of 10^{-3}. J_C can be further simplified as

$$J_C \cong \ln\left(k_gR'/2\right) \tag{1.6}$$

Inserting (1.6) into (1.4) and setting $\gamma = 0$ (usually reasonable for power engineering applications) results in

$$E_z \cong \frac{j\omega\mu_0 I_p}{2\pi}\ln(R)\left[1+\ln\left(k_g/2\right)\right] \tag{1.7}$$

E_z is related to the current I_p, which explains why it should be considered for the case involving inductive coupling. Usually, E_z is much smaller in magnitude than the transverse electric field components.

The magnetic field in free space is found by [35] – [37]

$$H_x \cong \frac{2I_p}{\mu_0}\left[\frac{(y-h_p)}{R^2} - \frac{(y+h_p+\alpha)}{(x-x_p)^2+(y+h_p+\alpha)^2}\right] \tag{1.8a}$$

$$H_y \cong \frac{-2I_p}{\mu_0}\left[\frac{(x-x_p)}{R^2} - \frac{(x-x_p)}{(x-x_p)^2+(y+h_p+\alpha)^2}\right] \tag{1.8b}$$

where $\alpha \cong \sqrt{2}\delta_g e^{-j\pi/4}$ and $\delta_g = \sqrt{2/(\pi\omega\sigma_g)}$ is the skin depth of the earth. This result is not identical to that obtained by the image theory. But it still can be interpreted as

that the second term in bracket represents the effect of a complex image, the image at a complex depth α. If the earth is perfect conductor, $\alpha = 0$. But for typical values of earth characteristics, the magnitude of α is on the order of 1000m, which is very large compared to the height of the power line conductor. The effect of the complex image on the magnetic field can often be ignored since the image is so far away from the observation point in free space. Therefore, for the magnetic field calculations at 60 Hz, the earth can be treated as transparent.

The results given in (1.2), (1.7), and (1.8) provide a simple way to calculate the quasi-static fields due to the power line. They will be used in all the simulations of this dissertation.

CHAPTER 2

POINT PROBES

2.1 Introduction

The point probe is a basic type of electromagnetic (EM) sensor which can be used for the field measurement of power transmission lines. Since the point probe usually has relatively simple construction as well as theory, it is a good starting point for the study of the electromagnetic sensors for the power transmission lines. In this chapter, some assumptions for the model of the point probe, on which the following analysis and discussion are based, are first made. Then the theories describing the interaction between the point probe and the power lines are analyzed by applying the reciprocity theorem for electrostatics. As results of in-depth understanding of these theories, some practical applications of the point probe in the power transmission system are proposed. Finally, the chapter is completed by some lab tests and field experiments for validation of the theories.

A simple point-probe system can be formed with a volume of conductor placed some height above the ground under a power line and grounded by a conductor wire. Generally speaking, the point probe is not necessary to be perfect conductor. A human standing or a car parking under a power line can also be treated as point probe under certain circumstances. But for convenience of analysis, the point probe is assumed to be perfect conductor in this chapter. In order for good accuracy of measurement, the volume and the dimension of the point probe should be reasonably small, compared to

the scale of the transmission line configuration (such as height of the line), so that the probe can be treated as a ‘point’. This makes sure of that the probe brings not much perturbation to the field to be measured and gives relatively accurate information of the interested field quantity.

As already discussed in last chapter, the electromagnetic field (EMF) induced by the power line has its own characteristics, one of which is the quasi-static approximation. For a quasi-static electric field, for instance the electric field generated by the power lines, the ground can be assumed to be perfect conductor. Since the point probe only has capacitive coupling with the power lines, i.e., only the electric field is involved, the ground in the model of the point probe used in this chapter is assumed to be perfect. A summary of the assumptions made for the point probe model is listed below

(a) The probe is a volume of perfect conductor.

(b) The dimension of the probe is small, $D_{\text{probe}} << H_p$ (height of the power line).

(c) The ground is perfect.

(d) One point probe is only grounded by one grounding wire (to avoid introducing the magnetic coupling into the model).

Based on these assumptions, the model of the point probe which will be used through this chapter is defined and illustrated in Fig. 2-1.

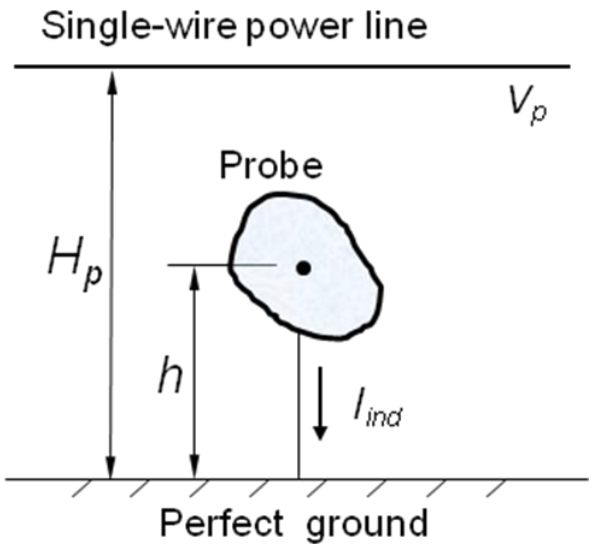

Fig. 2-1 A general model of the point probe.

In Fig. 2-1, under a single-wire power transmission line with a height of H_p (meters), a small volume of conductor with arbitrary shape is placed h meters above the perfect ground. The conductor is connected to the ground by a conducting wire. Note that the shape of the probe is not specified here and it can be arbitrary. However, for convenience again, some symmetrical shapes such as sphere, cylinder or circular plate may be applied when the quantitative analysis is carried out.

2.2 General theory of point probes

When a point probe is put in the interested area, what quantity is really measured by it? To answer this question, the analysis based on the reciprocity theorem is applied. Consider the following two different cases. For the first one, the power line in the model shown in Fig. 2-1 is energized with a voltage of V_p and the point probe is left floating by open the grounding wire at the terminals M and N. The EM field of the power line causes the free charges to redistribute in the conductor probe and lifts the

potential of the probe. The voltage at the terminals MN, which is called the open-circuit voltage and denoted as V_{oc}, is the potential difference between the probe and the ground. Because the point probe works like a receiver this case is called a receiving state and shown in Fig. 2-2(a). For the second case, Fig. 2-2(b), the transmission line is removed and some testing charges of amount Q^b are placed on the probe and cause a surface charge density $\rho_s^b(\bar{r})$ on the surface S of the prob. The superscript 'b' stands for case (b) and the subscript 's' stands for 'surface'. These charges give rise to potential V^b at the field point outside the probe conductor. The probe works like a source and this case is called a source state.

The open-circuit voltage V_{oc} in case (a) is important for obtaining the Thevenin's equivalent of the model and easy to measure. Thus, Voc is to be found first and to what quantity of the excitation field (i.e., the field due to the power line) it is related is to be examined.

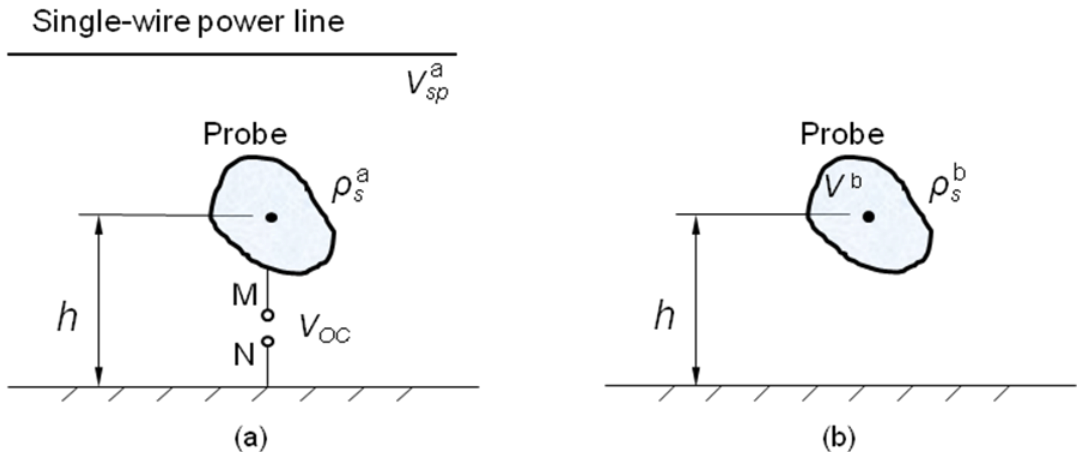

Fig. 2-2 Two states of the point probe for applying the reciprocity theorem: (a) receiving state, (b) source state.

For the receiving state model, although the net free charges on the probe must be zero for the probe's disconnecting with the ground, the non-uniform distribution of

the surface charge (with a density of $\rho_s^a(\bar{r})$) generates an electric field canceling the excitation field due to the power line and keeping the total E field to be zero inside the probe conductor. On the outside, the induced surface charge causes a potential of V^a. The space potential due to the power line in the absence of the probe is denoted as V_{SP}^a. It is clear that the total potential at each field point in the area is the superposition of V_{SP}^a and V^a at that position. The open-circuit voltage V_{oc} representing the total potential on the probe surface can be written as

$$V^a + V_{SP}^a = V_{oc}$$

Thus

$$V^a = V_{SP}^a - V_{oc} \quad (\text{on } S) \tag{2.1}$$

Similarly, in Fig. 2-2(b), the potential is constant over *S*. Applying the reciprocity theorem for electrostatics to this particular problem gives that [38]

$$\oint_S \rho_s^b(\bar{r})\, V^a dS = \oint_S \rho_s^a(\bar{r})\, V^b dS \tag{2.2}$$

Inserting (2.1) into (2.2) yields

$$\oint_S \rho_s^b\ (V_{oc} - V_{SP}^a) dS = V^b \oint_S \rho_s^a\ dS = 0 \tag{2.3}$$

Equation (2.3) can be equal to zero because the probe is 'floating' in case (a) and the net induced free charges on it are always zero. Then

$$\oint_S \rho_s^b\ V_{oc} dS = \oint_S \rho_s^b\ V_{SP}^a dS$$

Because V_{oc} is independent of the position variable, pulling it out of the integral on the L.H.S. results

$$V_{oc} = \frac{1}{Q^b} \oint_S \rho_s^b \, V_{SP}^a dS \tag{2.4}$$

From (2.4), the open-circuit voltage can be looked as the weighted average of the unperturbed power line space potential over the surface of the point probe with the weighting coefficient to be the charge on the probe surface. If the space potential and the density of the testing charge are known on the probe surface, the open circuit voltage V_{oc} can be calculated.

Consider the case for which the probe conductor is small enough, such that the space potential over S can be approximated as a constant and pulled out of the integral in (2.4). Then the open circuit voltage can be rewritten as

$$V_{oc} = \frac{V_{SP}^a}{Q_b} \oint_S \rho_s^b \, dS = \frac{V_{SP}^a}{Q_b} Q_b = V_{SP}^a \tag{2.5}$$

On the most right hand side of (2.5) is just the power line space potential V_{SP}^a due to the transmission line which equals to the open circuit voltage of the probe. Thus the question asked at the beginning of section 2.2 has been answered by (2.5): placing an point probe under a power line and measuring the open-circuit voltage of the point probe results in the unperturbed space potential's being measured at the position of the probe.

If the close the open terminals MN in Fig. 2-2(a) there will be an induced current flowing through the grounding wire. This current can be easily measurable and can also be calculated by finding the Thevenin's equivalent circuit for the probe model in Fig. 2-2(a). Fig. 2-3(a) shows the Thevenin's equivalent circuit.

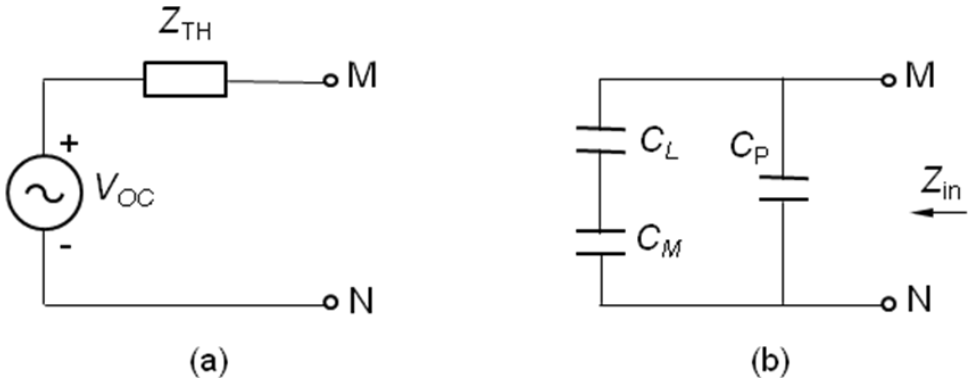

Fig. 2-3 Thevenin equivalent circuit for the point probe model:

(a) equivalent circuit; (b) Circuit to determine the Thevenin equivalent impedance (input impedance looking into terminals MN).

The source voltage in the Thevenin's equivalent circuit is just the open circuit voltage, V_{oc}. The equivalent impedance is the input impedance $\bar{Z}_{in}$ looking into terminals MN. The circuit includes three capacitances for this case, Fig. 2-3(b), because the electric coupling dominates. C_L is the self capacitance of the power transmission line, C_P is the self capacitance of the probe with the presences of the transmission line and ground and C_M stands for the mutual capacitance between the line and the probe.

Once the Thevenin's equivalent circuit is determined, the induced current (in phasor form) is obtained by dividing the open circuit voltage by the input impedance.

$$\bar{I}_{ind} = \frac{\bar{V}_{OC}}{\bar{Z}_{TH}} = \frac{\bar{V}_{OC}}{\bar{Z}_{in}} \tag{2.6}$$

Using (2.5) in (2.6) yields the relationship between the current and the space potential

$$\bar{I}_{ind} = \frac{\bar{V}_{SP}^{a}}{\bar{Z}_{in}} \tag{2.7}$$

Since C_L and C_M are negligible if the distance between the line and the probe is far

enough (which is usually true for power transmission line and the point probe), the input impedance of the probe is mainly determined by the capacitance of the probe, C_P. In addition, when the height of the probe h is large compared to its dimension (at least 5 times of the largest dimension of the probe), the capacitance of the probe can be approximated by its self-capacitance to free space [39], [40]. Finally a simple expression of the induced current is obtained as

$$\bar{I}_{ind} = j\omega C_{self} \bar{V}_{SP}^{a} \tag{2.8}$$

where C_{self} is the self-capacitance of the point probe in free space without the presences of the power line and the ground. For a spherical conductor with a radius of a, its self-capacitance in free space is [40]

$$C_{self} = 4\pi\varepsilon_0 a \tag{2.9}$$

where ε_0 is the permittivity of free space. Usually, the self-capacitance of the point probe is very small, which makes the coupling between the point probe and the power lines is a high-impedance capacitive coupling. Therefore, the earth resistance of the grounding system of the point probe can be neglected. According to (2.8), the induced current is the product of the admittance of the probe's self-capacitance and the space potential due to the power line. This provides us a means to find the space potential by measuring the induced current of the point probe. In practice, by connecting an ammeter between the probe and the ground, this induced current can be easily measured. Using the measurement and (2.8) gives the space potential at the probe's position.

All the analysis above is based on the model with a single-wire power

transmission line to be the excitation source. If the three-phase power transmission line is the case, the analysis for each phase is similar to the previous one and the total induced current of the probe should be obtained by the superposition of the results for all the three phases. Then the total space potential is determined by (2.8).

2.3 Applications of point probe

2.3.1 Power line voltage monitoring

From the previous analysis, it is known that the point probe only picks up the electric coupling from the power line and there is no magnetic coupling involved. As discussed in Chapter 1, for the electromagnetic field produced by an energized power transmission line the quasi-static approximation usually applies. The quasi-static electric field is basically determined by the equivalent charges (i.e. the voltage) and the configurations of the power line [17], [36]. This is also true for the space potential, which is related to the electric field. Therefore, the most straightforward application of the point probe is to monitor the voltage of the power line.

Fig. 2-4 depicts the configuration of a typical horizontal, 230kV, three-phase power transmission line. Here, the ground is assumed to be perfect conductor and the radius of the line conductor is 0.01m.

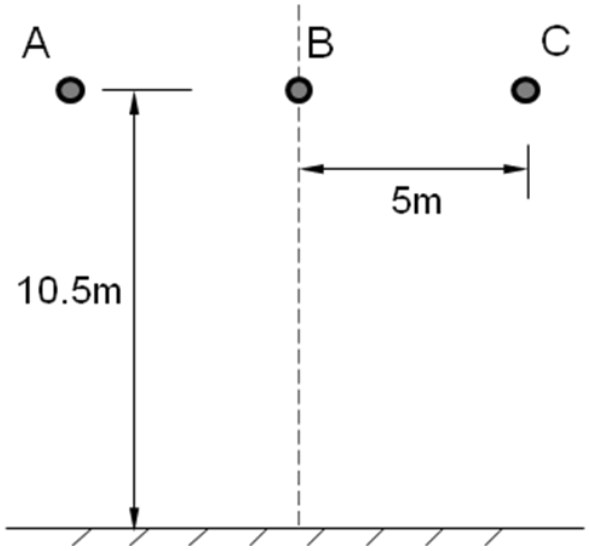

Fig. 2-4 Configuration of a 230kV, three phase, horizontal transmission line

When a set of rating positive sequence voltages is applied on the line, the profiles of space potential both in magnitude and phase are shown in Fig. 2-5. It is noticed that the contours, both for magnitude and phase, have symmetries to the central vertical axis.

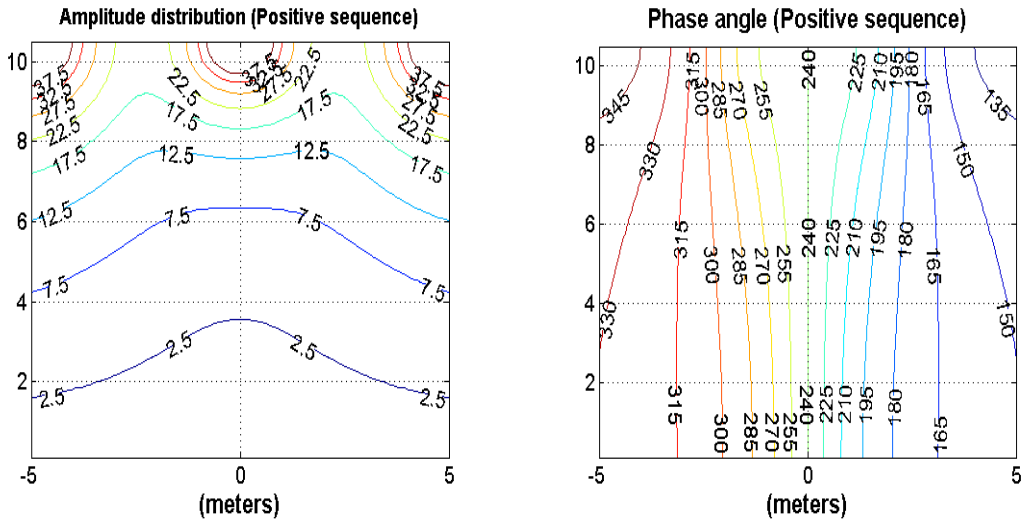

(a) magnitude (kV) (b) phase angle (degree)

Fig. 2-5 Space potential profiles for positive sequence voltage

The total space potential at a field point is the superposition of the space potentials caused by the three phase lines. And the space potential caused by each

phase is proportional to the voltage of that phase. So, the total space potential changes linearly with the magnitude of the applied voltage on the power line.

According to (2.8), if a grounded point probe is placed in the vicinity of the power line, the space potential at the location of the probe can be determined by measuring the induced current of the probe, illustrated in Fig. 2-6. The probe is placed on the central axis of the cross section of the three-phase line. Consider (2.8) and the analysis in last paragraph, the magnitude of the induced current changes linearly with that of the applied voltage on the power line, too.

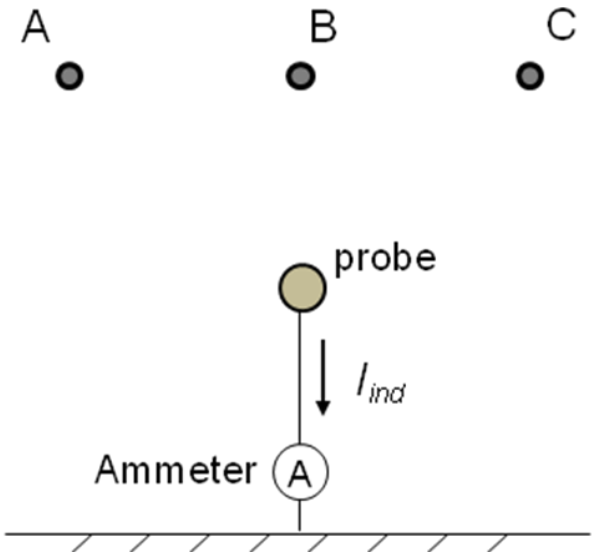

Fig. 2-6 Single probe placed under the three-phase power line

Fig. 2-7 shows the results of a simulation to find the relationship between the power line voltage and the induced current in the point probe. The models of the power line and the probe are the same as shown in Fig. 2-4 and Fig. 2-6, respectively. The probe is a spherical conductor with radius of 7.6 cm (3 inch) and is 3 meters above the ground. The applied voltage of the power line changes in between ±10% off the rating voltage (230kV).

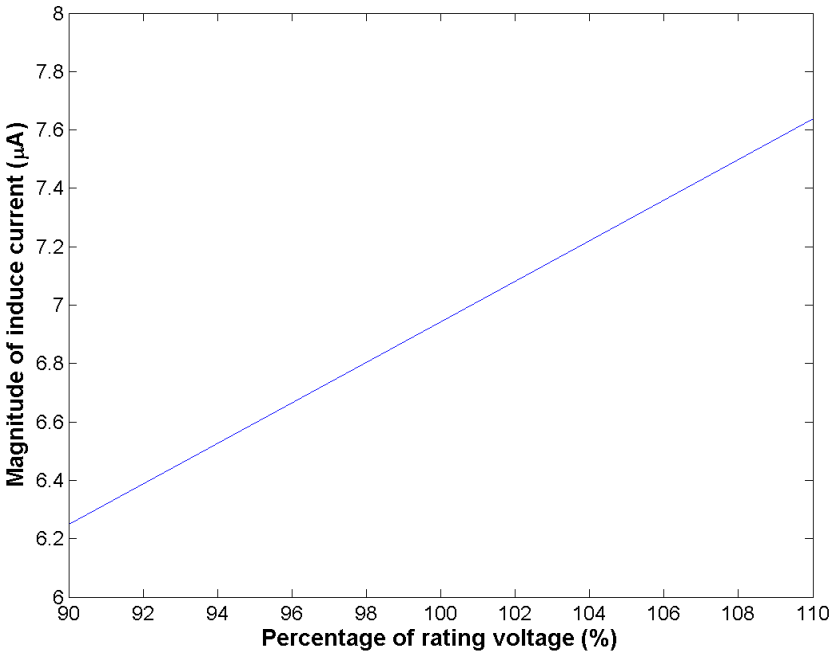

Fig. 2-7 Applied voltage (in percentage of the rating voltage, 230kV) on the power line vs. induced current in point probe.

It is obvious from Fig. 2-7 that the induced current is linear to the applied voltage on the power line, which indicates that the magnitude of voltage on the power line can be monitored by the induced current of the point probe. However, the space potential also depends on the configurations of the power line. The changing of the positions of the line conductors may change the induced current. The sag of the power line (i.e. the height change of the line conductor), for instance, will affect the induced current. To avoid this kind of effect, the place to put the probe should be chosen properly. The height of line conductor may vary a lot at the mid span due to line sag, but it doesn't change much in the area near the tower. If the probe is placed closed to the tower, the effect of the sag on the induced current will be reduced.

2.3.2 Sag monitoring

Another simple application of the point probe is to measure the sag of the power line.

The probe is placed at the mid-point of a span because the power line conductor sags much more than what is does at near the tower. The same probe and power line models as described in Fig. 2-4 and Fig. 2-6 are used. And assume the length of one span is L = 106.7m (350ft). The sag of the power line is accounted in the percentage of L. Fig. 2-8 shows the change of the current in the probe due to the line sag.

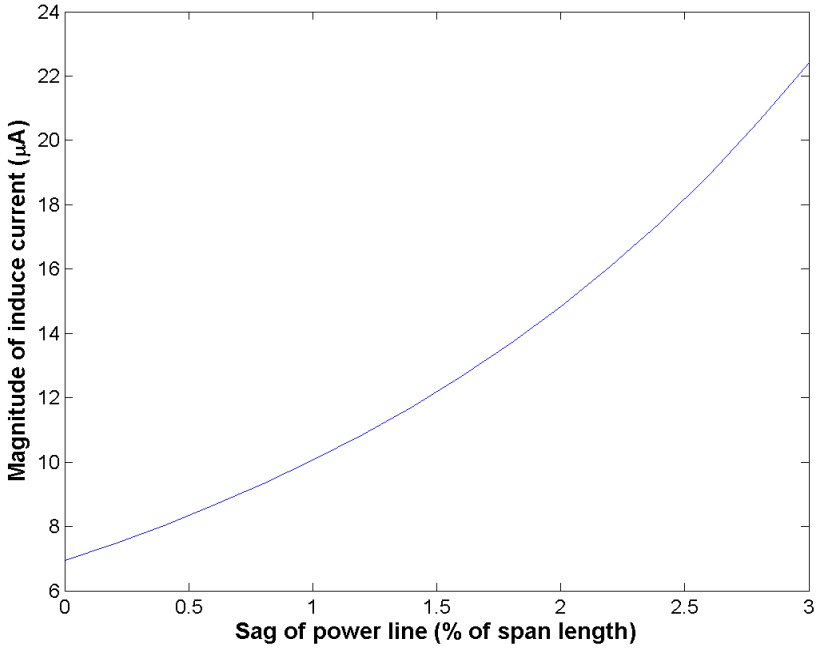

Fig. 2-8 Line sag (in percentage of the span length, L = 106.7m) vs. induced current in point probe.

The induced current increases as the line sag increasing, but not linearly. When the line sag is 3% of the span length (about 3.2 meters of height reduction), the induced current can reach three times of the value when there is no sag. This character makes the point probe a good sensor to monitor the line sag. But, as discussed in section 2.3.1, the line voltage can bring effect on the induced current. This effect is an error when the point probe is used for the sag measuring. Fortunately, in real power system the voltage of the power line usually varies within ±10% off its rating voltage.

On the other hand the sag of the line causes the height of the conductor to change in a relatively large range at the mid-point of a span. The effect of the sag on the induced current is much larger than that of the voltage. This is also proved by the level of the magnitude change shown in Fig. 2-7 and Fig. 2-8.

2.3.3 Negative/Zero sequence voltage detection

The induced current and space potential in (2.8) are both phasors, which implies that the information of both the magnitude and the phase of the space potential can be obtained by the point probe if used in a proper way. Practically, the phase angle information is hard to be picked up if only one probe is used. But if two or more probes are applied the phase information can be utilized to accomplish more complicated tasks than just measuring the magnitude of the space potential. A two-probe system for the negative/zero sequence voltage detection is one example among those applications.

Fig. 2-5 shows the positive space potential in both magnitude and phase angle. If the negative sequence voltage is applied on the power line, the contours of the magnitude and phase angle keep the same shapes, but the phase angle's distribution changes, as shown in Fig. 2-9(b). Comparing Fig. 2-5 and Fig. 2-9, in most places in the given cross sectional area the space potential phase changes under the different sequence modes of power line voltage.

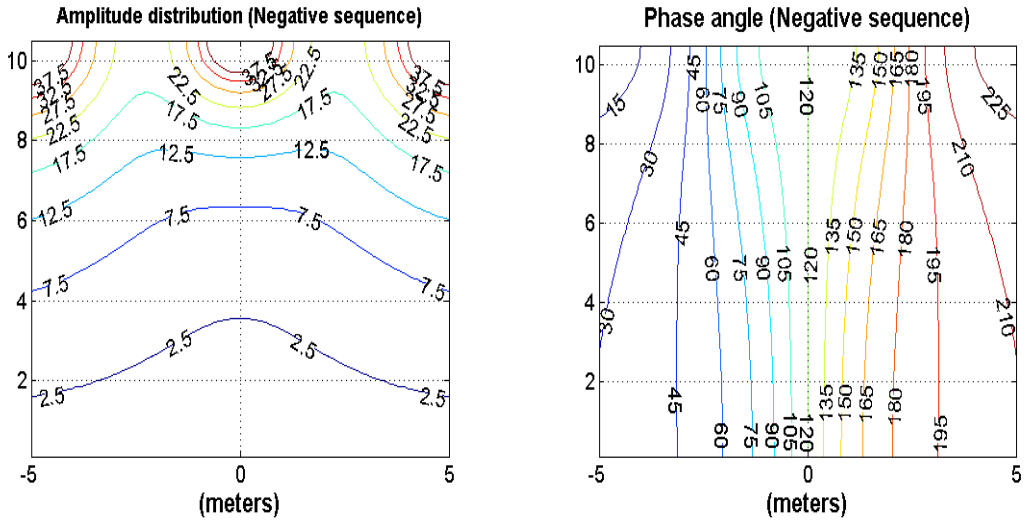

(a) magnitude (kV) (b) phase angle (degree)

Fig. 2-9 Space potential profiles for negative sequence power line voltage

Consider two point probes placed at symmetrical positions along two phase angle contours (dashed lines), say 300 ° and 180 ° for positive mode, as illustrated in Fig. 2-10(a). The positive mode means positive sequence voltage is applied in the three-phase power line. The two contours have a phase angle difference of 120 °. With a +30 ° phase shifter connected to the probe on the left side and a -30 ° phase shifter connected to the probe on the right side, the induced currents in the two probes will have same magnitude but a 180 ° difference of phase angle. Combining them leads to the cancellation of each other and the total current I_{tot} is zero.

If the applied voltage in the power lines changes from positive mode to negative mode, the situation will also change. As shown in Fig. 2-10(b), the phase angle of the left contour becomes 60 ° for negative mode and the angle for the right one is still 180 °. After the same ±30 ° phase shifting as for positive mode, the two induced current now have a 60 ° phase difference. Their total current is no longer zero. Therefore, the settings of the two point probes and the phase shifters only work for positive sequence

mode to get zero total current. Any amount of presence of the negative sequence voltage in the applied voltage can cause nonzero total induced current in the probe. Monitoring whether the magnitude of I_{tot} is zero provides a indicator of negative sequence voltage in the power line.

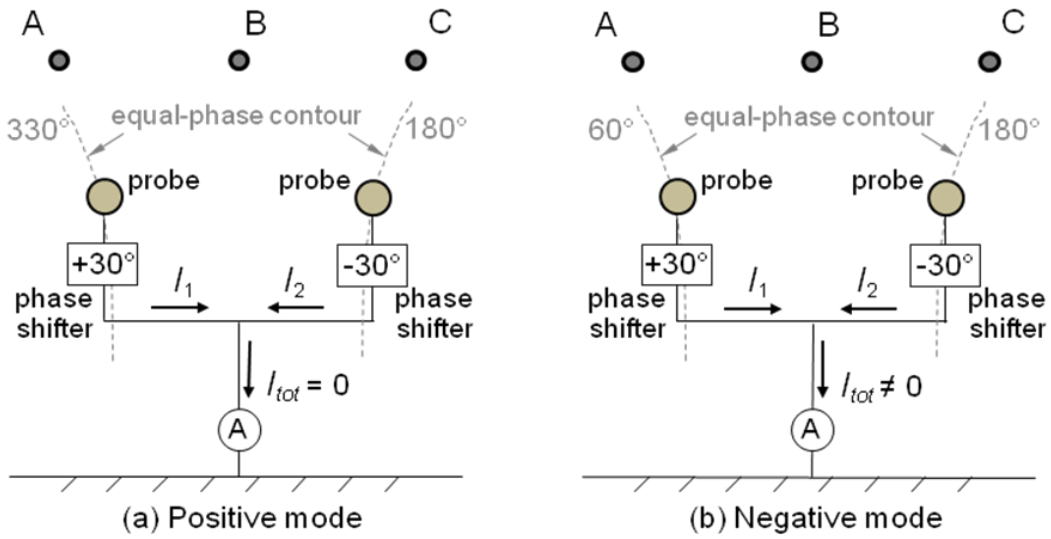

Fig. 2-10 Two probes designed to detect negative sequence component in line voltage

Another advantage of this two-probe scheme is that by properly choosing the phase-angle contours the system can work independent of the conductor height. For instance, the 315 ° and 165 ° contours in Fig. 2-5(b) become nearly vertical below the height of about 5m. When the height of conductor changes (due to the line sag) in a reasonable range, the phase angles of the two probes do not change much because they almost keep being on the same equal-phase contours. Thus the two-probe system can still provide good performance when the sag of the line is changing. For this case, the +30 ° and -30 ° phase shifter should be respectively replaced by a +15 ° and -15 ° phase shifter in order to obtain zero I_{tot} in positive mode. This example shows how to choose the positions of the probe such that the effect of the line sag can be

significantly mitigated. However, sometimes it is an advantage to use the dependence of phase angle on the line sag (i.e., conductor height). Then the point probe must be placed in the areas in which the equal-phase contours have slow slope. Because in these areas the phase angle of space potential is sensitive to the conductor height. The induced current is consequently sensitive to the change of conductor height.

Once the mechanism of two-probe system is well understood, it's not difficult to update the system with the three-probe model. Using three probes allow us to built a device to indicate the four operating modes in the power transmission line: positive mode, negative mode, zero mode (zero sequence voltage is applied) and unenergized mode (the power line is unenergized). One example for the three-probe approach is illustrated in Fig. 2-11. Three identical probes are located on one equal-magnitude contour (dotted line). The middle probe is on the central axis and the other two are put on two symmetrical phase-angle contours (dashed lines). As shown in Fig. 2-11(a), the phase-angle contours of 270 °and 210 °(for positive sequence) are chosen to place the probes on. The central phase-angle contour has the angle value of 240 °. The angle shifting is -90 °for the left phase shifter and +90 °for the right one.

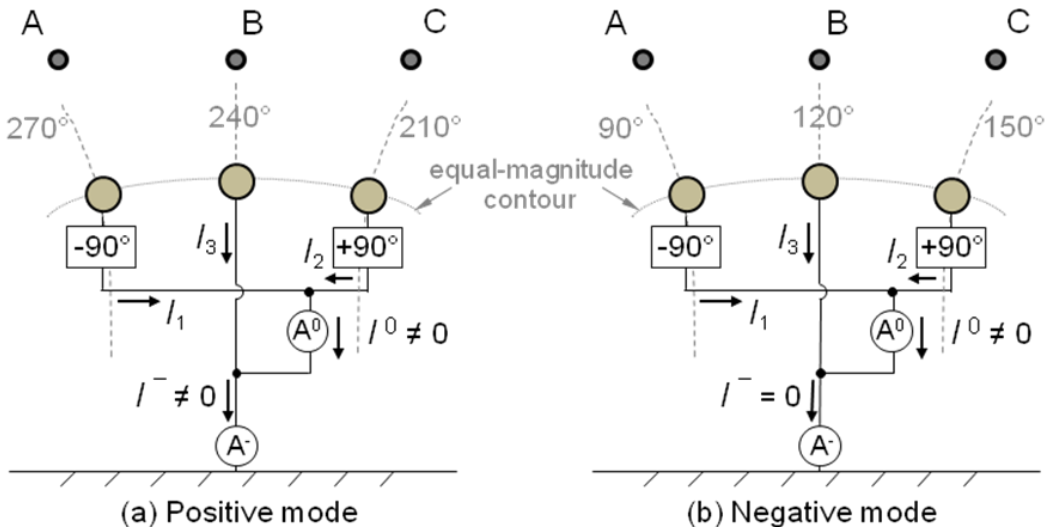

Fig. 2-11 Design of a three-probe device used as a four-mode indicator

The two ammeters A^0 and A^- are the indicators for zero mode and negative mode, respectively. The reading on A^0 is zero when the applied voltage on the power line is in zero mode and reading on A^- is zero when negative mode is on. If both of the two meters show nonzero readings there is only positive-sequence voltage operating. When the transmission line is not energized, there will be no induced current in any of the three probes. Hence, by inspecting the current in one single probe, the out-of-service mode of the line can also be indicated by this device. Table 2-1 shows the corresponding current statuses for each of the four modes.

Table 2-1 Four sequence modes and their corresponding current statuses

Mode	$\lvert\bar{I}_{1,2or3}\rvert$	$\lvert\bar{I}^0\rvert$	$\lvert\bar{I}^-\rvert$
Positive	$\neq 0$	$\neq 0$	$\neq 0$
Negative	$\neq 0$	$\neq 0$	0
Zero	$\neq 0$	0	$\neq 0$
Out-of-service	0	0	0

It is not often true in the real power system that only one sequence of voltage operates in the power line. The unbalanced operations or faults can cause the

presences of the negative and zero sequence components in line voltage. Consider the case that both positive sequence and negative sequence components are present at the same time. It is good for protection relay engineer to know the magnitude ratio of the negative sequence to the positive sequence voltage. Since the phase of the space potential depends on the sequence of the line voltage, one may be inspired that the point probe can be used for accomplishing this task. Here is a design, Fig. 2-12, of a three-probe device by which the ratio of the negative to positive sequence line voltage can be found.

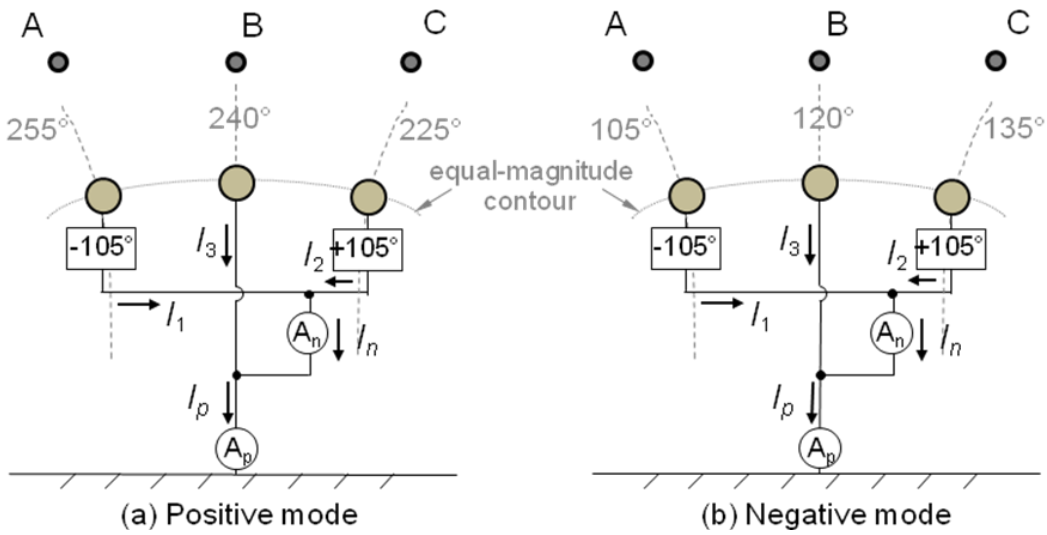

Fig. 2-12 Design of a negative-to-positive ratio measurement device

Similar analysis applies as before. If the contours of 255 ° and 225 ° (for positive mode) are chosen, in the negative mode they have angles of 105 ° and 135 °, respectively. The angle shiftings are chosen to be ±105 °. The two ammeters A_p and A_n are set to respectively measure the magnitude of the induced current for positive and negative modes. This is valid because for the settings shown in Fig. 2-12 it is always true that

$$\bar{I}_n^+ = 0 \text{ and } \bar{I}_p^+ = I^+ \angle 240°$$

where I^+ is the magnitude of positive sequence current in the probes and the superscript '+' stands for quantities in positive mode. The positive currents from the two side probes always cancel each other because they have 180 ° angle difference after phase shifting. Thus, in the reading of ammeter A_n positive sequence current is always zero. The ammeter A_n will only measure the magnitude of negative sequence current. Similarly

$$\bar{I}_n^- = I^- \angle 300° \text{ and } \bar{I}_p^- = 0$$

where I^- is the magnitude of negative sequence current in the probes the superscript '-' stands for quantities in negative mode and. Combining the currents for the two sequence modes shows that the reading on A_p is only the magnitude of positive sequence current $\bar{I}_p = \bar{I}_p^+ + \bar{I}_p^- = \bar{I}_p^+$ and the reading on A_n is only the magnitude of negative sequence current $\bar{I}_n = \bar{I}_n^+ + \bar{I}_n^- = \bar{I}_n^-$. Thus

$$\frac{\left|\bar{I}_n\right|}{\left|\bar{I}_p\right|} = \frac{\left|I^- \angle 300°\right|}{\left|I^+ \angle 240°\right|} = \frac{I^-}{I^+} \tag{2.10}$$

From the analysis in section 2.2, the induced current is proportional to the line voltage in magnitude, which results in that

$$\frac{\left|\bar{V}_{line}^-\right|}{\left|\bar{V}_{line}^+\right|} = \frac{\left|\bar{I}_n\right|}{\left|\bar{I}_p\right|} = \frac{I^-}{I^+} \tag{2.11}$$

The theory introduced in this example is verified by computer simulation. In the simulation, the positions to locate the three probes have the coordinates (in meters) as (-0.414, 2.98), (0, 3.08), and (0.414, 2.98). Apply a series of three-phase line voltage which contain different percentages of negative sequence. Calculate the current ratio

by (2.10). Table 2-2 lists the results. The error is due to the position of the probes.

Table 2-2 Results for computer simulation

$\frac{\lvert\bar{V}^{-}_{line}\rvert}{\lvert\bar{V}^{+}_{line}\rvert}$	5.0%	10.0%	15.0%	20.0%	25.0%	30.0%	35.0%	40.0%
$\frac{\lvert\bar{I}_{n}\rvert}{\lvert\bar{I}_{p}\rvert}$	4.9%	9.8%	14.7%	19.6%	24.5%	29.5%	34.4%	39.3%

2.4 Lab tests and field experiments of point probe

Some lab tests and field experiments have been conducted to validate the theories of the point probe.

2.4.1 Single-phase, single-probe lab test

This test is to check whether the modeling of space potential probe works as presented in (2.8). Voltage is applied on one bus bar to simulate a single-phase power transmission line. A spherical conducting probe supported by a PVC pipe locates right below the bar, as illustrated in Fig. 2-13. The probe is grounded by one coaxial cable. The induced current is measured by a “FLUKE 189” ammeter. By using (2.2) the space potential is obtained from the induced current. To verify the result, the space potential at where the probe is placed is also directly measured by a space potential meter (see Fig. 2-14). The two potential values, one computed from the current and one measured directly, are compared in Table 2-3.

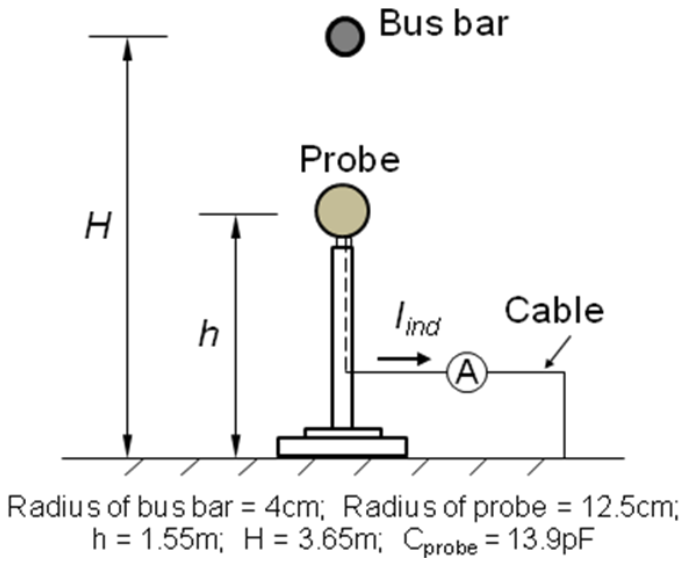

Fig. 2-13 Single-phase, single-probe lab test

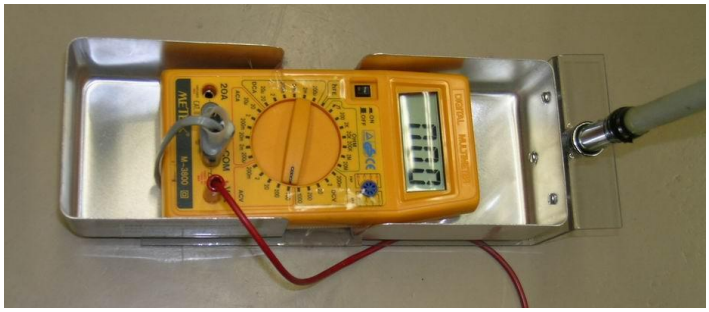

Fig. 2-14 Space potential meter

Table 2-3 Results of single-phase, single-probe lab test

Applied Voltage (kV)	Probe Current (μA)	SP value from current (kV)	SP value from meter (kV)	Relative error
10.95	6.87	1.31	1.22	6.7%
20.8	12.6	2.41	2.40	0.2%
30.7	17.9	3.42	3.39	0.8%
40.5	24.4	4.66	4.62	0.8%
49.7	29.6	5.64	5.58	1.0%
60.5	36.1	6.89	6.80	1.3%
70.1	41.3	7.89	7.83	0.7%
80.1	47.2	9.00	8.90	1.1%
91.0	53.7	10.25	10.37	1.1%
100.1	58.4	11.14	10.97	1.6%

The difference between the two values (from current and from meter) is very small, which prove the correction of the modeling of space potential probe.

2.4.2 Single-phase, two-probe lab test

Two probes are used in this test to check whether the induced currents in the probes can be combined correctly. The test setting is similar to the single-probe test except another probe is introduced in but 10ft away from the previous one. Fig. 2-15 shows the illustration.

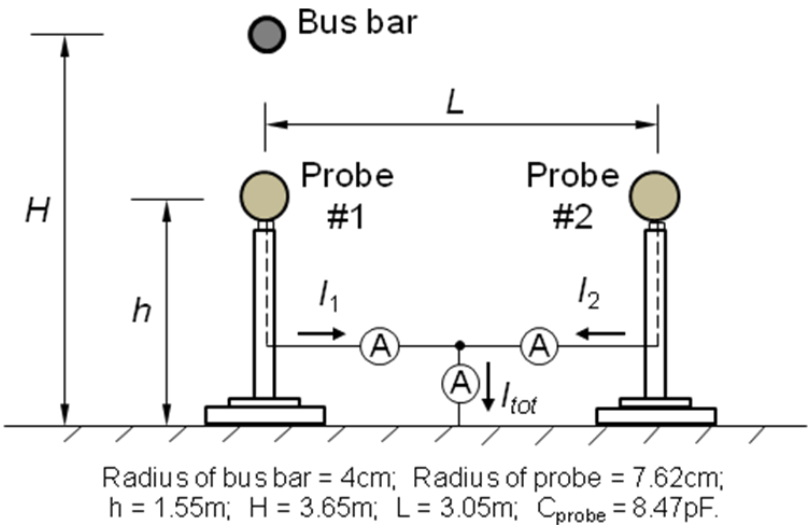

Fig. 2-15 Single-phase, two-probe lab test

The induced currents from probe #1, #2 (I_1 and I_2, respectively) and the total current I_{tot} are measured. I_1 and I_2 are in phase because of the single phase voltage. So I_{tot} is equal to the arithmetical summation of I_1 and I_2. Results are shown in Table 2-4.

Table 2-4 Results of single-phase, two-probe test

Applied Voltage (kV)	Current of Probe #1, I_1 (μA)	Current of Probe #2, I_2 (μA)	Total Probe Current, I_{tot} (μA)	I_1+I_2 (μA)
15.4	9.79	3.43	12.82	13.22
21.1	10.67	3.94	14.23	14.61
31.5	14.37	5.73	19.49	20.10
40.8	17.21	7.08	23.58	24.29
51.0	21.03	8.43	28.82	29.46
61.5	22.34	8.75	30.46	31.09
69.6	24.76	9.85	34.34	34.61
81.1	28.51	11.24	39.42	39.75
91.6	32.26	12.82	44.86	45.08
102.8	36.06	14.28	50.05	50.34

2.4.3 Field experiments

One span of the 230 kV N Lewiston-Shawnee line is chosen to be the experiment site for the field experiments. The line is horizontal configured and has H-framed wood tower, Fig. 2-16 (a). The ground between pole 16/6 and 16/7, about 5 miles northwest to Colton (WA), is flat enough for the experiment, Fig.a 15 (b).

(a) line configuration (b) span between pole 16/6 and 16/7

Fig. 2-16 The site of the field experiment for point probe

Listed below are some parameters for the transmission line at the site.

Height of line conductor at mid-span	about 45 ft (13.93m)
Phase spacing	19.25 ft (5.87m)
Diameter of the conductor	1.345 inch (0.0342m)

Based on these configurations the distribution of the space potential under the line can be simulated by computer. Fig. 2-17 shows the space potential profiles in the cross sectional plane at the mid-span.

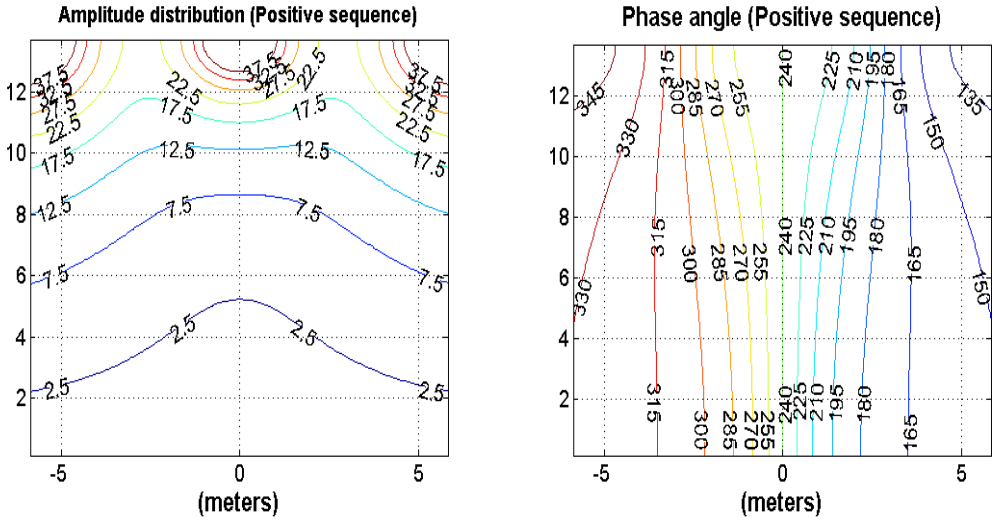

(a) magnitude (kV) (b) phase angle (degree)

Fig. 2-17 Positive sequence space potential profiles of the power line at the experiment site

To conduct the field experiment a two-probe device for measuring is designed. Two spherical probes are used, each of which has a pipe supporter and a cross-shaped base made of PVC pipes. The height of the supporter can be adjusted so that the probes can be placed at the desired height. Table 2-5 lists some parameters of the device.

Table 2-5 Parameters of the two-probe device

Radius of probe	3 in (0.0762m)
Height range of supporter	6~10.5ft, adjustable
Dimension of base	8×8ft, diagonal
Minimum current recognized	0.01μA

Fig. 2-18 is a picture taken at the experiment site showing the experiment settings. The height of the probe is fixed at 3.048m (10ft). The two probes are symmetrically moved from the middle by certain incremental distance step. Induced currents from both probes and their total current are measured by ammeters.

Fig. 2-18 Settings for the field experiment

When the probes are moved to locate on the angle contours of 330^{o} and 150^{o} respectively, the total induced current is expected to be very small because of the cancellation. According to Fig. 2-17, this will happen when the each probe's offset from the middle is about 5.8m.

The field experiment was done on October 17th, 2006. The original data of induced current are listed in Table 2-6. These data are compared to the theoretical ones as shown in Fig. 2-19 and Fig. 2-20. The solid lines and the dash lines represent measured values and the dot lines represent theoretical values.

Table 2-6 Original data of induced current

d (ft, from the middle)	*d* (m)	I_A (μA)	I_B (μA)	I_A+I_B (μA)
2	0.61	4.09	4.08	7.84
4	1.22	5.07	5.09	7.73
6	1.83	6.07	6.09	7.18
8	2.44	7.56	7.24	6.21
10	3.05	8.64	8.75	4.98
12	3.66	9.73	9.70	3.83
14	4.27	10.71	10.76	2.60
16	4.88	11.54	11.55	1.49
17	5.18	11.90	11.93	0.96
18	5.49	12.31	12.32	0.57
18.5	5.64	12.53	12.43	0.56
19	5.79	12.57	12.66	0.61
20	6.10	12.79	12.80	0.92
22	6.71	13.32	13.23	1.76
24	7.32	13.74	13.55	2.60
26	7.92	14.06	13.85	3.44
28	8.53	14.20	13.99	4.13
30	9.14	14.27	13.92	4.83

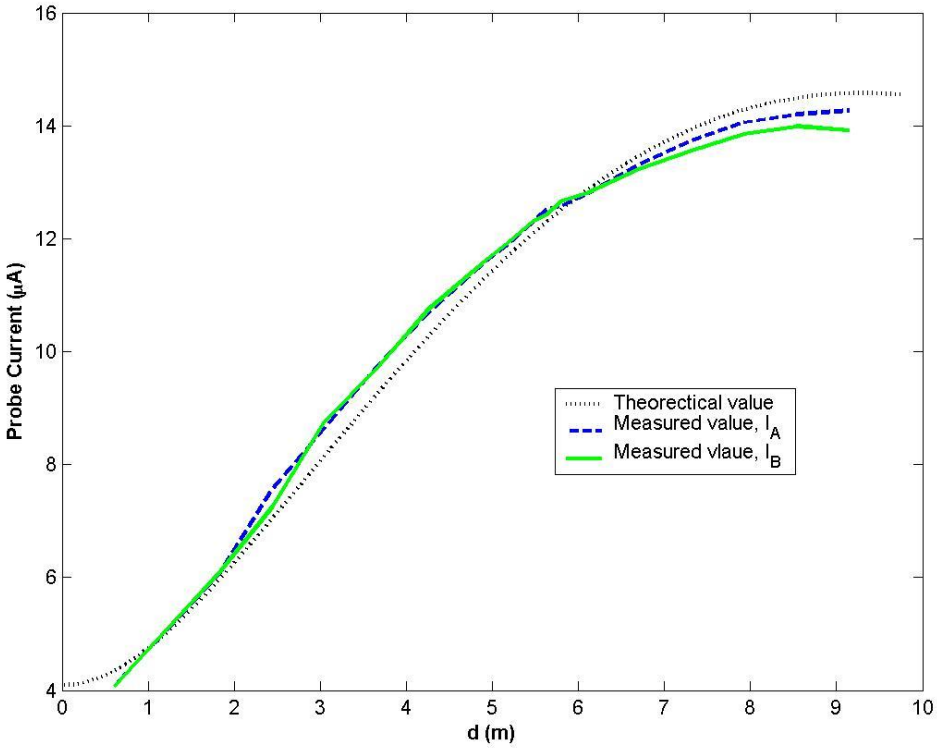

Fig. 2-19 Probe currents of the field experiments

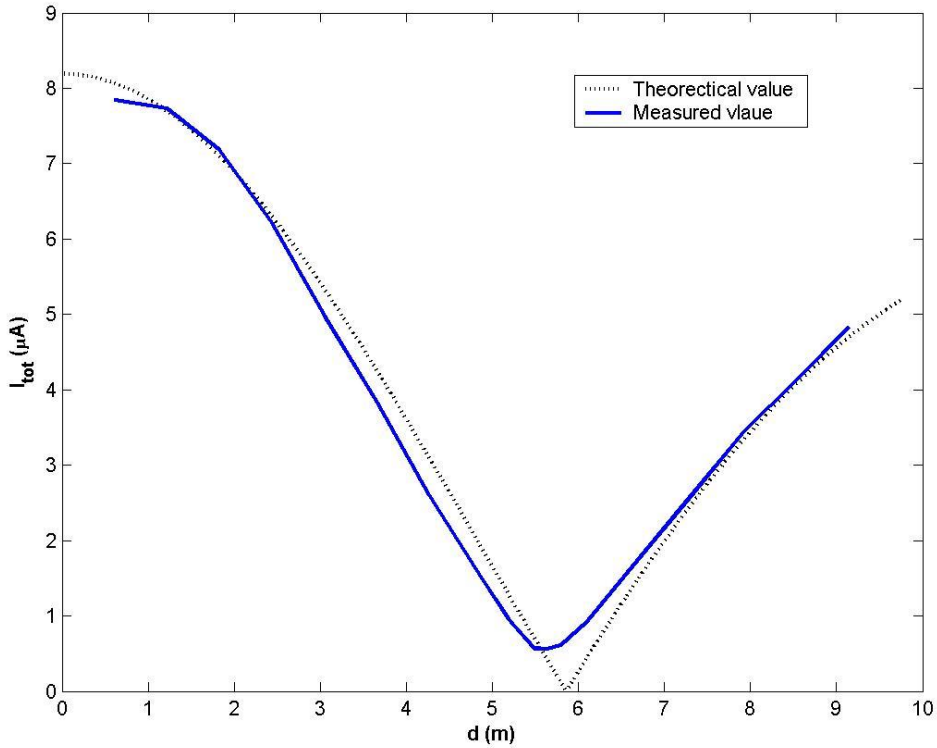

Fig. 2-20 Total current of the field experiments

This experiment is a simplified implementation of the two-probe approach. The positive sequence voltage is assumed to be applied in the power line and no phase shifters are used. The results validate the theory that the current cancels at certain positions of the probes. The zero total current occurs when the probes are placed at the same positions as predicted. Therefore, this experiment proves that the phase angle information can be picked up and utilized by using the point probe and it also indirectly proves the theories for the negative/zero sequence voltage detection discussed in section 2.3.3.

CHAPTER 3

GENERAL THEORY OF LINEAR SENSORS

The linear sensor is the type of electromagnetic (EM) sensor to be studied in Chapter 3 to 5 of this dissertation. It has a wire-like shape, which differs from the point probe in Chapter 2. Since the analysis for the linear sensor is based on the reciprocity theorem, which places no special requirements on the sensor shape, there are not many shape constraints made on the model of the linear sensor. For example, it sensor is not necessary that the sensor be straight or be uniform in diameter. The wire-like EM sensor has many practical applications in high frequency areas, but its application in low frequency system such as electric power system at 60Hz is seldom seen in the literature. Important objectives of this dissertation are to derive a theory and to propose potential applications for using the linear sensor in EM measurement of power transmission line status.

In this chapter the theory behind the linear sensor will be explored. An approach based on the reciprocity theorem for general electromagnetic case is introduced in 3.1. A solution to the induced current in a linear sensor excited by the incident electromagnetic field is then provided. Following this, an approach using the model of per-unit-length induced voltage and current sources is introduced in 3.2. Finally, the relationship between the two approaches is discussed in 3.3.

3.1 Approach by reciprocity theorem

A general model of the linear sensor to be used in the following sections is depicted in

Fig. 3-1.

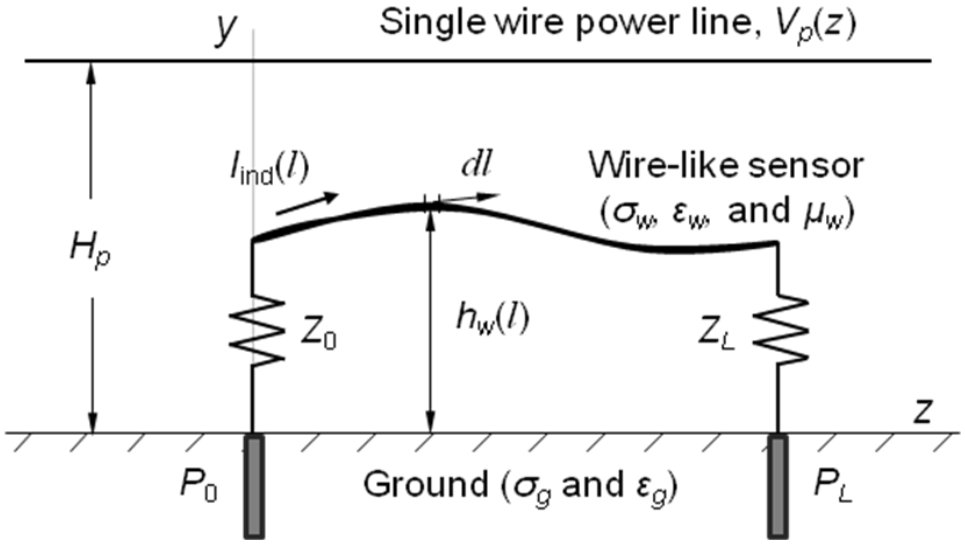

Fig. 3-1 A general model of the linear sensor

In this model, the wire-like sensor is assumed to have a curve shape and a non-uniformly distributed diameter in order not to lose generality. The radius $a_w(l)$ height $h_w(l)$ and $x(l)$ vary with length, where l is the variable indicating the position along the central axis of the sensor wire. However, for convenience the sensor is assumed to be 'thin' everywhere, which means the largest diameter of the sensor is much smaller than its length and the height of the power line conductors. The sensor has distributed parameters, i.e., its electric and magnetic characteristics, such as the conductivity $\sigma_w(l)$, permittivity $\varepsilon_w(l)$, and permeability $\mu_w(l)$, that can all be functions of position. If the impedance per unit length of the sensor is $Z_w(l)$, the lumped impedance of a short segment Δl (at position l) is $Z_w(l)\Delta l$.

The sensor is connected to the ground through impedances Z_0 and Z_L respectively, at its ends at $l = 0$ and $l = L$. The grounding system is also taken into account. Assume the underground parts of the grounding system are two cylindrical conducting pins P_0

and P_L, which vertically penetrate into the lossy earth with dielectric constant of ε_g and conductivity of σ_g. The grounding impedances of the two pins are Z_{p0} and Z_{pL}, respectively. The sensor itself along with impedances Z_0 and Z_L, grounding impedances Z_{p0} and Z_{pL}, and the earth return form a sensor system, which is placed under a power transmission line.

The power line, with an applied voltage of $V_p(z)$ on it, is a single, horizontal and infinitely extending wire in 'z' direction. The power line conductor has a radius of a (meters) and is H (meters) above the ground. The applied voltage $V_p(z)$ is a 60Hz sinusoid, for which the free space wavelength λ_0 is 5000km. Thus the sensor is electrically short (i.e., length of the sensor << λ_0) for most cases. But in some special cases, high speed transient processes for instance, the sensor may not be electrically short. The manner in which the sensor is placed is not specified in this model. It could be placed parallel, oblique, or perpendicular to the power line's axial direction, i.e., z direction. Models with the sensor placed perpendicular and parallel to the power line are to be studied in Chapter 4 and Chapter 5, respectively.

3.1.1 Reciprocity theorem for general electromagnetic case

Before the analysis for the model in Fig. 3-1 is started, the Lorentz reciprocity theorem for general electromagnetic cases is recalled here. $\mathbf{J_1}$, $\mathbf{M_1}$ and $\mathbf{J_2}$, $\mathbf{M_2}$ are the two distinct sets of electric and magnetic current sources radiating at the same frequency and in the same linear, isotropic medium. $\mathbf{E_1}$, $\mathbf{H_1}$ and $\mathbf{E_2}$, $\mathbf{H_2}$ are the electric and magnetic fields produced by them, respectively. If a region with infinite radius is considered, the Lorentz reciprocity theorem can be expressed as [41]

$$\iiint_V (\mathbf{E_1} \bullet \mathbf{J_2} - \mathbf{H_1} \bullet \mathbf{M_2}) dv' = \iiint_V (\mathbf{E_2} \bullet \mathbf{J_1} - \mathbf{H_2} \bullet \mathbf{M_1}) dv' \tag{3.1}$$

For the case without magnetic current sources ($\mathbf{M_1} = \mathbf{M_2} = 0$), (3.1) reduces to

$$\iiint_V \mathbf{E_1} \bullet \mathbf{J_2} dv' = \iiint_V \mathbf{E_2} \bullet \mathbf{J_1} dv' \tag{3.2}$$

Particularly, consider the case that the source $\mathbf{J_1}$ and $\mathbf{J_2}$ are the currents on two wires (i.e. two line currents), w_1 and w_2, respectively, as illustrated in Fig. 3-2.

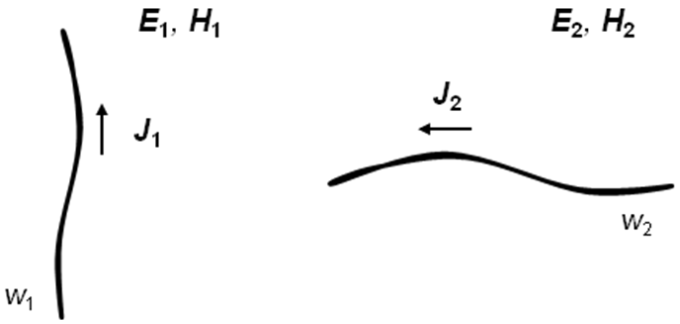

Fig. 3-2 Special case for reciprocity theorem: sources reduces to line currents (J_1 and J_2)

The volume integral in (3.2) reduces to line integral. Thus, the reciprocity theorem for this special case can be presented as

$$\int_{w_2} \mathbf{E_1} \bullet \mathbf{J_2} dl' = \int_{w_1} \mathbf{E_2} \bullet \mathbf{J_1} dl' \tag{3.3}$$

Equation (3.3) is very important and it will be used to derive the basic theory for the linear sensor in the following sections.

3.1.2 Two situations for implementing reciprocity theorem

Equation (3.3) will now be used to study the linear sensor model shown in Fig. 3-1. Basically, the sensor is a receiving antenna. In the antenna theory, one important problem is to determine the current distribution on the antenna [18]. Thus, the goal here is to find the induced current and voltage everywhere on the sensor when it is excited by the electromagnetic field produced by the power line. The approach is to determine the Thevenin equivalent circuit of the sensor at an arbitrary position along

it. To accomplish this the sensor is first opened at a gap *w* between terminals M and N as shown in Fig. 3-3. As introduced in Chapter 2, the Thevenin equivalent circuit consists of the open circuit voltage across the gap and the input impedance looking into terminals MN. Again, two situations are defined, as illustrated in Fig. 3-3(a) and (b), to apply the reciprocity theorem.

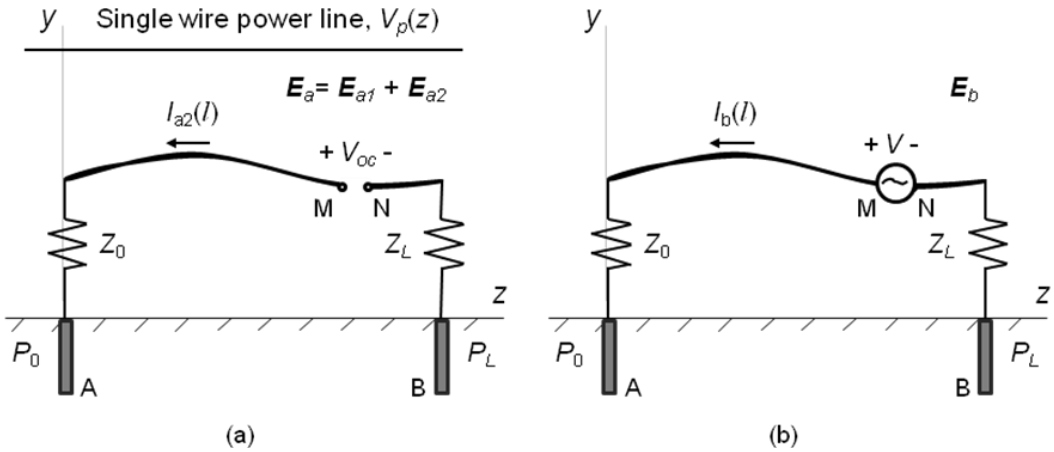

Fig. 3-3 Two situations for implementing reciprocity theorem: (a) the probe is opened at the gap between terminals M and N, the power line is energized as the source and the sensor wire works as a receiver; (b) a voltage source is put in between MN, the probe works as a source and the power line is removed.

In case (a), the power line is energized by the voltage source $V_p(z)$, which generates a current $I_p(z)$ in the line. This current produces the incident electric field $\bar{E}_{a1}$. The open circuit voltage across the gap at MN is V_{oc}. There is a current $\bar{I}_{a2}$ induced in the sensor by the incident field. The electric field produced by $\bar{I}_{a2}$ is denoted as $\bar{E}_{a2}$. By superposition the total electric field $\bar{E}_a$ at a field point in the upper region (free space) can be written as

$$\bar{E}_a = \bar{E}_{a1} + \bar{E}_{a2} \tag{3.4}$$

Note that there are two current sources, $I_p(z)$ and $\bar{I}_{a2}$, giving rise of two electric fields $\bar{E}_{a1}$ and $\bar{E}_{a2}$, respectively. Although $\bar{I}_{a2}$ is induced by $I_p(z)$, it is still treated as an

independent source. $\bar{I}_{a2}$ and $\bar{E}_{a2}$ form one source-field pair in the following analysis for applying the reciprocity theorem.

In case (b), the power line and the voltage source $V_p(z)$ are removed. Instead, a voltage source with amplitude of V is connected to the terminals M and N. The probe is acting as a source now. Assume the current produced by V on the probe is $\bar{I}_b$ and the electric field at the field point due to this current is $\bar{E}_b$. $\bar{I}_b$ and $\bar{E}_b$ make another source-field pair for using the reciprocity theorem.

3.1.3 Implementing reciprocity theorem

The induced current $\bar{I}_{a2}$ in case (a) produces electric field $\bar{E}_{a2}$ and the source current $\bar{I}_b$ in case (b) produces electric field $\bar{E}_b$. Thus, $\bar{I}_b$ and $\bar{I}_{a2}$ are the two sources and $\bar{E}_b$ and $\bar{E}_{a2}$ are the fields respectively excited by them. Replacing the current sources and the electric fields in (3.3) by the following relationships

$$\bar{I}_b(l) \leftrightarrow \mathbf{J_1},\ \bar{E}_b(l) \leftrightarrow \mathbf{E_1},$$
$$\bar{I}_{a2}(l) \leftrightarrow \mathbf{J_2},\ \bar{E}_{a2}(l) \leftrightarrow \mathbf{E_2},$$

(3.3) can be rewritten as

$$\int_{C_{AB}} \bar{E}_b(l) \bullet \bar{I}_{a2}(l) dl = \int_{C_{AB}} \bar{E}_{a2}(l) \bullet \bar{I}_b(l) dl \tag{3.5}$$

where C_{AB} is the contour that covered by the whole sensor system, from the lower ends of the grounding pin P_0 to that for P_L, i.e., from A → Z_0 → M → N → Z_L → B. It includes, from left to right hand side, P_0, Z_0, the sensor, the gap w, Z_L and P_L. In fact, the whole loop of the circuit includes an earth return, too. There should be a current flowing in the earth if it is not perfect conductor. In (3.5), however, the integral term associated with this earth return current hasn't been explicitly expressed because the

effect of the earth return current can be fully accounted in the expression of the incident field $\bar{E}_{a1}$. If the earth is perfect conductor, this return current effect on the incident field can be replaced by an image current. If the earth is lossy, its effect can be represented by a Carson's term in the incident field formulation [26]. The details about this issue will be discussed in later section.

The currents and the electric fields are all vectors and functions of position. Actually, the spatial vector of current can be presented as

$$\bar{I}_{a2}(l) = \hat{a}_l I_{a2}(l) \text{ and } \bar{I}_b(l) = \hat{a}_l I_b(l)$$

where $\hat{a}_l$ is the unit spatial vector pointing in the same direction as the sensor's central axis, and $I_{a2}(l)$, $I_b(l)$ are the magnitudes of the corresponding currents. For the position vector on the sensor

$$d\bar{l} = \hat{a}_l dl$$

With these relations (3.5) is equivalent to

$$\int_{C_{AB}} I_{a2}(l)\bar{E}_b(l) \bullet d\bar{l} = \int_{C_{AB}} I_b(l)\bar{E}_{a2}(l) \bullet d\bar{l} \tag{3.6}$$

Because the induced current $\bar{I}_{a2}$ in the gap is zero, the left-hand side of (3.6) can be rewritten as

$$\text{L.H.S.} = \int_{C_{AM}+C_{NB}} I_{a2}(l)\bar{E}_b(l) \bullet d\bar{l} \tag{3.7}$$

Equation (3.7) is valid because there is no current flowing through the gap if the sensor wire is open. Thus $I_{a2}(gap) = 0$, which causes the integral term $\int_{gap} I_{a2}(l)\bar{E}_b(l) \bullet d\bar{l}$ to be zero.

On the right-hand side, if the gap is small enough, the current through the gap $\bar{I}_b(gap)$ can be approximated as a constant. Additionally, replacing $\bar{E}_{a2}$ by (3.4)

$$\text{R.H.S.} = \int_{C_{AB}} I_b(l)\bar{E}_a(l)\bullet d\bar{l} - \int_{C_{AB}} I_b(l)\bar{E}_{a1}(l)\bullet d\bar{l}$$

Separating the integral over the gap from the first term and simplifying it, the R.H.S. becomes

$$\text{R.H.S.} = \int_{C_{AM}+C_{NB}} I_b(l)\bar{E}_a(l)\bullet d\bar{l} - I_b(gap)V_{oc} - \int_{C_{AB}} I_b(l)\bar{E}_{a1}(l)\bullet d\bar{l} \qquad (3.8)$$

where $I_b(gap)$ is the current I_b at the position of the gap, V_{oc} is the open circuit voltage across MN, and $V_{oc} = -\int_{gap} \bar{E}_a(l)\bullet d\bar{l}$.

The dot product of the electric field with the position vector at the field point is the tangential field component multiplied by the incremental length, i.e., the voltage across the incremental sensor segment. Thus

$$\begin{aligned} \bar{E}_a \bullet d\bar{l} &= dV = I_{a2} Z_w dl \\ \bar{E}_b \bullet d\bar{l} &= dV = I_b Z_w dl \end{aligned} \qquad (3.9)$$

where Z_w is the per unit length surface impedance (Ω/m) of the sensor [42]. Inherently, that (3.9) is valid is based on the thin wire assumption of the sensor wire. The sensor wire is assumed to be thin wire so that the tangential electric field on the surface of the wire is equal to the product of the surface impedance of the wire conduct and the current [42]. In addition, for the lumped impedance Z_0 and Z_L, it is true that

$$\begin{aligned} V_0^a &= I_{a2} Z_0;\ V_L^a = I_{a2} Z_L \\ V_0^b &= I_b Z_0;\ V_L^b = I_b Z_L \end{aligned} \qquad (3.10)$$

where V_0^a is the voltage on Z_0 due to I_{a2}, V_L^a is the voltage on Z_L due to I_{a2}, V_0^b is the voltage on Z_0 due to I_b and V_L^b is the voltage on Z_L due to I_b. Inserting (3.9) and (3.10) into (3.7) and (3.8),

$$\begin{aligned} &\int_{C_{AM}+C_{NB}} I_{a2}(l) I_b(l) Z_S dl + V_0^b I_{a2} - V_L^b I_{a2} \\ &= \int_{C_{AM}+C_{NB}} I_b(l) I_{a2} Z_S dl - I_b(w) V_{oc} - \int_{C_{AB}} I_b(l)\bar{E}_{a1}(l)\bullet d\bar{l} + V_0^a I_b - V_L^a I_b \end{aligned}$$

According to the reciprocity theorem for lumped elements, it holds that

$$V_0^b I_{a2} = V_0^a I_b$$
$$V_L^b I_{a2} = V_L^a I_b$$

Thus, the four terms relative to the lumped impedance in the previous equation can be cancelled. Finally, the relationship between the open-circuit voltage and the incident electric field due to the power line is found as

$$I_b(gap)V_{oc} = -\int_{C_{AB}} I_b(l)\bar{E}_{a1}(l)\bullet d\bar{l}$$

and can be written as

$$V_{oc} = \frac{-1}{I_b(gap)}\int_{C_{AB}} I_b(l)\bar{E}_{a1}(l)\bullet d\bar{l} \tag{3.11}$$

Equation (3.11) is the expression of 'hybrid reciprocity theorem' [43] – [46]. Mapping this theorem to our linear sensor problem it is known that the open circuit voltage at the terminals MN can be calculated if the incident electric field $\bar{E}_{a1}(l)$ due to the power line and the distribution of the current $\bar{I}_b(l)$ when the probe is driven by a voltage source V are known. In (3.11), $\bar{E}_{a1}$ is nothing but the electric field generated by an infinite long horizontal conductor wire above earth without the presence of the sensor. Fortunately, the electromagnetic field exited by an infinite long wire above earth is a canonical problem and has been studied since the 1920's [26]. So electric field in (3.11) is not difficult to obtain. The current distribution $\bar{I}_b(l)$ may be difficult to be determined for the general case, but if the linear sensor is a straight horizontal wire, the current due to a voltage source V can be calculated by the classical transmission theory.

Finding the open circuit voltage is only half of the problem of determining the Thevenin's equivalent circuit. The other half is to calculate the Thevenin's equivalent

impedance Z_{TH}. Fig. 3-4 shows the diagram of the Thevenin's equivalent circuit.

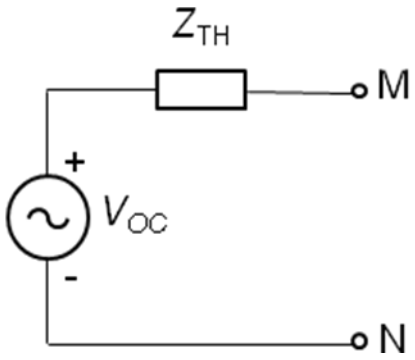

Fig. 3-4 Thevenin's equivalent circuit for the linear sensor system

In fact, Z_{TH} is just the input impedance looking into the port MN and can be calculated by (referred to Fig. 3-3 (b))

$$Z_{TH} = Z_{in} = \frac{\bar{V}}{\bar{I}_b(gap)} \tag{3.12}$$

Since the position of the gap is arbitrarily chosen, the above analysis is applicable at any desired point on the sensor. Given a position on the sensor the Thevenin equivalent circuit at that place can be determined. The induced current at the position of the gap is the short-circuit current of the Thevenin equivalent and found by reconnecting the terminals MN. Then, the induced current distribution on the sensor can be found as

$$\bar{I}_{probe}(l) = \frac{\bar{V}_{oc}(l)}{Z_{TH}(l)} = \frac{-1}{\bar{V}} \int_{C_{AB}} I_b(l) \bar{E}_{a1}(l) \bullet d\bar{l} \tag{3.13}$$

Given the induced current on the sensor, the total electric field distribution is

$$\bar{E}_a(l) = -\bar{I}_{probe}(l) Z_w \tag{3.14}$$

and the voltage drop along the sensor is

$$\bar{V}_{probe}(l) = -\int_C \bar{E}_a \bullet d\bar{l} \tag{3.15}$$

Therefore, (3.11) ~ (3.15) provides us a general set of tools to analysis the linear sensor system defined in the model in Fig. 3-1.

3.1.4 Solutions to the horizontal sensor case

A set of general solutions by the reciprocity approach is given in (3.11) through (3.13). In practice, a more specified model is often interested, in which the linear sensor is specified as a horizontal lossy wire h_w meters above the ground. The whole model is depicted in Fig. 3-5.

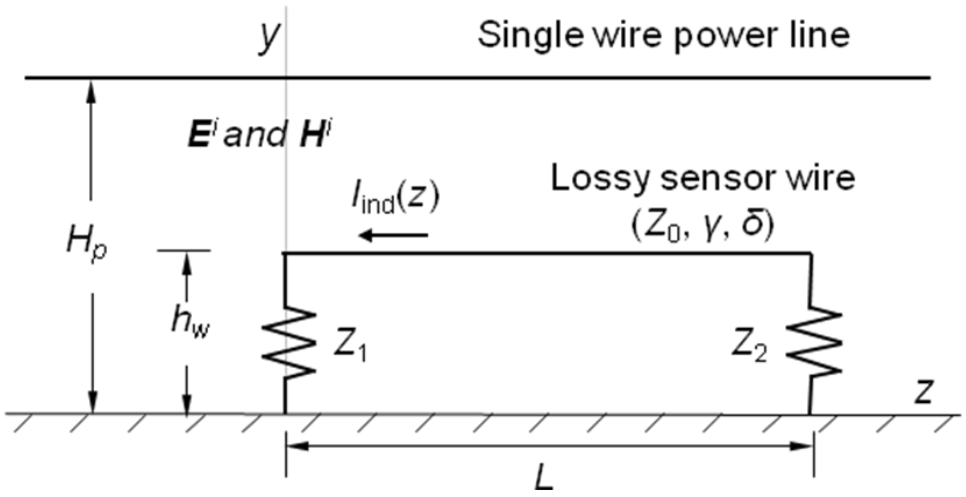

Fig. 3-5 Model of the horizontal lossy wire sensor

In the model the sensor wire is L meters long and is grounded by impedances Z_1 and Z_2 at its left and right ends. The characteristics of the lossy wire are described by γ, δ and Z_0, which are the propagation constant, characteristic length and the characteristic impedance, respectively. The sensor is illuminated by the incident electromagnetic field due to the single-wire power line. The sensor wire is horizontally placed and its axis is along the z direction. In Fig. 3-5, the power line extends in the same direction as the sensor, but in fact this is not necessary. The sensor can be oblique to the power line. This will be shown in following analysis.

From (3.13), the induced current at any point ($0 < z < L$) on the lossy wire can be found as

$$\begin{aligned}\bar{I}_{ind}(z) = \frac{-1}{V}\cdot\Big[&\int_0^{h_w} I_t(z,0)E_y^i(y',z'=0)dy' \\ &-\int_0^{h_w} I_t(z,L)E_y^i(y',z'=L)dy' \\ &+\int_0^{L} I_t(z,z')E_z^i(y'=h_w,z')dz'\Big]\end{aligned} \tag{3.16}$$

where $I_t(z,z')$ is the current at position z' on the lossy wire when it is driven by a voltage source V at $z' = z$, $I_t(z, 0)$ and $I_t(z, L)$ are the currents at $z' = 0$ and $z' = L$ driven by the same voltage source. $E_y^i(y',z'=0)$ is the y-component of the incident electric field along y' axis at $z' = 0$, and $E_y^i(y',z'=L)$ is the similar component at $z' = L$. $E_z^i(y'=h_w,z')$ is the z-component of the incident electric field along z' axis at $y' = h_w$. $I_t(z, z')$ can be found by using the classical transmission line theory as

$$I_t(z,z') = \frac{V}{2Z_0\left(1-\Gamma_1\Gamma_2 e^{-2\gamma L}\right)}\left[e^{-\gamma|z'-z|} - \Gamma_1 e^{-\gamma(z'+z)} - \Gamma_2 e^{-2\gamma L}\left(e^{\gamma(z'+z)} - \Gamma_1 e^{\gamma|z'-z|}\right)\right] \tag{3.17}$$

where $\Gamma_1 = \dfrac{Z_1 - Z_0}{Z_1 + Z_0}$ and $\Gamma_2 = \dfrac{Z_2 - Z_0}{Z_2 + Z_0}$. Inserting (3.17) into (3.16), with some algebra manipulations the induced current in (3.16) can be rewritten as

$$\begin{aligned}\bar{I}_{ind}(z) = \frac{-1}{Z_0 D}\Big[&A_1(z)\int_0^z B_1(z')E_z^i(h,z')dz' + A_2(z)\int_z^L B_3(z')E_z^i(h,z')dz'\Big] \\ -\frac{1}{D}\Big[&A_1(z)\int_0^{h_{sw}} E_y^i(y',z'=0)dy' - A_2(z)\int_0^{h_{sw}} E_y^i(y',z'=L)dy'\Big]\end{aligned} \tag{3.18}$$

where

$$A_1(z) = Z_0\cosh\left[\gamma\left(L-z\right)\right] + Z_2\sinh\left[\gamma\left(L-z\right)\right]$$

$$A_2(z) = Z_0\cosh\left(\gamma z\right) + Z_1\sinh\left(\gamma z\right)$$

$$B_1(z') = Z_0\cosh\left(\gamma z'\right) + Z_1\sinh\left(\gamma z'\right)$$

$$B_3(z') = Z_0\cosh\left[\gamma\left(L-z'\right)\right] + Z_2\sinh\left[\gamma\left(L-z'\right)\right]$$

$$D = \left(Z_0 Z_1 + Z_0 Z_2\right)\cosh\left(\gamma L\right) + \left(Z_0^2 + Z_1 Z_2\right)\sinh\left(\gamma L\right)$$

Equations (3.16) and (3.18) are the solutions to the induced current of the horizontal sensor model that are identical but of different form. According to these results, the induced current can be determined at any point on the sensor if the incident E fields at the position of the sensor are known. There is no requirement that the relative position of the power line to the sensor wire is known as long as the power line is horizontal and high enough ($H_p >> h_w$). Thus the power line can be parallel, oblique, or perpendicular to the sensor wire. The results in (3.16) and (3.18) will be used in Chapter 4 and 5 for the cases of the perpendicular linear sensor and the parallel linear sensor.

3.2 Approach by model of per-unit-length voltage and current sources

As shown, the reciprocity theorem can be used to find the induced current for the very general model as depicted in Fig. 3-1. Now the model in Fig. 3-5 is considered and a further assumption that the ground is perfect conductor is made. The new model is shown in Fig. 3-6. For this problem a method based on classical transmission line theory uses voltage-and-current sources to replace the external excitation.

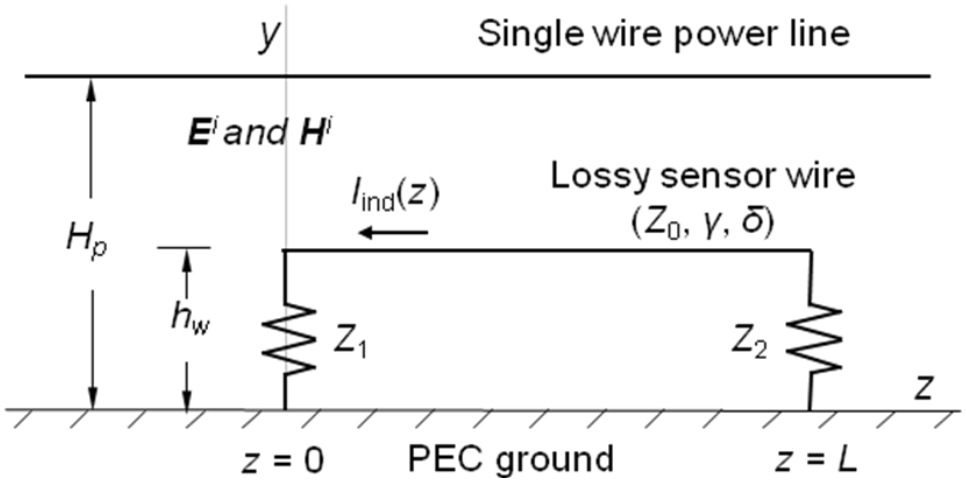

Fig. 3-6 Model of a horizontal lossy linear sensor over perfect conductor ground

In Fig. 3-6, the horizontal lossy wire probe is h_w meters above the perfect ground and grounded by impedances Z_1 and Z_2 at the left and right hand ends. It has a length of L meters. The characteristics of the lossy wire are described by γ, δ and Z_0, which are the propagation constant, characteristic length and the characteristic impedance, respectively. The sensor is illuminated by the incident electromagnetic field and it can be replaced by the continuous distributed per-unit-length induced voltage source and the per-unit-length induced current source [42], as depicted in Fig. 3-7.

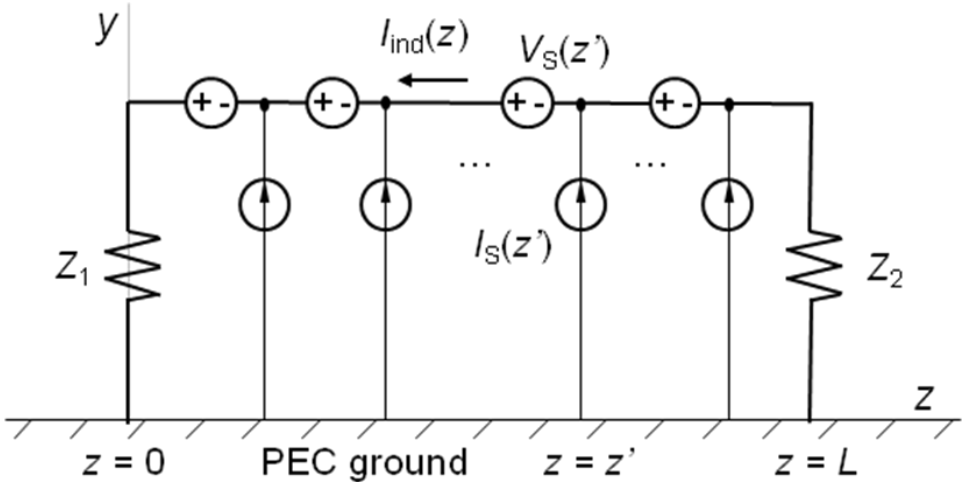

Fig. 3-7 Replacing the external excitation with per-unit-length induced voltage and current sources

These two per-unit-length equivalent sources are functions of position (z). According to [42] the per-unit-length induced voltage and current source can be written as

$$\bar{V}_S(z') = -j\omega\mu_0 \int_0^{h_w} H_x^i(y', z')dy' \tag{3.19}$$

$$\bar{I}_S(z') = -j\omega c_w \int_0^{h_w} E_y^i(y', z')dy' \tag{3.20}$$

where ω is the angular frequency of the incident field, μ_0 is the permeability of free space, c_w is the per-unit-length capacitance of the lossy wire and E_y^i and H_x^i are the incident electric and magnetic field respectively. The induced current is to be determined by the superposition of the current due to each source pair. From (3.19) and (3.20), it is known that the voltage source is related to the magnetic field coupling and the current source is related to the electric field coupling.

Consider the case for that the lossy wire sensor is driven by only one set of the voltage and current sources (at $z = z'$) as shown in Fig. 3-8.

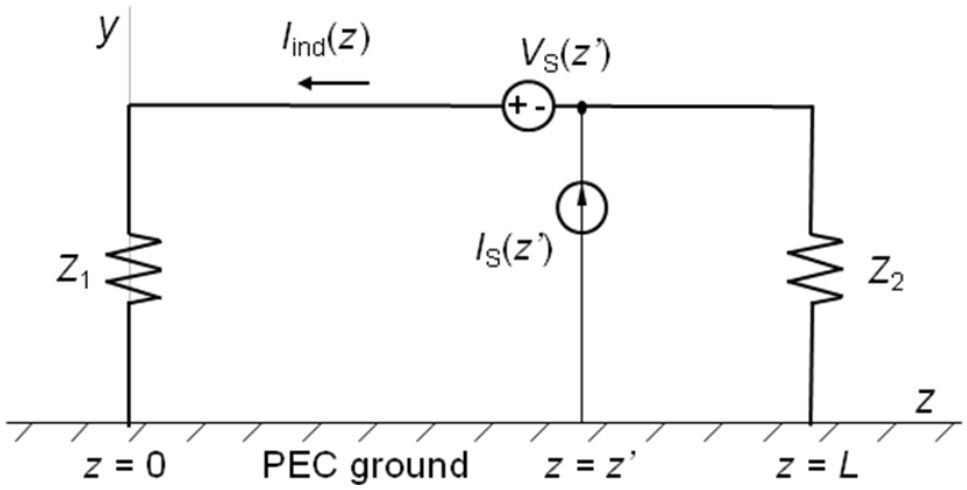

Fig. 3-8 The sensor driven by only one set of the per-unit-length induced voltage and current sources (at $z = z'$)

The circuit on the left hand side of the two sources ($0 < z < z'$) can be substituted by the input impedance looking into the left side of the source pair and the right part of the circuit ($z' < z < L$) can be substituted by the input impedance looking into the

right side of the source pair. The equivalent circuit of the model in Fig. 3-8 is then obtained as shown in Fig. 3-9.

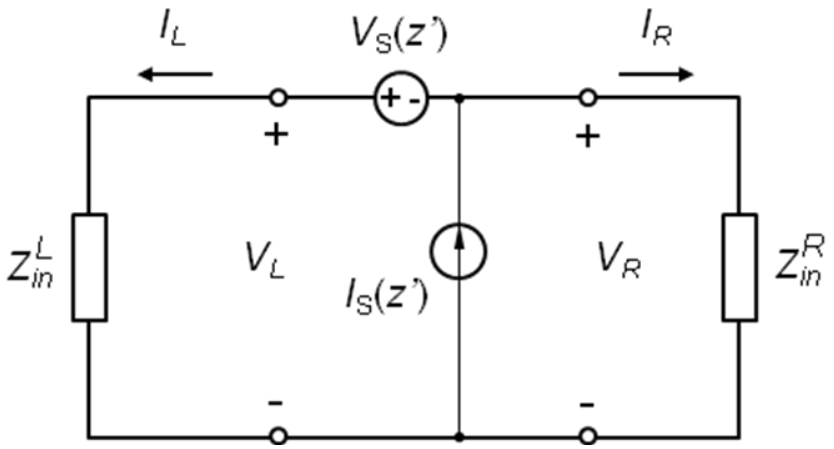

Fig. 3-9 Equivalent circuit of the model driven by only one pair of the per-unit-length induced voltage and current sources

Z_{in}^L and Z_{in}^R are the input impedances looking into the left and right sides of the source. The voltages cross them, V_L and V_R, are found by

$$V_L(z') = \frac{Z_{in}^L}{Z_{in}^L + Z_{in}^R} \cdot V_s(z') + \frac{Z_{in}^L Z_{in}^R}{Z_{in}^L + Z_{in}^R} \cdot I_s(z')$$

$$V_R(z') = -\frac{Z_{in}^R}{Z_{in}^L + Z_{in}^R} \cdot V_s(z') + \frac{Z_{in}^L Z_{in}^R}{Z_{in}^L + Z_{in}^R} \cdot I_s(z')$$

These two voltages can be determined by the classical transmission line theory. Then the distribution of the induced current on the lossy wire can be found. Assume the induced current is denoted as $I(z', z)$, where z is the position variable and z' indicates the position of the voltage-and-current source. On the right and left side of the source the induced current $I(z', z)$ can be written as

$$I(z', z)\big|_{z \geq z'} = \frac{A_1(z)}{Z_0 D}\left[-B_1(z')\bar{V}_S(z') + B_2(z')Z_0\bar{I}_S(z')\right] \tag{3.21}$$

$$I(z',z)\big|_{z\le z'} = \frac{A_2(z)}{Z_0 D}\left[B_3(z')\bar{V}_S(z') + B_4(z')Z_0\bar{I}_S(z')\right] \tag{3.22}$$

where

$$A_1(z) = Z_0\cosh\left[\gamma\left(L-z\right)\right] + Z_2\sinh\left[\gamma\left(L-z\right)\right]$$

$$A_2(z) = Z_0\cosh\left(\gamma z\right) + Z_1\sinh\left(\gamma z\right)$$

$$B_1(z') = Z_0\cosh\left(\gamma z'\right) + Z_1\sinh\left(\gamma z'\right)$$

$$B_2(z') = Z_1\cosh\left(\gamma z'\right) + Z_0\sinh\left(\gamma z'\right)$$

$$B_3(z') = Z_0\cosh\left[\gamma\left(L-z'\right)\right] + Z_2\sinh\left[\gamma\left(L-z'\right)\right]$$

$$B_4(z') = Z_2\cosh\left[\gamma\left(L-z'\right)\right] + Z_0\sinh\left[\gamma\left(L-z'\right)\right]$$

$$D = \left(Z_0Z_1 + Z_0Z_2\right)\cosh\left(\gamma L\right) + \left(Z_0^2 + Z_1Z_2\right)\sinh\left(\gamma L\right)$$

Next consider that the lossy wire is driven by continuously distributed per-unit-length induced voltage and current sources. The induced current in the wire is obtained by integrating the induced current due to single set of source along the length of the wire:

$$\bar{I}_{ind}(z) = -\int_0^z I(z',z)\big|_{z\ge z'}dz' + \int_z^L I(z',z)\big|_{z\le z'}dz' \tag{3.23}$$

Inserting (3.21) and (3.22) into (3.23), the induced current on the lossy wire sensor at position z can be obtained as

$$\begin{aligned}\bar{I}_{ind}(z) = &-\frac{A_1(z)}{Z_0 D}\int_0^z\left[B_1(z')\bar{V}_S(z') + B_2(z')Z_0\bar{I}_S(z')\right]dz' \\ &-\frac{A_2(z)}{Z_0 D}\int_z^L\left[B_3(z')\bar{V}_S(z') - B_4(z')Z_0\bar{I}_S(z')\right]dz'\end{aligned} \tag{3.24}$$

where

$$A_1(z) = Z_0\cosh\left[\gamma\left(L-z\right)\right] + Z_2\sinh\left[\gamma\left(L-z\right)\right]$$

$$A_2(z) = Z_0\cosh\left(\gamma z\right) + Z_1\sinh\left(\gamma z\right)$$

$$B_1(z') = Z_0 \cosh(\gamma z') + Z_1 \sinh(\gamma z')$$

$$B_2(z') = Z_1 \cosh(\gamma z') + Z_0 \sinh(\gamma z')$$

$$B_3(z') = Z_0 \cosh\left[\gamma(L - z')\right] + Z_2 \sinh\left[\gamma(L - z')\right]$$

$$B_4(z') = Z_2 \cosh\left[\gamma(L - z')\right] + Z_0 \sinh\left[\gamma(L - z')\right]$$

$$D = (Z_0 Z_1 + Z_0 Z_2)\cosh(\gamma L) + (Z_0^2 + Z_1 Z_2)\sinh(\gamma L)$$

$$\bar{V}_S(z') = -j\omega\mu_0 \int_0^{h_w} H_x^i(y', z')dy'$$

$$\bar{I}_S(z') = -j\omega c_w \int_0^{h_w} E_y^i(y', z')dy'$$

It appears that the results using the reciprocity approach for the induced current shown in (3.16) and (3.18) are different from (3.24). But it is shown below in Section 3.3 that they are identical.

3.3 Relationship between the two approaches

In this section the relation between the result (3.16) derived using the reciprocity approach and the result (3.24) using the per-unit-length-source approach is studied. Since the reciprocity method is more general, the analysis will be started from (3.16).

First, consider the current distribution shown in (3.17). Replacing the exponential functions in it by the hyperbolic sine and cosine functions results in

$$I_t(z, z') = \begin{cases} \dfrac{V}{Z_0 D} A_1(z) B_1(z') & 0 \le z' \le z \\ \dfrac{V}{Z_0 D} A_2(z) B_3(z') & z \le z' \le L \end{cases} \tag{3.25}$$

where

$$A_1(z) = Z_0 \cosh\left[\gamma(L - z)\right] + Z_2 \sinh\left[\gamma(L - z)\right]$$

$$A_2(z) = Z_0 \cosh(\gamma z) + Z_1 \sinh(\gamma z)$$

$$B_1(z') = Z_0 \cosh(\gamma z') + Z_1 \sinh(\gamma z')$$

$$B_3(z') = Z_0 \cosh\left[\gamma(L - z')\right] + Z_2 \sinh\left[\gamma(L - z')\right]$$

$$D = (Z_0 Z_1 + Z_0 Z_2)\cosh(\gamma L) + (Z_0^2 + Z_1 Z_2)\sinh(\gamma L)$$

The derivative of this current with respect to *z'* is found as

$$\frac{\partial I_t(z,z')}{\partial z'} = \begin{cases} \dfrac{\gamma V}{Z_0 D} A_1(z) B_2(z') & 0 \le z' \le z \\ \dfrac{-\gamma V}{Z_0 D} A_2(z) B_4(z') & z \le z' \le L \end{cases} \tag{3.26}$$

where

$$B_2(z') = Z_1 \cosh(\gamma z') + Z_0 \sinh(\gamma z')$$

$$B_4(z') = Z_2 \cosh\left[\gamma(L - z')\right] + Z_0 \sinh\left[\gamma(L - z')\right]$$

Second, pulling the current out of the first two integrals of (3.16) results in

$$\begin{aligned} \bar{I}_{ind}(z) = \frac{-1}{V} \cdot \Big[& I_t(z,0) \int_0^{h_w} E_y^i(y', z' = 0) dy' \\ & - I_t(z,L) \int_0^{h_w} E_y^i(y', z' = L) dy' \\ & + \int_0^L I_t(z,z') E_z^i(y' = h_w, z') dz' \Big] \end{aligned} \tag{3.27}$$

Using the definitions of the per-unit-length current source (3.20) in (3.27) yields

$$\bar{I}_{ind}(z) = \frac{-1}{V} \cdot \left[\frac{I_t(z,0)\bar{I}_S(0)}{-j\omega c_w} - \frac{I_t(z,L)\bar{I}_S(L)}{-j\omega c_w} + C_1 \right] \tag{3.28}$$

where

$$C_1 = \int_0^L I_t(z,z') E_z^i(y' = h_w, z') dz' .$$

Third, from the Maxwell's equation

$$\nabla \times \bar{E} = -j\omega\mu_0 \bar{H}$$

the *x* component of the H field can be obtained as

$$-j\omega\mu_0 H_x^i(y', z') = -\frac{\partial E_y^i(y', z')}{\partial z'} + \frac{\partial E_z^i(y', z')}{\partial y'} \tag{3.29}$$

Integrating both sides of (3.29) with respect to *y'* from 0 to h_w and using the definition of the per-unit-length voltage source (3.19) leads to

$$E_z^i(y' = h_w, z') - E_z^i(y' = 0, z') = \bar{V}_S(z') + \int_0^{h_w} \frac{\partial E_y^i(y', z')}{\partial z'} dy' \tag{3.30}$$

If the assumption $E_z^i(y' = 0, z') = 0$ is made (i.e., the ground is assumed to be perfect conductor), (3.30) becomes

$$E_z^i(y' = h_w, z') = \bar{V}_S(z') + \int_0^{h_w} \frac{\partial E_y^i(y', z')}{\partial z'} dy' \tag{3.31}$$

Inserting (3.31) into the term C_1 in (3.28) and using (3.25) result in

$$C_1 = \frac{V}{Z_0 D}\left[A_1(z)\int_0^z B_1(z')\bar{V}_S(z')dz' + A_2(z)\int_z^L B_3(z')\bar{V}_S(z')dz' \right] + M \tag{3.32}$$

where

$$M = \int_0^{h_w}\int_0^L I_t(z, z')\frac{\partial E_y^i(y', z')}{\partial z'} dz'dy'$$

If the inner integral of *M* is evaluated by parts, *M* becomes

$$M = \frac{I_t(z, L)\bar{I}_S(L)}{-j\omega c_w} - \frac{I_t(z, 0)\bar{I}_S(0)}{-j\omega c_w} - \int_0^{h_w}\int_0^L E_y^i(y', z')\frac{\partial I_t(z, z')}{\partial z'} dz'dy'$$

Then, by using (3.20), (3.26) and the fact that $\gamma/Z_0 = j\omega c_w$, the term *M* can be rewritten as

$$\begin{aligned} M = & \frac{I_t(z, L)\bar{I}_S(L)}{-j\omega c_w} - \frac{I_t(z, 0)\bar{I}_S(0)}{-j\omega c_w} \\ & + \frac{V}{Z_0 D}\left[A_1(z)\int_0^z B_2(z')Z_0\bar{I}_S(z')dz' - A_2(z)\int_z^L B_4(z')Z_0\bar{I}_S(z')dz' \right] \end{aligned} \tag{3.33}$$

Finally, combining (3.28), (3.32), and (3.33) gives the result for the induced current in the form of per-unit-length sources as

$$\begin{aligned}\bar{I}_{ind}(z) = &-\frac{A_1(z)}{Z_0 D}\int_0^z \left[B_1(z')\bar{V}_S(z') + B_2(z')Z_0\bar{I}_S(z')\right]dz' \\ &-\frac{A_2(z)}{Z_0 D}\int_z^L \left[B_3(z')\bar{V}_S(z') - B_4(z')Z_0\bar{I}_S(z')\right]dz'\end{aligned} \tag{3.34}$$

Obviously, (3.34) is identical to (3.24). The two approaches, the reciprocity and the per-unit-length induced sources, give identical results for the induced current of the lossy sensor wire of Fig. 3-5. Note that (3.24) or (3.34) can only be obtained based on the assumption made between (3.30) and (3.31), which is

$$E_z^i\left(y' = h_w, 0\right) = 0 \tag{3.35}$$

This assumption is equivalent to assuming that the ground is perfect conductor. In (3.18) there is no requirement on the property of the earth. Therefore, the result from the reciprocity is more general than that from the per-unit-length induced sources method.

In practice, the earth is not perfect but lossy. As introduced in Chapter 1, at low frequency the earth is rather transparent than perfect for the calculation of magnetic field. For lossy earth, the axial electric field E_z^i, which is nonzero, contributes to the inductive coupling of the sensor. Therefore, the assumption (3.35) may not be valid for the real earth case. Under this circumstance, the assumption (3.35) should not be made and (3.31) should be written as

$$E_z^i\left(y' = h_w, z'\right) = \bar{V}_S(z') + E_z^i\left(y' = 0, z'\right) + \int_0^{h_w}\frac{\partial E_y^i\left(y', z'\right)}{\partial z'}dy' \tag{3.36}$$

Then, redefine the induced per-unit-length voltage source $\bar{V}_S(z')$ (related to the inductive coupling) and change the notation to $\bar{V}_S'(z')$. It can be rewritten as

$$\bar{V}_S'(z') = -j\omega\mu_0\int_0^{h_w} H_x^i(y', z')dy' + E_z^i\left(y' = 0, z'\right) \tag{3.37}$$

The effect of the lossy earth on the inductive coupling is embodied in axial incident electric field added to (3.37). Using $\bar{V}_S'(z')$ to substitute $\bar{V}_S(z')$ in (3.24) results in

$$\begin{aligned}\bar{I}_{ind}(z) = &-\frac{A_1(z)}{Z_0 D}\int_0^z \left[B_1(z')\bar{V}_S'(z') + B_2(z')Z_0\bar{I}_S(z')\right]dz' \\ &-\frac{A_2(z)}{Z_0 D}\int_z^L \left[B_3(z')\bar{V}_S'(z') - B_4(z')Z_0\bar{I}_S(z')\right]dz'\end{aligned} \tag{3.38}$$

where $\bar{V}_S'(z')$ is defined by (3.37) and all the other variables or symbols are the same as defined in (3.24). After the modification being made to $\bar{V}_S(z')$, (3.38) is valid for the case that the earth is lossy. It is unconditionally identical to the result by the reciprocity method (3.18) and more general than (3.24). In Chapter 5, (3.38) will be used for the analysis of the parallel linear sensor because for this kind of sensor the inductive (magnetic) coupling is involved and the effect of the lossy earth on the induced current cannot be ignored.

In [46] another approach using a model of the continuous distributed voltage source is provided to formulate the induced current of a lossy transmission line which is the analogue to the lossy sensor wire of Fig. 3-5. The result is also proved to be identical to (3.34), which means that the three approaches validate each other.

Either the reciprocity method or the per-unit-length source method has its own advantages and should be utilized in different situations. The reciprocity result, (3.16) or (3.18), only involves the incident electric field. It can be use in the case that the electric field is easy to find. The advantage of (3.24) is that the effects of the electric and magnetic couplings are explicitly separated. Thus, when both of the electric and magnetic coupling are involved (3.24) will be more helpful for analysis.

CHAPTER 4

PERPENDICULAR LINEAR SENSORS

As discussed in Chapter 3, the position of the linear sensor relative to the power transmission line varies for different sensors. In this chapter interest is the kind of linear sensor that is placed to be horizontal over the ground and perpendicular to the conductors of the power transmission line. Thus, it is called the perpendicular linear sensor. It has been introduced in Chapter 1 that the dominant magnetic fields of the infinite long power line above the earth are transverse to its direction [36]. Since the sensor is perpendicular to the power line, the plane containing the circuit loop of the sensor must be transverse to the power line and parallel to the magnetic flux plane. Therefore, no magnetic flux couples with the sensor loop, as illustrated in Fig. 4-1. In other words, there is no magnetic coupling picked up by the sensor. Thus, only electric field coupling related to the capacitance of the sensor will be involved.

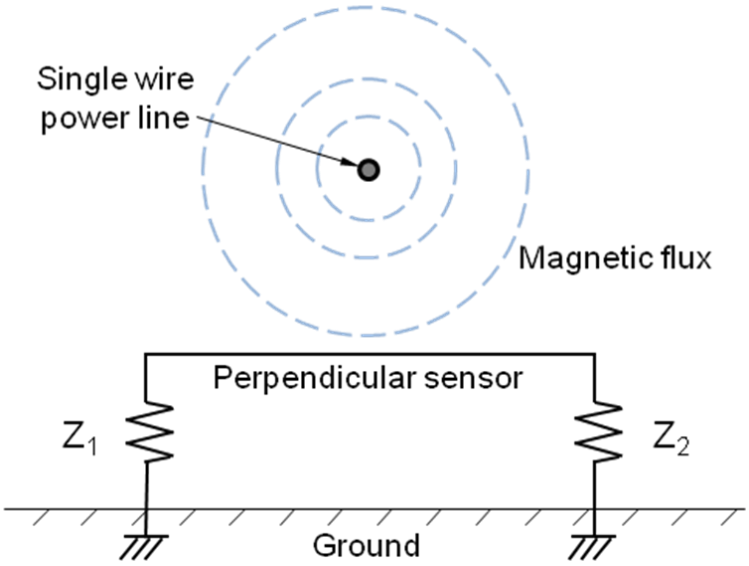

Fig. 4-1 Circuit loop of the perpendicular linear sensor is transverse to the power line and parallel to the magnetic flux plane of the power line.

The perpendicular linear sensor can be designed for monitoring the power line sag, which may caused by either conductor heating or ice coating. Heating can increase the line sag by weakening the tensile strength of the conductor and increasing its length [47] – [49]. Ice coating on the power line elongates the conductor by increasing the weight of it [50], [51]. The perpendicular linear sensor can also be made to detect the negative/zero sequence mode of the power line voltage. In the following sections, a model of the perpendicular sensor is first introduced and the theory of how the sensor works is derived in 4.1. Again, the induced current of the sensor under the excitation from the power line is the focus. Second, the effects of different parameters, such as the length, height, resistance and capacitance of the sensor wire, on the induced current are discussed in 4.2. Applications using the perpendicular sensors in sag monitoring and negative mode detection are introduced in 4.3.

4.1 Model and theories

A model of the perpendicular linear sensor system is shown in Fig. 4-2. In this model, the sensor is a horizontal lossy wire, L meters long and h_w meters above the ground. The sensor wire is placed perpendicular to a single-wire power line, which is H_p meters above the ground and energized by a voltage source of V_p (kV). As mentioned before, for the perpendicular linear sensor only the electric coupling, i.e., the transverse electric field, will be involved in analyzing the theory. Thus the ground is assumed to be perfect electric conductor (PEC) because of the quasi-static

approximation for the field calculation. The sensor wire is grounded through two impedances, Z_1 and Z_2, at its two ends. The sensor wire itself can be lossy, for which case it is characterized by its resistance per unit length r_w (Ω/m) and the capacitance per unit length c_w (pF/m). More generally, these parameters, r_w and c_w, can be functions of position along the sensor.

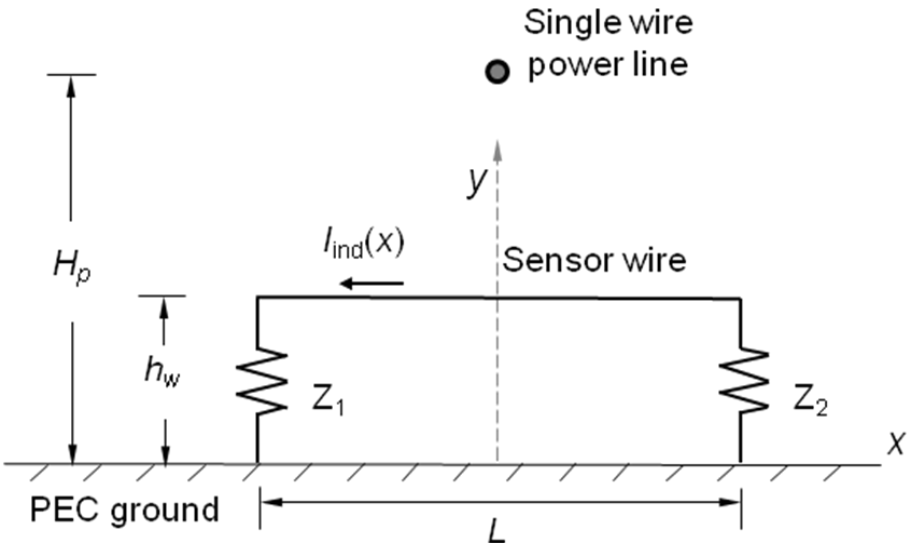

Fig. 4-2 Model of a perpendicular linear sensor system.

The sensor wire with the impedances Z_1 and Z_2, the earth return and the connecting wires form the circuit loop of the sensor system. Under the excitation of the incident field from the power line a current is induced in the sensor wire. By using the reciprocity approach developed in Chapter 3, this induced current can be analytically determined. The model defined in Fig. 4-2 is similar to that shown in Fig. 3-5 except that the position of the sensor relative to the power line is not specified in the latter one. But this is not a problem when utilizing the results of the latter model in this perpendicular sensor model. Adapting (3.16) to the model in Fig. 4-2 gives the induced current as

$$\bar{I}_{ind}(x) = \frac{-1}{V} \cdot \left[\int_0^{h_w} I_t(x, -L/2) E_y^i(x' = -L/2, y') dy' \right.$$
$$- \int_0^{h_w} I_t(x, L/2) E_y^i(x' = L/2, y') dy' \qquad (4.1)$$
$$\left. + \int_{-L/2}^{L/2} I_t(x, x') E_x^i(x', y' = h_w) dx' \right]$$

where E_x^i and E_y^i are the x and y components of the unperturbed incident electric fields (i.e., in the absence of the sensor) from the power line, respectively. $I_t(x, x')$ is the testing current at x' when a voltage source of amplitude V is applied at the open terminals at x. $I_t(x, -L/2)$ and $I_t(x, L/2)$ are the testing currents at the left and right ends of the sensor wire. If the wires connecting the sensor wire to ground through Z_1 and Z_2 have very small propagation constant, compared to that for the sensor wire, the current doesn't change along the vertical segments on the left and right ends of the sensor wire. This can be realized by using wires that have better conductivity (smaller per-unit-length resistance) and much thinner diameter (smaller per-unit-length capacitance) than the sensor wire as the connecting wires. Given this assumption in (4.1), the testing currents in the first and second terms in the bracket can be pulled out of the integrals, which leaves only the incident field E_y^i in the integrands. Since $E_y^i = -\frac{\partial V_{sp}}{\partial y}$, where V_{sp} is the space potential due to the power line, (4.1) can be rewritten as

$$\bar{I}_{ind}(x) = \frac{-1}{V} \cdot \left[-I_t(x, -L/2) V_{sp}(x' = -L/2, y') \right.$$
$$+ I_t(x, L/2) V_{sp}(x' = L/2, y') \qquad (4.2)$$
$$\left. + \int_{-L/2}^{L/2} I_t(x, x') E_x^i(x', y' = h_w) dx' \right]$$

Evaluating the integral of the third term in (4.2) using integration by parts and using

$E_x^i = -\dfrac{\partial V_{sp}}{\partial x}$ results in

$$\begin{aligned}\bar{I}_{ind}(x) = \frac{-1}{V}\cdot\Big[&-I_t(x,-L/2)V_{sp}(x'=-L/2,y') + I_t(x,L/2)V_{sp}(x'=L/2,y') \\ &+ I_t(x,-L/2)V_{sp}(x'=-L/2,y') - I_t(x,L/2)V_{sp}(x'=L/2,y') \\ &- \int_{-L/2}^{L/2}\frac{\partial I_t(x,x')}{\partial x'}V_{sp}(x',y'=h_w)dx'\Big]\end{aligned}$$

The first four terms cancel leaving that

$$\bar{I}_{ind}(x) = \frac{1}{V}\int_{-L/2}^{L/2}\frac{\partial I_t(x,x')}{\partial x'}V_{sp}(x',y'=h_w)dx' \tag{4.3}$$

The first term in the integrand of (4.3) is the derivative of the testing current, which is basically determined by the parameters of the wire probe and the matching condictions at both ends of it. The second term is the space potential due to the incident electric field. It is determined by the energized voltage V_p and the configuration of the power line. Therefore, equation (4.3) indicates that the induced current in the probe contains information about the incident electric field, i.e. information about the voltage and configurations of the power line. This matches with the previous argument that the perpendicular sensor is only sensitive to the electric field.

The distribution of the testing current can be obtained by adapting (3.17) to this case. With a variable changing from *z* to *x* and a shifting in coordinate of +*L*/2, (3.17) can be rewritten as

$$I_t(x,x') = \frac{V\left[e^{-\gamma|x'-x|} - \Gamma_1 e^{-\gamma(L+x'+x)} - \Gamma_2 e^{-2\gamma L}\left(e^{\gamma(L+x'+x)} - \Gamma_1 e^{\gamma|x'-x|}\right)\right]}{2Z_0\left(1-\Gamma_1\Gamma_2 e^{-2\gamma L}\right)} \tag{4.4}$$

where Z_0 is the characteristic impedance of the sensor wire, $\Gamma_1 = \dfrac{Z_1 - Z_0}{Z_1 + Z_0}$ and

$\Gamma_2 = \dfrac{Z_2 - Z_0}{Z_2 + Z_0}$ are the reflection coefficients at the left and right hand sides of the sensor respectively. The partial derivative of the testing current with respect to *x'* is:

for $-L/2 < x' < x$:

$$\frac{\partial I_t(x,x')}{\partial x'} = \frac{V\gamma}{2Z_0\left(1-\Gamma_1\Gamma_2 e^{-2\gamma L}\right)}\left[e^{-\gamma(x-x')} + \Gamma_1 e^{-\gamma(L+x'+x)} - \Gamma_2 e^{-2\gamma L}\left(e^{\gamma(L+x'+x)} + \Gamma_1 e^{\gamma(x-x')}\right)\right] \tag{4.5a}$$

and for $x < x' < L/2$:

$$\frac{\partial I_t(x,x')}{\partial x'} = \frac{V\gamma}{2Z_0\left(1-\Gamma_1\Gamma_2 e^{-2\gamma L}\right)}\left[-e^{-\gamma(x'-x)} + \Gamma_1 e^{-\gamma(L+x'+x)} - \Gamma_2 e^{-2\gamma L}\left(e^{\gamma(L+x'+x)} - \Gamma_1 e^{\gamma(x'-x)}\right)\right] \tag{4.5b}$$

The testing current in (4.4) and its derivative with respect to *x'* in (4.5a) and (4.5b) can also be written in forms of hyperbolic sine and cosine functions as

$$I_t(x,x') = \begin{cases} \dfrac{V}{Z_0 D} A_1(x) B_1(x') & -L/2 \le x' \le x \\ \dfrac{V}{Z_0 D} A_2(x) B_3(x') & x \le x' \le L/2 \end{cases} \tag{4.6}$$

where

$$A_1(x) = Z_0 \cosh\left[\gamma\left(L/2 - x\right)\right] + Z_2 \sinh\left[\gamma\left(L/2 - x\right)\right]$$

$$A_2(x) = Z_0 \cosh\left[\gamma\left(L/2 + x\right)\right] + Z_1 \sinh\left[\gamma\left(L/2 + x\right)\right]$$

$$B_1(x') = Z_0 \cosh\left[\gamma\left(L/2 + x'\right)\right] + Z_1 \sinh\left[\gamma\left(L/2 + x'\right)\right]$$

$$B_3(x') = Z_0 \cosh\left[\gamma\left(L/2 - x'\right)\right] + Z_2 \sinh\left[\gamma\left(L/2 - x'\right)\right]$$

$$D = \left(Z_0 Z_1 + Z_0 Z_2\right)\cosh\left(\gamma L\right) + \left(Z_0^2 + Z_1 Z_2\right)\sinh\left(\gamma L\right)$$

The derivative of this current with respect to *z'* is then found as

$$\frac{\partial I_t(x,x')}{\partial x'} = \begin{cases} \dfrac{\gamma V}{Z_0 D} A_1(x) B_2(x') & -L/2 \le x' \le x \\ \dfrac{-\gamma V}{Z_0 D} A_2(x) B_4(x') & x \le x' \le L/2 \end{cases} \tag{4.7}$$

where

$$B_2(x') = Z_1 \cosh\left[\gamma\left(L/2 + x'\right)\right] + Z_0 \sinh\left[\gamma\left(L/2 + x'\right)\right]$$

$$B_4(x') = Z_2 \cosh\left[\gamma\left(L/2 - x'\right)\right] + Z_0 \sinh\left[\gamma\left(L/2 - x'\right)\right]$$

By using (4.7), the induced current in (4.3) can be rewritten in the forms of hyperbolic sine and cosine functions as

$$\begin{aligned} \bar{I}_{ind}(x) = {} & \frac{\gamma A_1(x)}{Z_0 D} \int_{-L/2}^{x} B_2(x') V_{sp}(x', y' = h_w) dx' \\ & - \frac{\gamma A_2(x)}{Z_0 D} \int_{x}^{L/2} B_4(x') V_{sp}(x', y' = h_w) dx' \end{aligned} \tag{4.8}$$

where $A_1(x)$, $A_2(x)$, $B_2(x')$, $B_4(x')$, and D are defined as before.

As previously discussed, the perpendicular sensor involves only electric field (i.e., capacitive) coupling, which is similar to that of the point probe introduced in Chapter 2. In fact, the model in Fig. 4-2 can reduce to a point probe if the sensor is assumed to be very short and open circuited at one of its ends. Consider that the length of the sensor L is short enough that $|\gamma L| << 1$ and the sensor is opened at $x = L/2$ (equivalent to setting $Z_2 = \infty$). The model with these assumptions is shown in Fig. 4-3.

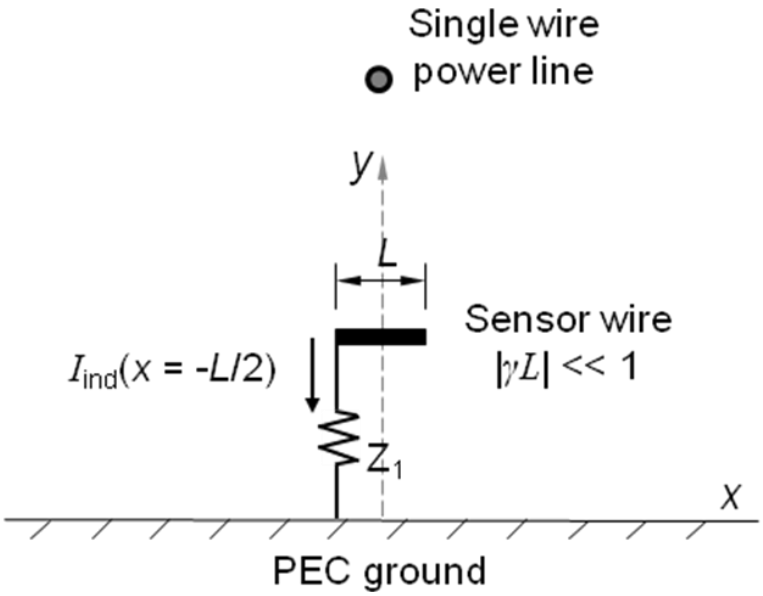

Fig. 4-3 A perpendicular linear sensor reduces to point probe when its length is very short and is opened at one of its end (x = L/2 for this case).

For the hyperbolic sine and cosine functions, given $|\gamma L| << 1$ it yields that

$$\cosh(\gamma u) \approx 1 \text{ and } \sinh(\gamma u) \approx 0$$

where $|u| < L$. With these approximations (4.7) reduces to

$$\frac{\partial I_t(x,x')}{\partial x'} = \begin{cases} \dfrac{\gamma V Z_1}{Z_0(Z_1+Z_2)} & -L/2 \le x' \le x \\ \dfrac{-\gamma V Z_2}{Z_0(Z_1+Z_2)} & x \le x' \le L/2 \end{cases} \tag{4.9}$$

The induced current can be rewritten as

$$\bar{I}_{ind}(x) = \frac{\gamma Z_1}{Z_0(Z_1+Z_2)} \int_{-L/2}^{x} V_{sp}(x', y' = h_w)dx' - \frac{\gamma Z_2}{Z_0(Z_1+Z_2)} \int_{x}^{L/2} V_{sp}(x', y' = h_w)dx'$$

Since $|\gamma L| << 1$, the space potential doesn't change much along the sensor wire and it can be assumed constant over the whole length of the sensor wire. Then, it yields that

$$\bar{I}_{ind}(x) = \frac{\gamma V_{sp,-L/2}}{Z_0(Z_1+Z_2)} \left[(x - L/2) Z_1 - (L/2 - x) Z_2 \right]$$

where $V_{sp,-L/2}$ is the space potential at ($x = -L/2$, $y = h_w$) and chosen to represent the space potential value over the sensor. Taking a further step by using the assumption

that $Z_2 = \infty$ and the fact that $\gamma / Z_0 = j\omega c_w$ (c_w is the per-unit-length capacitance of the sensor) the induced current now can be written as

$$\bar{I}_{ind}(x) = -j\omega c_w \left(L/2 - x\right) V_{sp,-L/2} \qquad \left(-L/2 \le x \le L/2\right) \tag{4.10}$$

Therefore, the induced current in the grounding wire at $x = -L / 2$ is found as

$$\bar{I}_{ind}(-L/2) = -j\omega (c_w L) V_{sp,avg} \tag{4.11}$$

Equation (4.11) gives the same result as (2.8) since $c_w L$ is the self-capacitance of the sensor. Therefore a perpendicular sensor can reduce to a point probe if the length of the sensor is short ($|\gamma L| << 1$).

As shown in (4.3) or (4.11) the perpendicular linear sensor collects information about the value of the space potential of the power line in. Many factors affect this average value and hence the induced current of the sensor. The sag of the power line conductor is one among those factors because the space potential is strongly related to the configurations of the power line conductor. A perpendicular linear sensor can be designed as a line-sag monitor such that the change of the line sag is recognized by measuring the induced current. The discussion of this part will be introduced in section 4.2.

In a similar way, the perpendicular sensor provides information not only the magnitude but also about the phase angle of the space potential. One example of an application using the phase angle information is the use of the perpendicular sensor to detect the negative and zero components in the power line voltage. If the single-wire power line in Fig. 4-2 is replaced by a three-phase power line, any change of the symmetrical components of the power line voltage will cause the profile of the phase

distribution of the incident space potential to change. The perpendicular sensor can be designed to be sensitive to this phase change and used as a negative or zero sequence voltage detector. The detailed analysis and discussion will be introduced in section 4.3.

4.2 Sag monitoring by perpendicular linear sensor

It has been qualitatively known from the previous discussion that the current induced on the sensor wire depends on the characteristics of the power line. If, for example, the quantitative relation between the induced current and the line sag can be analyzed, it is possible to design and built a sag sensor using the perpendicular linear sensor. To examine this possibility, computer simulations based on the models of a horizontal-configured and a delta-configured three-phase power line were conducted.

4.2.1 Power line models and parameters

Consider the two power transmission lines, configurations of which are shown in Fig. 4-4 (a) and (b), respectively.

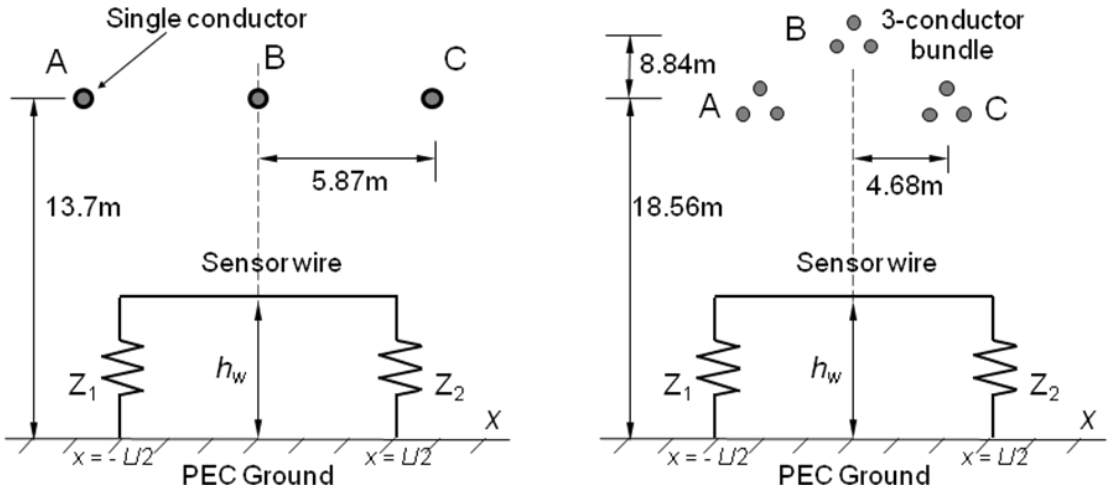

(a) Model A: 230 kV horizontal line (b) Model B: 500 kV delta line

Fig. 4-4 Geometries of the perpendicular wire sensor and two types of three-phase power transmission line

Model A is a single-wire three-phase 230 kV horizontal line and Model B is a bundled three-phase 500 kV delta line. They are the power line models used to conduct the simulations for this chapter. Their configurations and parameters of the corresponding perpendicular sensors are listed in Table 4-1.

Table 4-1 Power line configures and sensor parameters

	Power line in Model A	Power line in Model B	Perpendicular sensor
Line to line voltage (kV)	230	500	
Conductor height (m)	13.72	–	3 (if not specified)
Conductor length (m)	–	–	6 (if not specified)
Single conductor diameter (m)	0.035	0.033	0.0042
Phase spacing (m)	5.87	–	–
Span length (m)	200	300	–
# of conductors / bundle	1	3	–
Spacing between bundle conductors (m)	–	0.433	–
Position of each phase (m)	A: (-5.87, 13.72) B: (0, 13.72) C: (5.87, 13.72)	A: (0, 27.40) B: (4.b68, 18.56) C: (- 4.68, 18.56)	–

The heights of the power line conductor in the table refer to as the conductor heights at the mid-point of one span assuming two towers at the ends of the span have same height over the level ground. The sensor is a conducting wire with the resistance per unit length r_w specified at 0.001 Ω/m (approximately the resistance of a one meter long copper wire with diameter of 4.2 mm). The per unit length capacitance and

inductance of the sensor are calculated by [42]

$$c_w = \frac{2\pi\varepsilon_0}{\ln\left(2H_p / a_w\right)} \tag{4.12}$$

$$l_w = \frac{\mu_0}{2\pi}\ln\left(2H_p / a_w\right) \tag{4.13}$$

where a_w is the radius of the sensor wire. With r_w, c_w, and l_w the characteristic impedance Z_0 and the propagation constant γ of the sensor wire can be determined as [42]

$$Z_0 = \sqrt{\frac{r_w + j\omega l_w}{j\omega c_w}} \tag{4.14}$$

$$\gamma = \sqrt{\left(r_w + j\omega l_w\right) j\omega c_w} \tag{4.15}$$

There are many factors that need to be considered when designing a perpendicular sensor for monitoring the power line sag. These factors include the length of the sensor wire, the height it is placed above the ground, and the impedances Z_1 and Z_2 connected the sensor to the ground. In the following sections, the effects of these factors on the sag monitoring will be examined by numerical simulations, in which the induced current on the sensor is calculated by (4.8) under different conditions.

4.2.2 Effect of setting of Z_1 and Z_2

To start the analysis, it is necessary to have some perceptual knowledge of the induced current of the perpendicular linear sensor. Fig. 4-5 (a) and (b) respectively show the magnitude of the induced current on the sensor in Model A and Model B when the sensor is connected to the ground through impedances Z_1 = 100Ω and Z_2 = 100Ω. Z_1 and Z_2 are not set to zero because, in practice, the earth resistance is never zero. Even

when the sensor wire is directly connected to ground, the grounding resistance due to the earth should still be taken account into the model. 100Ω is a reasonable value of the grounding resistance. Fig. 4-6 shows the corresponding phase angles. The power line sag is set to zero for these simulations. The results obtained by (4.8) are represented by solid lines in the figures. To validate (4.8), a method [52] based on the concept of superposition to calculate the induced current is used. The results are presented in circles in the figures.

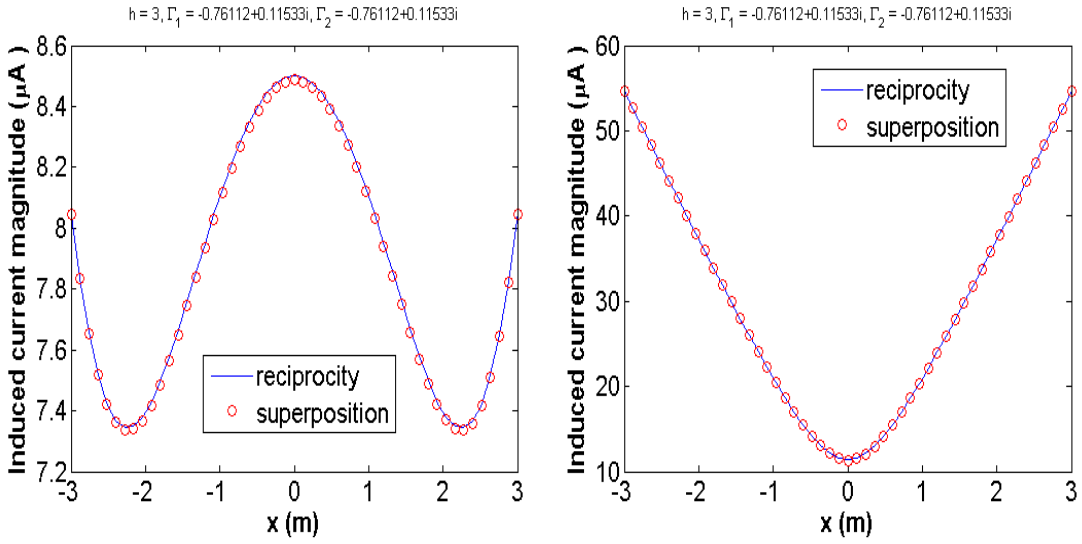

(a) Model A: 230 kV horizontal line (b) Model B: 500 kV delta line

Fig. 4-5 Magnitude of the induced current on the sensor when Z_1 = 100Ω and Z_2 = 100Ω

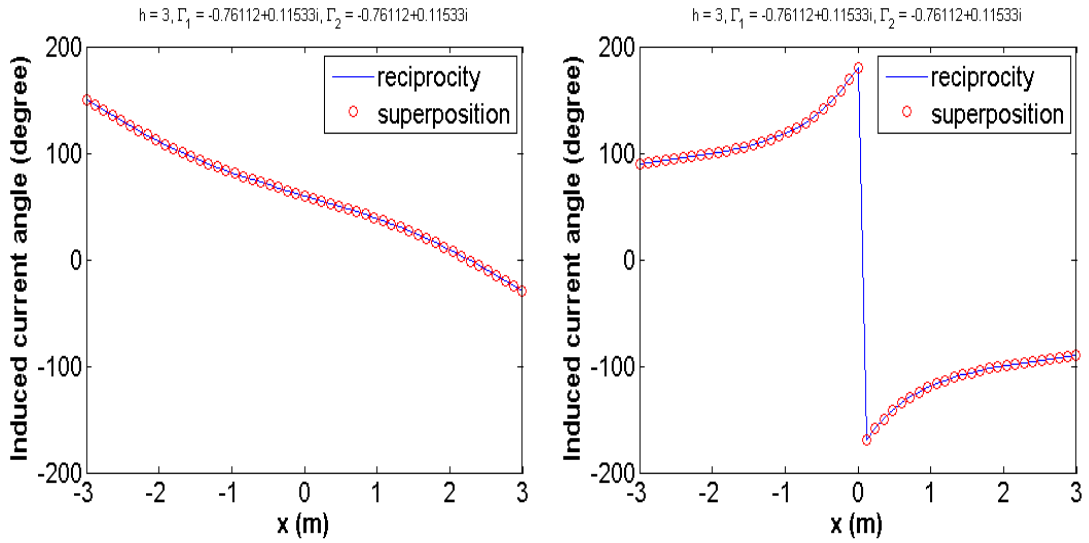

(a) Model A: 230 kV horizontal line (b) Model B: 500 kV delta line

Fig. 4-6 Phase angle of the induced current on the sensor when Z_1 = 100Ω and Z_2 = 100Ω

The magnitudes of the induced current of the two models are both symmetrical about the midpoint of the sensor wire because of the symmetry of the models. The space potential is received symmetrically on the left and right half of the sensor and derivative of the testing current in (4.7) has symmetry about the midpoint of the sensor. Given these facts, it seems qualitatively that the induced current at the midpoint should always be zero if $Z_1 = Z_2$ because the current flows symmetrically from the midpoint to the two ends of the sensor. But this is not true, as shown in Fig. 4-5. According to (4.3), the induced current is determined by the integration of the derivative of the testing current multiplied by the space potential. From Fig. 2-5, the phase angle distribution of the space potential is not mirrored by central vertical axis. Consequently, the induced currents on the two halves of the sensor are not symmetrical, in phase angle, about the central axis and don't always cancel each other. Thus, the induced current at the midpoint can be nonzero.

Z_1 and Z_2 can be selected arbitrarily. Their values determine the reflection coefficients at both ends of the sensor, hence affect the induced current. There is no a priori about which values of Z_1 and Z_2 are better for the sag monitoring. According to multiple simulations, when Z_1 = 100Ω and Z_2 = ∞ (directly grounded at x = -L/2 and open at x = +L/2) the induced current has larger magnitude of the induced current at x = -L/2, as shown in Fig. 4-7. This may be a good point for the sensor design because, in practice, the larger the magnitude of the current the easier the measurement.

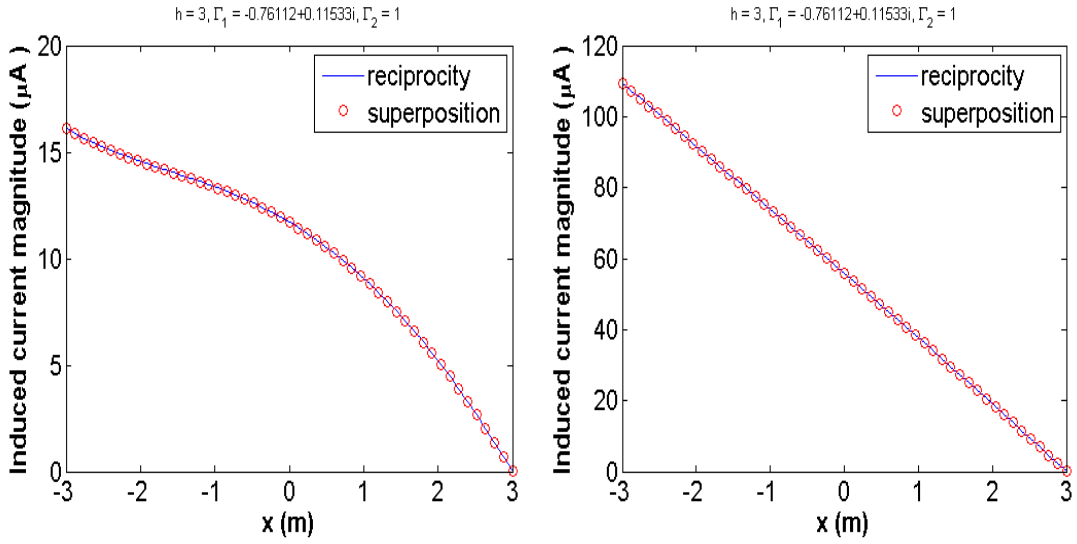

(a) Model A: 230 kV horizontal line (b) Model B: 500 kV delta line

Fig. 4-7 Magnitude of the induced current on the sensor when Z_1 = 100Ω and Z_2 = ∞

Generally speaking, the reason why the induced current of this setting is larger than that for the previous setting (Z_1 = 100Ω and Z_2 = 100Ω) is because with one end open the induced current in the whole sensor flows in the same direction and the effective part of the sensor for receiving the incident field becomes larger.

4.2.3 Effect of sensor length

According to (4.3) or (4.8), the length of the sensor wire, L, affects the induced

current. The induced currents at the left end (x = - L/2) were calculated for various values of L. Results for several different line sag values are plotted in Fig. 4-8 (a) and (b) for Model A and Model B, respectively. The sensor is connected to the ground directly (Z_1 = 100Ω and Z_2 = 100Ω).

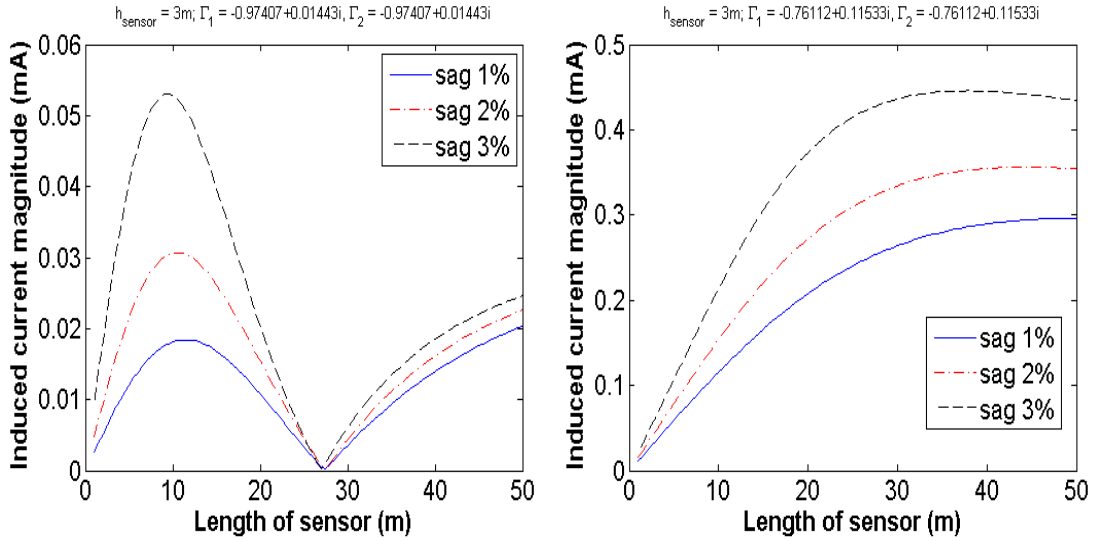

(a) Model A: 230 kV horizontal line (b) Model B: 500 kV delta line

Fig. 4-8 Induced current at x = - L/2 vs. length of the sensor (Z_1 = 100Ω and Z_2 = 100Ω)

For both Model A and B, the induced current saturates when the sensor is long enough. This makes sense because if the sensor is very long the contribution to the induced current from the part of the sensor far away from the center becomes negligible due to the attenuation of the incident field. But, for Model A, it is interesting that the induced current has a null at about L = 27m in each of the three curves, as shown in Fig. 4-8 (a). Results from multiple simulations show that the sensor length causing the null is approximately proportional to the horizontal spacing between the phase conductors of the power line and almost independent of the line sag. By further simulations, it is found that the integration of the space potential alone

(just assume the derivative of the testing current in (4.3) is 1) over the sensor wire has very similar shape as the curves in Fig. 4-8 (a) and a null occurs at about the same sensor length as for the induced current, shown in Fig. 4-9. According to (4.3), this argument is valid because for the given parameters of the sensor wire the derivative of the testing current doesn't change much along the sensor and the shape of the integration is not distorted by it. Under this condition, the null is mainly determined by the characteristic of the distribution of the space potential, which is determined by the configuration of the power line.

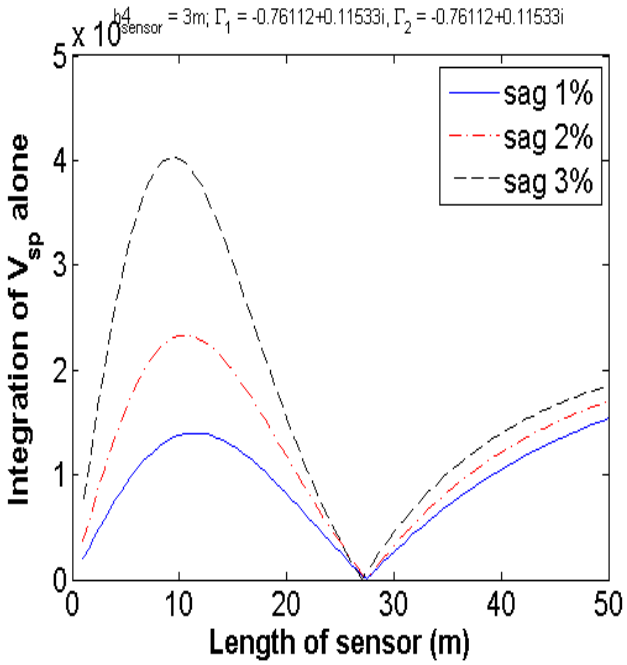

Fig. 4-9 Integration of space potential alone over the sensor wire for different lengths of sensor. The shapes of the curves are very similar to that in Fig. 4-8 (a).

If one end of the sensor is open (set $Z_2 = \infty$), similar results for the induced current can be obtained. Fig. 4-10 (a) and (b) show the induced current of Model A and B, respectively, at $x = -L/2$ changing with the sensor length for the setting of $Z_1 =$ 100Ω and $Z_2 = \infty$.

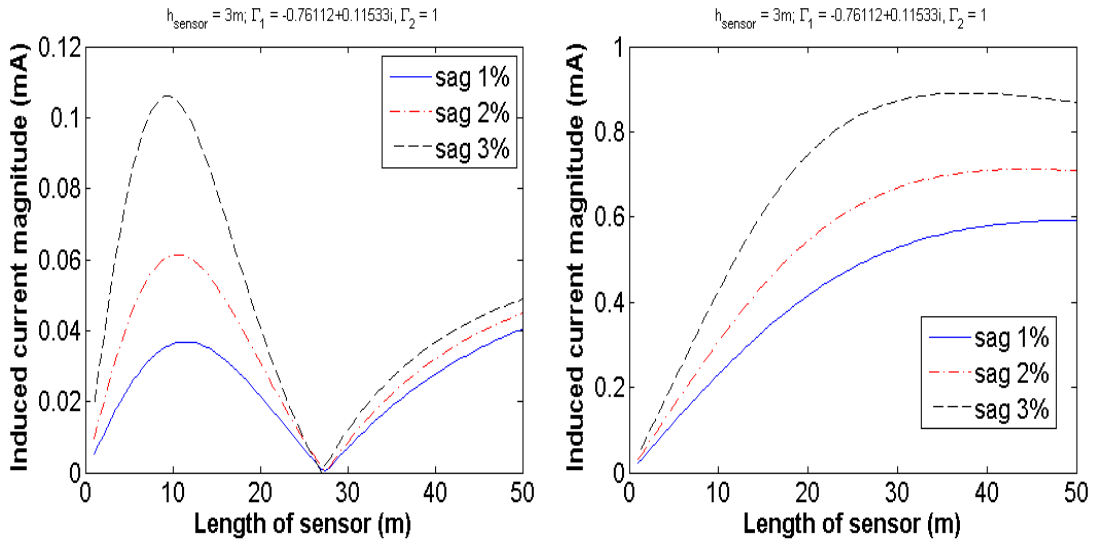

(a) Model A: 230 kV horizontal line (b) Model B: 500 kV delta line

Fig. 4-10 Induced current at $x = -L/2$ vs. length of the sensor ($Z_1 = 100\Omega$ and $Z_2 = \infty$)

The induced current of Model A has a null occurring at about the same sensor length as in Fig. 4-8 (a). This fact supports the previous argument that the null is determined by the characteristic of the space potential distribution because the derivative of the testing current doesn't change much along the sensor for the given parameters. The characteristic null in the induced current may be helpful in designing the sag sensor. It can be noticed from Fig. 4-10 (a) that for the sensor length less than the value causing the null the induced current increases rapidly with increasing sag, which implies that the sensor has better sensitivity to sag for lengths in that range. For this reason any sensor of length from 5 to 10 meters seems to be good choice for sag monitoring. Given concerns of cost and ease of installation, however, the length of the sensor would not be expected to be too long. Thus, any values close to five meters would probably be an optimal choice of the length of the sensor.

The sensitivity of a sensor can be evaluated in many ways. For the sag sensor, how much magnitude change in induced current can be gained over the given range of

sag values may be an important parameter. Hence, a factor S_c can be defined to show the sensitivity of the sensor

$$S_c = \frac{|I_{\max}|}{|I_{\min}|(s_{\max} - s_{\min})} \tag{4.16}$$

where $I_{\max}$ and $I_{\min}$ are the maximum and minimum of induced current in the given range of the line sag, $s_{\max}$ and $s_{\min}$ (in %) are the line sag values that cause $I_{\max}$ and $I_{\min}$, respectively. For a monotonically increasing current, S_c represents the steepness of the curve. But for a current curve that has multiple peaks or valleys S_c may not be the appropriate parameter.

4.2.4 Effect of sensor height

Obviously, the height of the sensor wire above the ground affects the induced current. The higher the position of the probe the higher the magnitude of the space potential, which in general will cause higher magnitude of induced current. Fig. 4-11 shows the results for Model A.

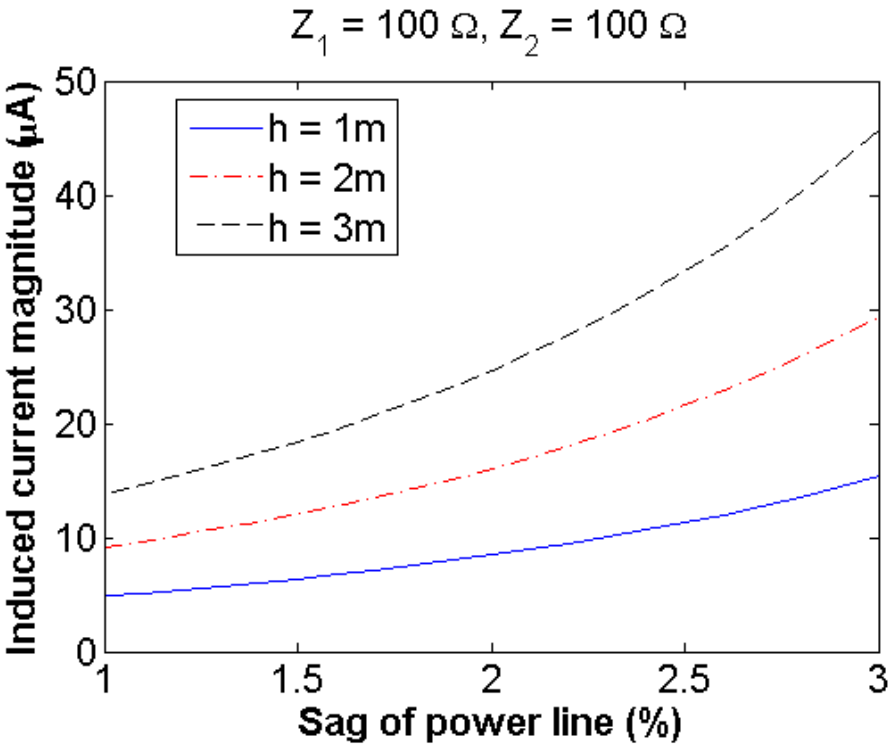

Fig. 4-11 Sensor height vs. line sag for Model A (Z_1 = 100Ω and Z_2 = 100Ω)

The induced current increases when the sag becomes large. But it can be seen that the change of the sensor height doesn't change the sag sensitivity much. Thus, the height may not be a key factor for designing the sensor. To get a larger magnitude of induced current, which makes measurements easier, a larger sensor height may be desired. But there are restrictions on sensor height so that safety codes relating to conductor clearance are not violated.

4.2.5 Discussion on characteristic parameters of the sensor wire

The characteristic impedance Z_0 and the propagation constant γ are defined in (4.14) and (4.15). Therefore, the characteristic parameters, such as r_w, c_w, and l_w, of the sensor wire determine the distribution of the testing current and its derivative, through which they can affect the result of the induced current. Fig. 4-12 shows the induced current vs. the sensor length for different values of r_w.

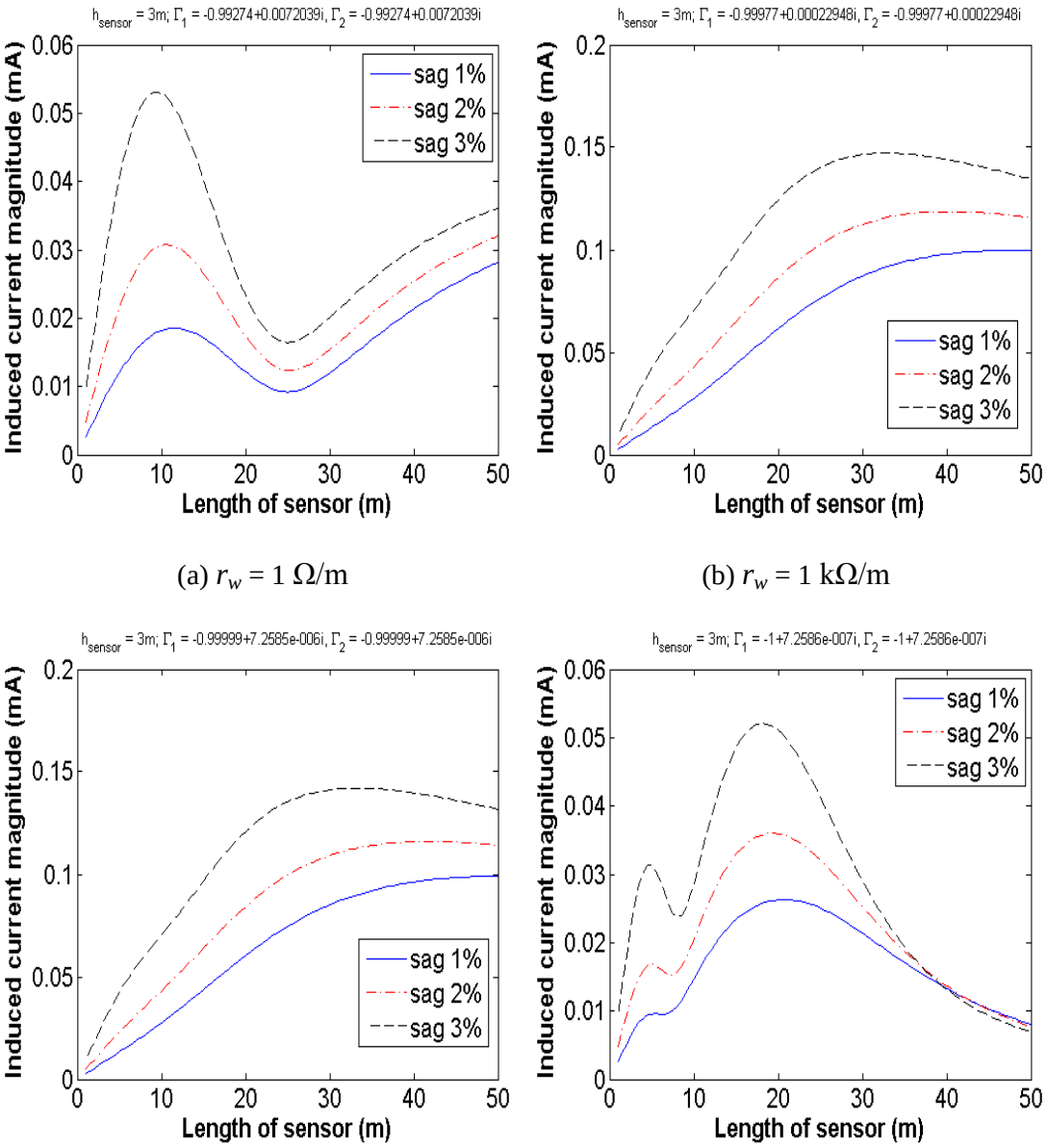

(a) r_w = 1 Ω/m

(b) r_w = 1 kΩ/m

(c) r_w = 1 MΩ/m

(d) r_w = 100 MΩ/m

Fig. 4-12 Induced current at x = - L/2 vs. length of the sensor for different r_w (Model A, Z_1 = 100Ω and Z_2 = 100Ω)

From Fig. 4-8 (a) and Fig. 4-12, the induced current changes with the changing of r_w. For the design of perpendicular sensor, the optimal value of r_w should be the one that can provide good sensitivity of the sensor and be easily achieved in practice. For the cases r_w = 0.001 Ω/m and r_w = 1 Ω/m, the induced current has better sensitivity to line sag for the small sensor length range. Since the copper wire that has r_w = 0.001

Ω/m is very easy to get, r_w = 0.001 Ω/m can be a good choice of the per-unit-length resistance of the line sag sensor.

The per-unit-length capacitance, c_w, also affects the induced current and the results for different values of c_w are shown in Fig. 4-13.

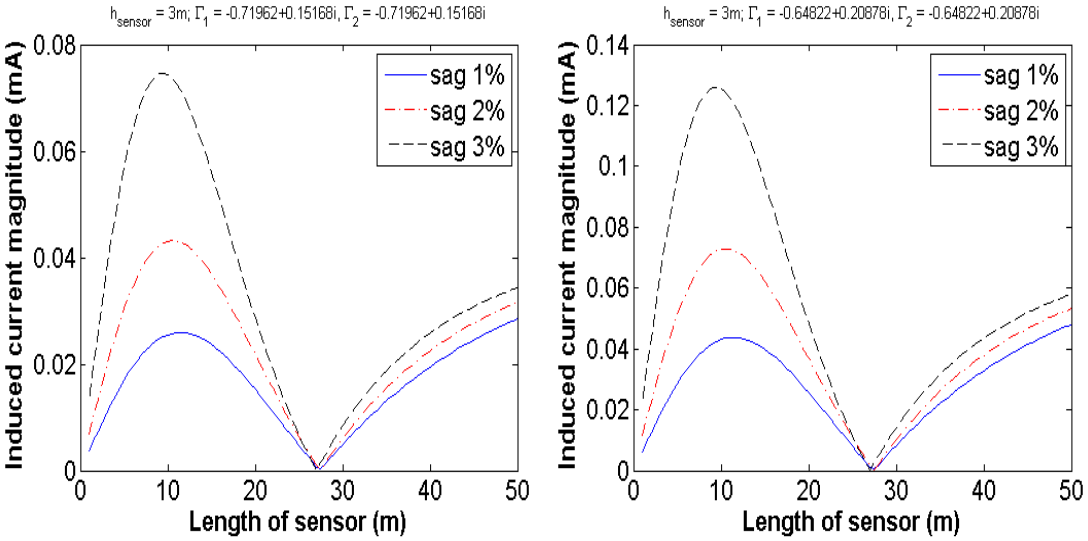

(a) a_w = 0.021 m (b) a_w = 0.21 m

Fig. 4-13 Induced current at x = - L/2 vs. length of the sensor for different c_w (Model A, Z_1 = 100Ω, Z_2 = 100Ω, and r_w = 0.001 Ω/m)

In these simulations, c_w is changed by using different values of radius of the sensor wire. Compared to the case for Fig. 4-8 (a), the sensor wire radius increases 10 and 100 times in Fig. 4-13 (a) and (b) respectively. The corresponding c_w then becomes ln(10) = 2.3 and ln(100) = 4.6 times of the original value. It can be seen from these figures that c_w doesn't change shapes of the curves but it affects the magnitude of the induced current. The larger the c_w, i.e., the radius, the larger the magnitude of the induced current. Based on this fact, the radius of the sensor wire can be determined according to the requirement of the current measurement.

All the factors discussed above, for power lines as described in Model A and

Model B, should be examined to determine optimal designs for building a good perpendicular linear sensor for sag monitoring. A set of these parameters of the sensor chosen based on above discussions is listed in Table 4-2 and makes a design of the sensor used as power line sag monitor.

Table 4-2 Designs of the perpendicular linear sensor for sag monitoring

Sensor length, L	3 m
Sensor height, h_w	2 m
Diameter of sensor, d_w	4.2 mm
Resistance per unit length, r_w	0.001 Ω/m
Setting of Z_1 and Z_2	Z_1 = 100 Ω, Z_2 = 100 Ω

4.3 Negative sequence mode detection by perpendicular linear sensor

Since a perpendicular linear sensor can provide some information about the space potential, which is a phasor, it is possible to utilize the phase angle of the space potential and design the sensor to detect the negative or zero sequence components of the power line voltage. Assume the power line in Fig. 4-2 is a balanced three-phase line with 120 degree phase shifts between each phase. As discussed in Chapter 2 (section 2.2), the negative and zero sequence components of the applied line voltage can cause the profile of the phase angle distribution of the space potential to change, which consequently causes the induced current in the sensor to change. Usually, the presences of the negative and/or zero sequence voltage components are signs of the abnormal conditions or faults occurring somewhere in the power system. If the

perpendicular sensor is designed to be able to respond to those unusual components of voltage, it can be used for detecting abnormal conditions or faults. Here, an example of this kind of design is illustrated in Fig. 4-14.

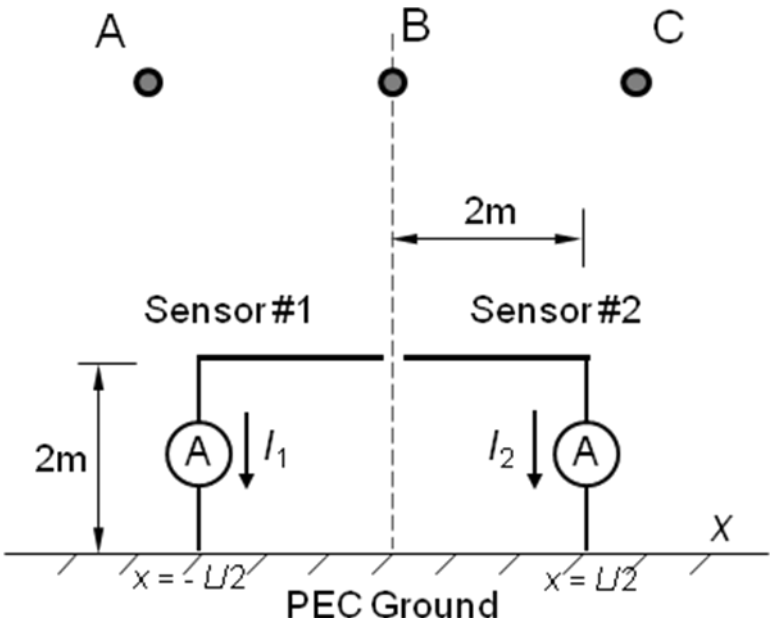

Fig. 4-14 An example of using perpendicular linear sensors to detect negative sequence voltage

In this model, the power line is the same as Model A in Fig. 4-4. Instead of using one single sensor two separate sensors are symmetrically placed on the left and right hand side of the central axis. Each of the sensors is two meters long, two meters above the ground, open at one end and grounded by a resistance 100Ω at the other end. The induced currents, I_1 and I_2, of the sensors are measured by an ammeter connected to the grounding wire. The other parameters of the sensor are the same as provided in Table 4-2. First, the induced currents given the different individual sequence modes are checked. Fig. 4-15 (a) and (b) show the magnitude of induced currents vs. the line sag for the positive mode and negative mode of the power line voltage. The phase corresponding phase angles are shown in Fig. 4-16 (a) and (b).

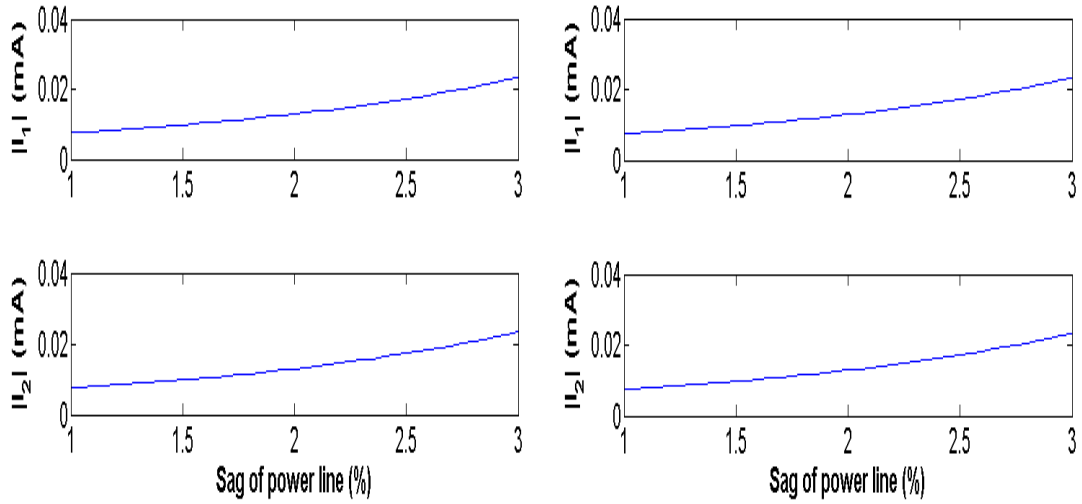

(a) positive mode (b) negative mode

Fig. 4-15 Magnitude of the induced current I_1 and I_2: (a) positive mode; (b) negative mode

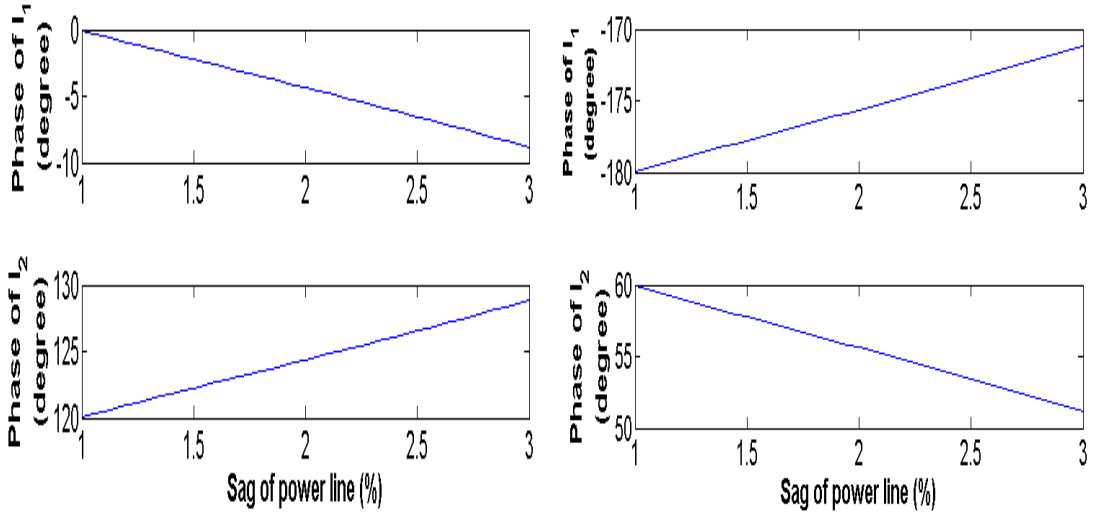

(a) positive mode (b) negative mode

Fig. 4-16 Phase angle of the induced current I_1 and I_2: (a) positive mode; (b) negative mode

From these figures, it is known that I_1 and I_2 have the same magnitude but different phase angle profiles for positive and negative mode. Thus, if I_1 and I_2 are shifted with some proper angles (about ± 30 °for this case), the total current of them I_{tot} = I_1 + I_2 can be set to zero for the positive mode but nonzero for the negative mode.

Fig. 4-17 shows the sensors with the phase shifters.

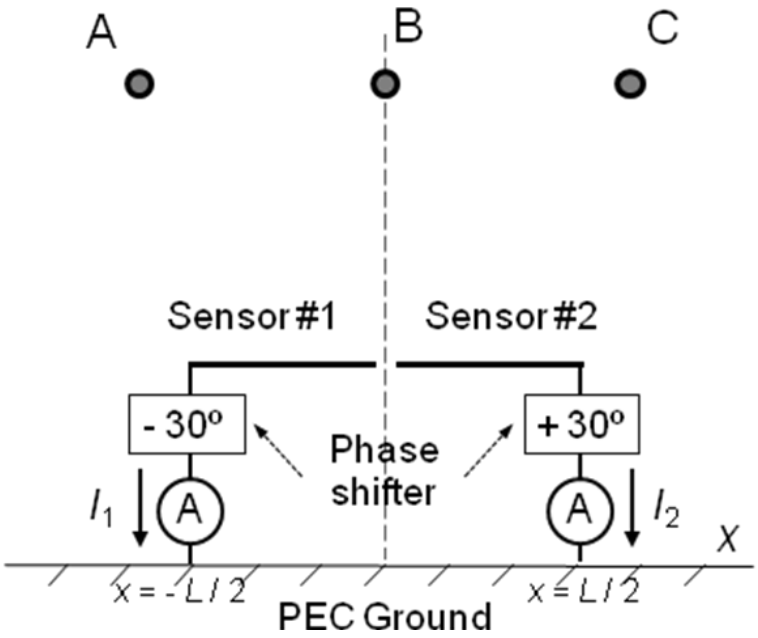

Fig. 4-17 Design of perpendicular linear sensors with phase shifters to detect negative mode

With the given parameters: h_w = 2m and $L/2$ = 2m, the proper phase shift values are +30 °for I_1 and -30 °for I_2. After the phase shift is applied, the total currents for the positive, negative, and zero modes are shown in Fig. 4-18 as a function of line sag.

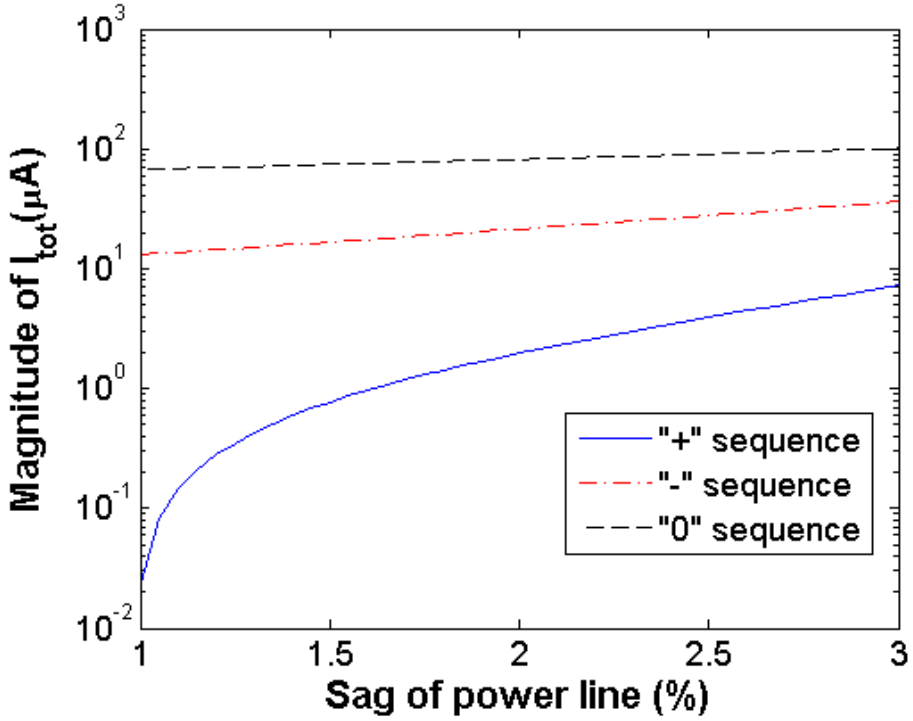

Fig. 4-18 Magnitude of total currents I_{tot} for the positive, negative, and zero modes after ±30 °phase shifting

Due to the cancellation of I_1 and I_2, the total current for positive mode is very small compared to that for negative mode. In the sag range of 1% to 3%, the total current for the positive sequence mode is at least 5 and 15 times smaller than that for the negative and zero sequence modes respectively. The current magnitude of zero sequence mode is about 3 ~ 4 times that for negative mode. When the line sag is close to 1%, this magnitude difference between the three modes becomes even larger. The magnitude of the current can be divided into three levels: I_{tot} < 7μA, 14μA < I_{tot} < 35μA and I_{tot} > 70μA for sag from 1% to 3%. These correspond to the positive, negative and zero sequence modes respectively of the power line. If assume only single sequence mode existing in the power line voltage, the mode can be determined by checking the level of the current magnitude. As shown in Fig. 4-18, this standard works well for the sag range from 1% to 3%, which means despite the effect of the

line sag change the sensor can detect the sequence mode change of the power line voltage. In another word, the sensor can detect negative/zero sequence voltage in the power line even when the line sag value changes in a fairly large range.

It has also been found that changing the position of the two linear sensors may improve the performance of the sensor. This property can be used to design a perpendicular linear sensor for sag monitoring. For example, when the two probes are moved away from the center by 0.3 meters, Fig. 4-19, the total current vs. sag is shown in Fig. 4-20.

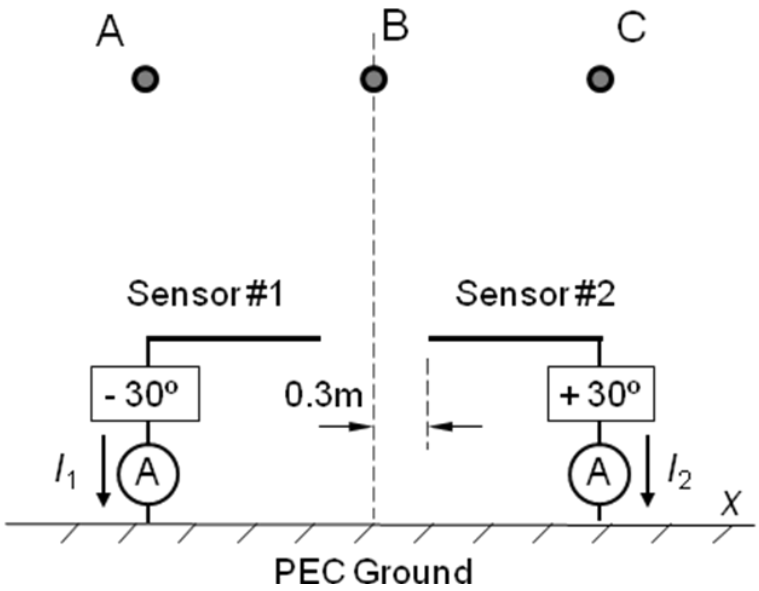

Fig. 4-19 Move the two probes away from the center by 0.3m

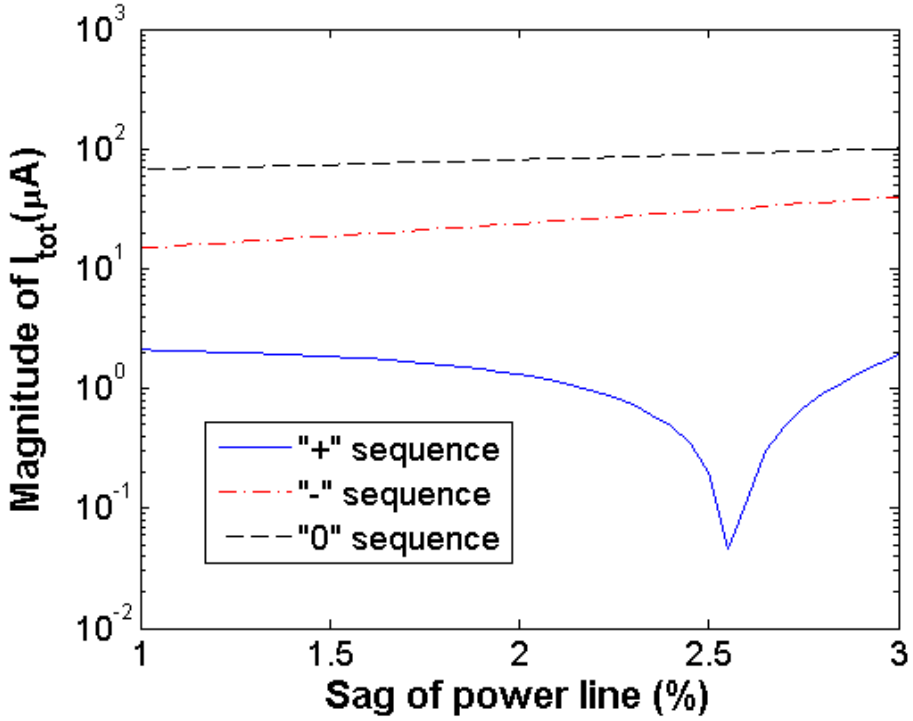

Fig. 4-20 Magnitude of total current when the probes are moved by 0.3 m (for positive mode)

At sag of 2.6% there is a null of the total induced current for the positive sequence mode. From 1% to about 2.6% of the line sag, the total current drops more than 40 times and shows a very good sensitivity to the change of line sag. Actually, this null also exists in Fig. 4-18 at about the sag value of 1%. By moving the two sensors apart from the center, the position of the null has been moved along the sag axis. This provide an extra degree of freedom for the sensor design. For example, if the sensor is designed as in Fig. 4-19, it can be used to monitor the line sag because for the positive sequence mode the current is very sensitive to the line sag near the value of 2.6%. If it is assumed that 2.6% represents a critical sag threshold and indicates dangerously low power line conductor height, the sensor in Fig. 4-19 can be used to indicate this dangerous condition.

Similarly, for the delta-configured power line such as defined in Model B, the

perpendicular linear sensor can also be used for sequence mode detection or sag monitoring. A system for negative/zero sequence voltage detection similar to that in Fig. 4-15 can be constructed, where the phase shifts are changed to +10 ° for I_1 and -10 ° for I_2. The induced currents for the positive, negative and zero modes are shown in Fig. 4-21.

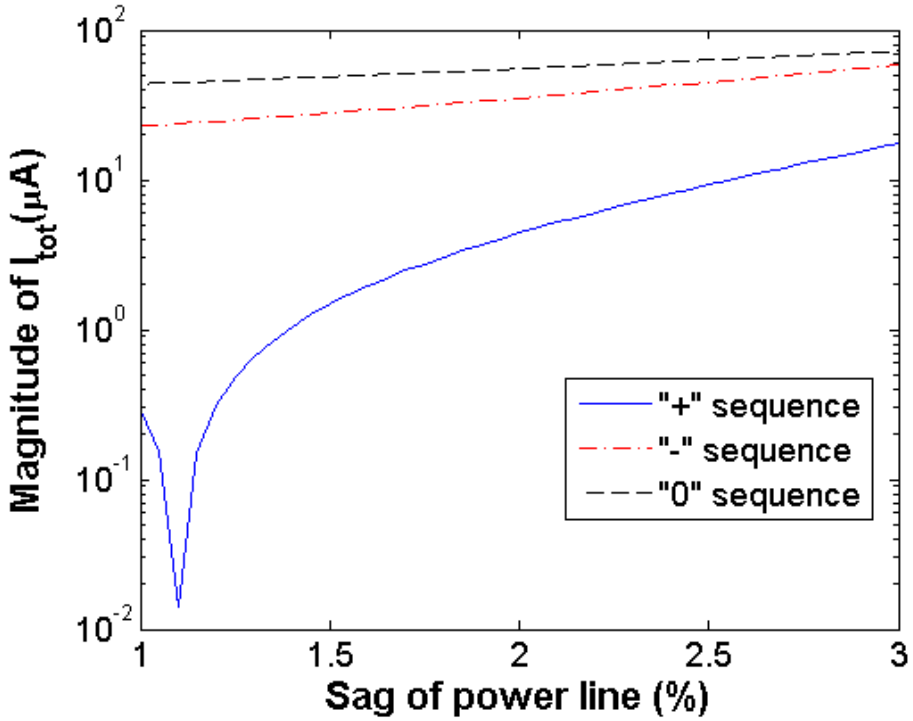

Fig. 4-21 Magnitude of total current for the positive, negative, and zero modes of voltage in Model B

It can be concluded that with appropriate parameters the perpendicular linear sensor can be used as a power line sag monitor and negative/zero sequence voltage detector. The mechanism of the perpendicular linear sensor is similar to that of point probe, which only responds to electric field coupling from the power line. But the perpendicular linear sensor has its own advantages, such as that either it can be designed to be robust to the change of the position of the power line conductor (the example given in Fig. 4-17) or very sensitive the line sag (the example in Fig. 4-19).

Additionally, since the perpendicular sensor has more complex structure than the point probe it provides more degrees of freedom for the design.

CHAPTER 5

PARALLEL LINEAR SENSORS

As discussed in Chapter 3, the linear sensor can be placed to be perpendicular, parallel, or oblique to the power transmission line. In Chapter 4, the theory and applications of the perpendicular linear sensor have been introduced. The study of this chapter will focus on the parallel linear sensor, which can be formed by placing a linear sensor along the direction in which the power transmission line is extending. The model of a typical parallel linear sensor is depicted in Fig. 5-1.

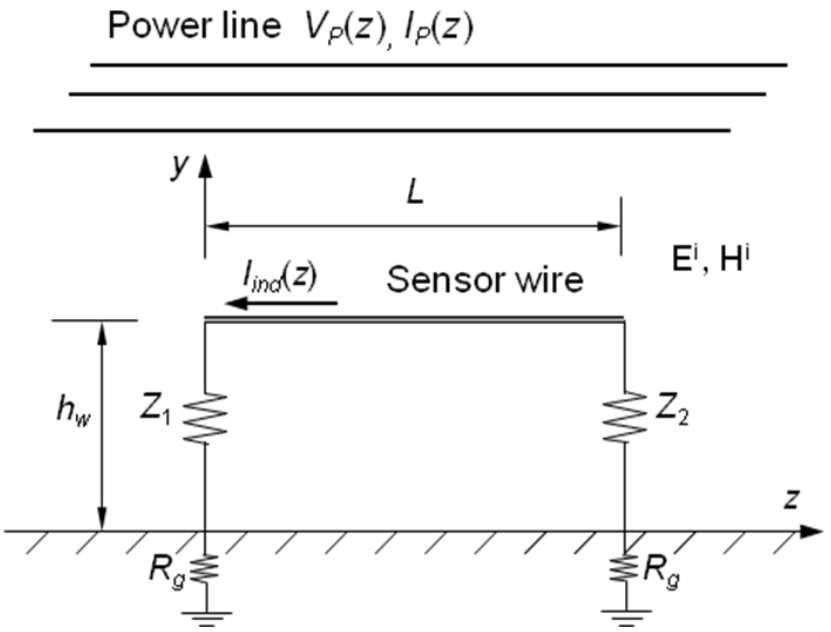

Fig. 5-1 Model of a horizontal parallel sensor

In the model, a horizontal linear sensor wire, L meters long and h_w meters above the ground, is connected to lumped impedances Z_1 and Z_2 and then to the ground at its two ends. Assume the grounding system at each end of the sensor results in an earth resistance of R_g. The sensor wire is along the z direction, the same direction as the energized three-phase power transmission line. $V_p(z)$ and $I_p(z)$ represent the set of

voltages and currents on the power line respectively. Under the excitation of the incident electromagnetic fields (i.e., E^i and H^i, produced by the power line), there is a current $I_{ind}(z)$ induced on the sensor wire.

The circuit loop formed by the sensor wire, the impedance Z_1 and Z_2, and the earth return cuts the flux of the incident magnetic field, i.e., H_x^i for this model. Therefore, different from the point probe and the perpendicular linear sensor, the parallel sensor receives the inductive (magnetic) coupling as well as the capacitive (electric) coupling from the incident fields. The induced current on the sensor can be decomposed into two components. One is related to the capacitive coupling, i.e. the voltage on the power line, and the other is related to the inductive coupling, i.e. the current on the power line. The differences in the nature of the capacitive and inductive coupling bring more complexities but more possibilities to the design of the parallel sensor. New functions other than those that can be realized using point probes or perpendicular sensors are possible. One good example is the directional coupler for detecting the traveling waves on the power line, which will be introduced in the following sections.

5.1 Directional coupler

A parallel linear sensor can be designed to operate as a directional coupler for power transmission lines (i.e., detecting forward and backward traveling wave amplitudes on the lines). The directional coupler is often used in microwave circuits and one definition of it is given as “a device that couples a secondary system only to a wave

traveling in a particular direction in a primary transmission system" [53]. By choosing the termination impedances correctly the effect of the forward or backward traveling wave can be cancelled, leaving the effect of only the other. For more specifically, the capacitive coupling and inductive coupling components of the current induced on the secondary wire due to the forward or backward wave can be made equal in magnitude and opposite in phase, i.e., can cancel at one end of the secondary wire [42].

On a real power transmission line, there almost always exist both forward and backward traveling waves because the terminations are not perfectly matched to the surge impedances. Fig. 5-2 (a) shows the propagation directions and polarities of the forward and backward traveling waves of voltage and current on a single-phase power line extending in z direction. If $+z$ is defined as the reference direction, the forward traveling waves propagate in $+z$ direction with a propagation term of $e^{-\gamma z}$, while the backward traveling waves in $-z$ direction with $e^{+\gamma z}$, where γ is the propagation constant on the power line. The voltage and current on the power line can be expressed in forms of the traveling wave components as [54], [46]

$$\begin{aligned} V_p(z) &= V_f e^{-\gamma z} + V_b e^{+\gamma z} \\ I_p(z) &= \frac{1}{Z_{si}}\left(V_f e^{-\gamma z} - V_b e^{+\gamma z}\right) \end{aligned} \tag{5.1}$$

where V_f and V_b are the phasor amplitudes of the forward and backward traveling waves of the power line voltage, respectively, and Z_{si} is the surge impedance of the power line. V_f and V_b are related by the reflection coefficient Γ_{TL} at the end of the power transmission line

$$\Gamma_{TL} = V_b / V_f = r_{TL} e^{j\theta_{TL}} \tag{5.2}$$

where Γ_{TL} is a complex number and r_{TL} and θ_{TL} are its magnitude and phase angle. The forward and backward traveling waves of the power line voltage have the same reference directions, while that of the current have the opposite reference directions. The total electromagnetic fields produced by the power line are the superposition of the fields due to the two sets of the traveling waves. For the electrically short power line (the length of the line is much smaller than a wavelength), the exponential terms in (5.1) can be ignored resulting in

$$\begin{aligned} V_p &= V_f + V_b \\ I_p &= \frac{1}{Z_{si}}\left(V_f - V_b\right) \end{aligned} \tag{5.3}$$

If a parallel linear sensor as depicted in Fig. 5-1 is introduced into the vicinity of the power line, both the forward and backward waves will contribute to the induced current in the sensor. And as discussed in Chapter 3, the induced current is composed of the capacitive and inductive coupling currents. Therefore, the induced current can be decomposed into four components based on the traveling wave direction and the type of coupling. The four components are denoted by I_e^f, I_e^b, I_m^f, and I_m^b, which are the capacitive coupling currents due to the forward and backward power line voltage waves, and the inductive coupling ones due to the forward and backward power line current waves respectively. The reference directions for each are shown in Fig. 5-2 (b).

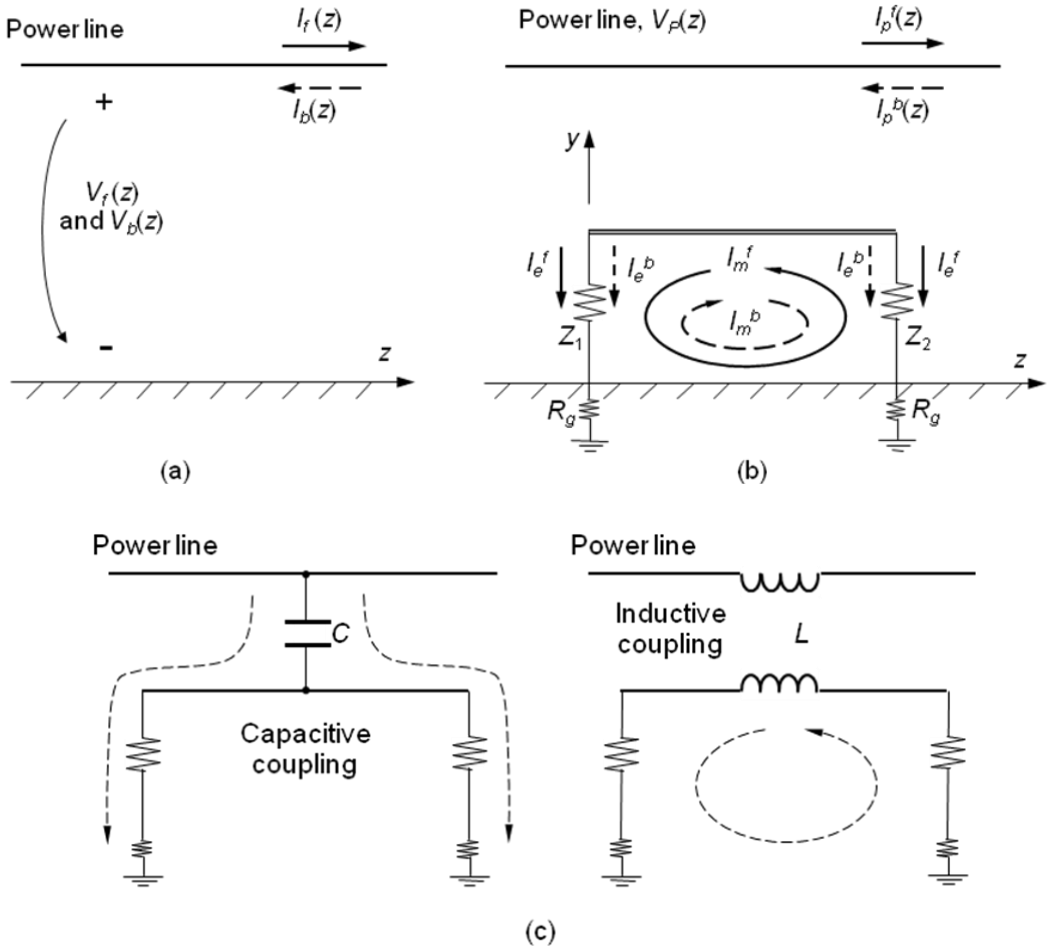

Fig. 5-2 (a) The reference directions of the forward and backward traveling waves of the voltage and current on a single-phase power line; (b) The reference directions of the capacitive and inductive coupling current in the parallel linear sensor due to the forward and backward traveling waves; (c) Circuit explanation for capacitive and inductive coupling between the sensor and the power line.

The capacitive current $I_e = I_e^f + I_e^b$ is determined by the incident electric field (E_y^i) and symmetrically distributed about the midpoint of the sensor wire. The inductive current $I_m = I_m^f + I_m^b$ is a loop current and its direction is determined in the manner that the direction (by the right hand rule) of the induced magnetic field is always against the change of the source magnetic field. According to this rule, the inductive current components, I_m^f and I_m^b, have opposite loop directions (CCW for I_m^f and CW for I_m^b in this case) because of the opposite reference directions of the forward and

backward traveling waves of power line current. The equivalent circuit explanation for the capacitive and inductive coupling, as shown in Fig. 5-2 (c), is helpful for understanding the direction of each component of the induced current.

Whether being induced by the forward or backward traveling waves on the power line, the capacitive and inductive currents have same signs at one end of the sensor wire and opposite signs at the other end. As shown in Fig. 5-2 (b), for the case of forward traveling waves, I_e^f has the same sign as I_m^f at the left end of the sensor (at Z_1), but has opposite sign at the right end (Z_2). Based on the analysis of Chapter 3, by carefully choosing Z_1 and Z_2 it can be realized that $I_e^f = -I_m^f$ at the right end of the sensor wire. In other words, the induced current due to the forward wave on the power line can be set to zero in the vertical branch on the right side of Fig. 5-2 (b). And the induced current measured in that branch is then only determined by the backward wave on the power line. Similarly, the induced current due to the backward wave can be set to zero in the left branch and that due to the forward waves is measured in there. This is basic mechanism for the parallel linear sensor to work as a directional coupler for the power line. The voltage at one end represents the forward wave amplitude while the voltage at the other end represents the backward wave amplitude.

The theory of the linear sensor has been introduced in Chapter 3. The induced current distribution on a parallel linear sensor can be determined by the reciprocity method and the result is shown in (3.18). But, here, it is more convenient to use the result in (3.38), which is identical to (3.18), because the capacitive and inductive components of the induced current are separated in (3.38) and it helps to obtain

insight into how the directional coupler works to detect the forward or backward traveling waves. Here, (3.38) is repeated and the equation number is changed to (5.4)

$$\begin{aligned}\bar{I}_{ind}(z) = &-\frac{A_1(z)}{Z_0 D}\int_0^z \left[B_1(z')\bar{V}_S'(z') + B_2(z')Z_0\bar{I}_S(z')\right]dz' \\ &-\frac{A_2(z)}{Z_0 D}\int_z^L \left[B_3(z')\bar{V}_S'(z') - B_4(z')Z_0\bar{I}_S(z')\right]dz'\end{aligned} \tag{5.4}$$

where L is the length of the sensor wire and

$$A_1(z) = Z_0\cosh\left[\gamma\left(L-z\right)\right] + Z_2\sinh\left[\gamma\left(L-z\right)\right]$$

$$A_2(z) = Z_0\cosh\left(\gamma z\right) + Z_1\sinh\left(\gamma z\right)$$

$$B_1(z') = Z_0\cosh\left(\gamma z'\right) + Z_1\sinh\left(\gamma z'\right)$$

$$B_2(z') = Z_1\cosh\left(\gamma z'\right) + Z_0\sinh\left(\gamma z'\right)$$

$$B_3(z') = Z_0\cosh\left[\gamma\left(L-z'\right)\right] + Z_2\sinh\left[\gamma\left(L-z'\right)\right]$$

$$B_4(z') = Z_2\cosh\left[\gamma\left(L-z'\right)\right] + Z_0\sinh\left[\gamma\left(L-z'\right)\right]$$

$$D = \left(Z_0Z_1 + Z_0Z_2\right)\cosh\left(\gamma L\right) + \left(Z_0^2 + Z_1Z_2\right)\sinh\left(\gamma L\right)$$

$$\bar{I}_S(z') = -j\omega c_w\int_0^{h_w} E_y^i(y', z')dy'$$

$$\bar{V}_S'(z') = -j\omega\mu_0\int_0^{h_w} H_x^i(y', z')dy' + E_z^i\left(y'=0, z'\right)$$

The induced per-unit-length voltage source is modified by adding the axial electric field on the air-earth interface to take care of the case of the lossy earth. In (5.4), the terms containing I_S are related to the capacitive coupling and that containing V_S are related to the inductive coupling. Then, (5.4) can be rewritten as

$$\bar{I}_{ind}(z) = I_e(z) + I_m(z) \tag{5.5}$$

where

$$I_e(z) = -\frac{A_1(z)}{Z_0 D}\int_0^z B_2(z')Z_0\bar{I}_S(z')dz' + \frac{A_2(z)}{Z_0 D}\int_z^L B_4(z')Z_0\bar{I}_S(z')dz' \tag{5.6}$$

$$I_m(z) = -\frac{A_1(z)}{Z_0 D}\int_0^z B_1(z')\bar{V}_S'(z')dz' - \frac{A_2(z)}{Z_0 D}\int_z^L B_3(z')\bar{V}_S'(z')dz' \tag{5.7}$$

The induced current at Z_1 (the left end of the sensor, $z = 0$), I_1, is found as

$$I_1 = I_{ind}(0) = I_{e1} + I_{m1} \tag{5.8}$$

where $I_{e1} = \frac{A_2(0)}{Z_0 D}\int_0^L B_4(z')Z_0\bar{I}_S(z')dz'$ and $I_{m1} = -\frac{A_2(0)}{Z_0 D}\int_0^L B_3(z')\bar{V}_S'(z')dz'$. And the induced current at Z_2 (the right end of the sensor, $z = L$), I_2, is

$$I_2 = I_{ind}(L) = I_{e2} + I_{m2} \tag{5.9}$$

where $I_{e2} = -\frac{A_1(L)}{Z_0 D}\int_0^L B_2(z')Z_0\bar{I}_S(z')dz'$ and $I_{m2} = -\frac{A_1(L)}{Z_0 D}\int_0^L B_1(z')\bar{V}_S(z')dz'$. It can be observed from (5.8) and (5.9) that the induced current at one end of the sensor is related only to the lumped impedance at the other end of the sensor, i.e., I_1 is only related to Z_2 and I_2 is only related to Z_1.

First, let $I_2 = 0$ in (5.9), resulting in $I_{e2} = -I_{m2}$, and Z_1 can be solved by

$$Z_1 = -Z_0\frac{\int_0^L\left[\cosh(\gamma z')\bar{V}_S'(z') + \sinh(\gamma z')Z_0\bar{I}_S(z')\right]dz'}{\int_0^L\left[\sinh(\gamma z')\bar{V}_S'(z') + \cosh(\gamma z')Z_0\bar{I}_S(z')\right]dz'} - R_g \tag{5.10}$$

Equation (5.10) gives the solution of Z_1 which leads to zero induced current at Z_2 ($I_2 = 0$). Similarly, the value of Z_2 causing zero induced current at Z_1 can be determined by letting $I_1 = 0$ and solving (5.8)

$$Z_2 = -Z_0\frac{\int_0^L\left\{\cosh\left[\gamma(L-z')\right]\bar{V}_S'(z') - \sinh\left[\gamma(L-z')\right]Z_0\bar{I}_S(z')\right\}dz'}{\int_0^L\left\{\sinh\left[\gamma(L-z')\right]\bar{V}_S'(z') - \cosh\left[\gamma(L-z')\right]Z_0\bar{I}_S(z')\right\}dz'} - R_g \tag{5.11}$$

Generally, for specified set of power line voltage and current, Z_1 and Z_2 are different, which means that single impedance value cannot cause zero induced current

at both sides of the sensor wire. In (5.10) and (5.11), the earth resistance of the grounding system is subtracted from the lumped impedance of Z_1 and Z_2. In the above derivation, the conditions of the traveling waves on the power line have not been mentioned. There could be pure forward or backward traveling waves, or some combination of them on the power line. The effects of the power line voltage and current are implicitly included in the induced per-unit-length sources I_S and V'_S. From the polarities shown in Fig. 5-2 (b), if pure forward traveling waves are assumed on the power line, I_2 is zero if Z_1 is determined by using (5.10). The result is rewritten as

$$Z_1^f = -Z_0 \frac{\int_0^L \left[\cosh(\gamma z')\bar{V}_S'^f(z') + \sinh(\gamma z') Z_0 \bar{I}_S^f(z')\right] dz'}{\int_0^L \left[\sinh(\gamma z')\bar{V}_S'^f(z') + \cosh(\gamma z') Z_0 \bar{I}_S^f(z')\right] dz'} - R_g \qquad (5.12)$$

where the notations of the per-unit-length sources $\bar{I}_S$ and $\bar{V}'$ have been changed to $\bar{I}_S^f$ and $\bar{V}_S'^f$ respectively to represent the case of pure forward waves on the power line. In the other hand, if assume pure backward traveling waves are assumed on the power line, I_1 can be set to zero when Z_2 is determined by using (5.11). The result is rewritten as

$$Z_2^b = -Z_0 \frac{\int_0^L \left\{\cosh\left[\gamma(L-z')\right]\bar{V}_S'^b(z') - \sinh\left[\gamma(L-z')\right] Z_0 \bar{I}_S^b(z')\right\} dz'}{\int_0^L \left\{\sinh\left[\gamma(L-z')\right]\bar{V}_S'^b(z') - \cosh\left[\gamma(L-z')\right] Z_0 \bar{I}_S^b(z')\right\} dz'} - R_g \qquad (5.13)$$

where $\bar{I}_S^b$ and $\bar{V}_S'^b$ are used to represent the case of pure backward waves on the power line.

Now, consider the case in which the power line voltage and current contain both the forward and backward traveling waves. Assume the values of Z_1 and Z_2 have been determined by using (5.12) and (5.13).

$$Z_1 = Z_1^f \text{ and } Z_2 = Z_2^b$$

The component of I_2 due to the forward traveling waves is zero because $Z_1 = Z_1^f$, resulting in $I_2 = I_2^b$. And $I_1 = I_1^f$ because the backward-traveling-wave component of I_1 has been set to zero by letting $Z_2 = Z_2^b$. Therefore, the induced currents at the ends on the left and right side of the sensor wire are coupled to the forward and backward traveling waves on the power line, respectively. This provides us a method to measure the traveling waves on the power line. Since the induced current is proportional to the incident fields, the reflection coefficient, defined in (5.2), of the power line can be found by

$$\Gamma_{TL} = I_2 / I_1 \tag{5.14}$$

In practice, the magnitude of Γ_{TL} can be obtained by measuring the magnitudes of I_1 and I_2, which can be easily achieved by using two ammeters. But measuring phase is more complicated.

5.2 Field experiments for directional coupler

5.2.1 Objective and model

To validate the theory of the directional coupler, two field experiments were conducted on May 4th and 25th, 2011. The experiments are based on the theory introduced in section 5.1 that zero induced current can be achieved at one end of the sensor wire by changing the impedance of Z_1 and Z_2 because of the cancellation of the capacitive and inductive components of the induced current. The settings of the two experiments are depicted in Fig. 5-3.

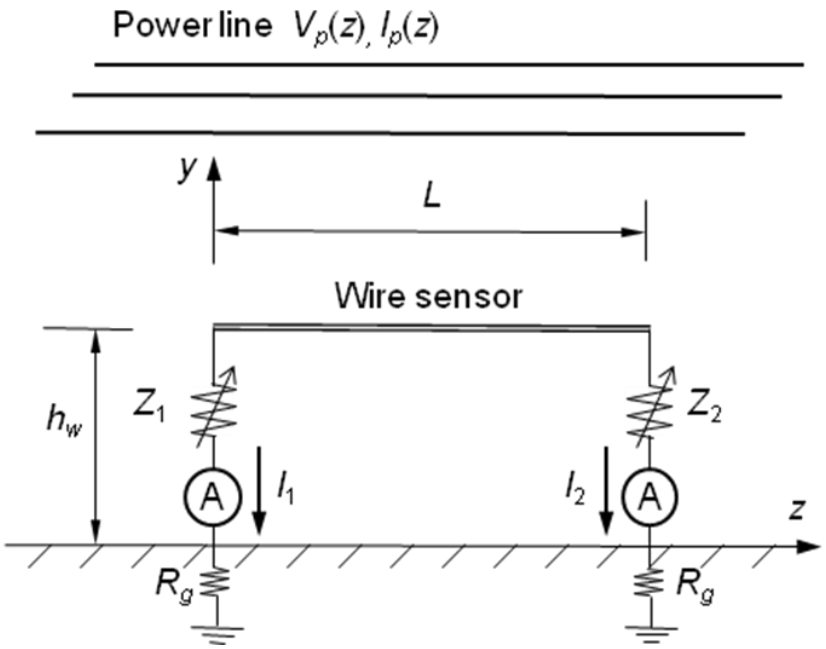

Fig. 5-3 Settings of the field experiment for directional couplers

In the experiments, the sensor wire is connected to ground through the adjustable impedance (Z_1 or Z_2), the ammeter, and the grounding copper rod(s) at each end of it. By adjusting the values of Z_1 and Z_2, the induced current I_1 or I_2 is expected to reach a null (close to zero) at some point. In the experiments, the case of inductive Z_1 and Z_2 has not been considered because of the fact found by simulations that the null can always be reached by capacitive Z_1 and Z_2 if the sensor is placed at the correct position (this will be discussed in more detail later). Therefore, during the field experiments, Z_1 and Z_2 are realized by adjustable resistance and capacitance boxes. The resistance and capacitance can be connected in series or parallel and their values can be chosen to realize the desired impedance values of Z_1 and Z_2. The circuits of both series and parallel connections are shown in Fig. 5-4.

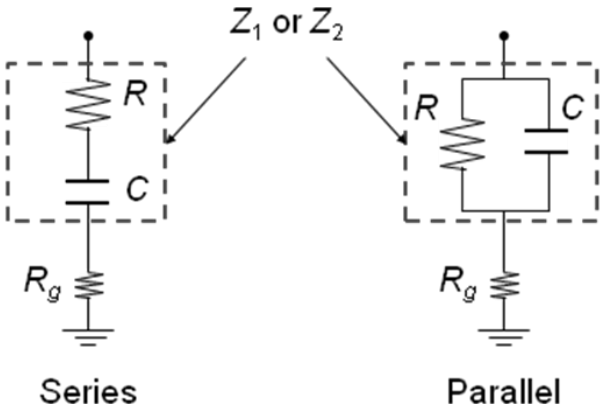

Fig. 5-4 Resistor and capacitor connected in series and parallel

For series connection, given the capacitive Z_1 or Z_2 calculated from (5.10) or (5.11), the values of the resistance and capacitance to be chosen are found by

$$\begin{aligned} R &= \mathrm{Re}(Z_1) - R_g \quad (\Omega) \\ C &= -\frac{10^6}{\omega\,\mathrm{Im}(Z_1)} \quad (\mu\mathrm{F}) \end{aligned} \tag{5.a12}$$

For parallel connection, they are found by solving the equation set

$$\begin{cases} \mathrm{Re}(Z_1) - R_g - \dfrac{R}{1+(\omega RC)^2} = 0 \\ \mathrm{Im}(Z_1) + \dfrac{\omega R^2 C}{1+(\omega RC)^2} = 0 \end{cases} \tag{5.a13}$$

where R is in Ω and C is in F. For the record, if Z_1 is inductive, the resistance and inductance in series connection can be found by

$$\begin{aligned} R &= \mathrm{Re}(Z_1) - R_g \quad (\Omega) \\ L &= \frac{\mathrm{Im}(Z_1)}{\omega} \quad (\mathrm{H}) \end{aligned} \tag{5.a14}$$

and for parallel connection they can be found by

$$\begin{aligned} R &= \mathrm{Re}(Z_1) - R_g + \frac{\left[\mathrm{Im}(Z_1)\right]^2}{\mathrm{Re}(Z_1) - R_g} \quad (\Omega) \\ L &= \frac{\left[\mathrm{Im}(Z_1)\right]^2 + \left[\mathrm{Re}(Z_1) - R_g\right]^2}{\omega \cdot \mathrm{Im}(Z_1)} \quad (\mathrm{H}) \end{aligned} \tag{5.a15}$$

Conducting the experiments is not as straight forward as deriving the theory. Since the separate traveling wave amplitudes on the power line to be tested are not known (equivalent to not knowing the reflection coefficient on the power line or the relative phase difference between the voltage and current on the power line), the values of Z_1 and Z_2, which can cause the null of the induced current, cannot be calculated beforehand. The only available information of the voltage and current on the power line is their magnitudes. This increases the unpredictability of the experiment and the difficulties in finding the null of the induced current. Details will be introduced in following sections.

5.2.2 Settings and preparations of experiment

The Benewah - Moscow 230kV power transmission line, owned by the Avista Utilities, was the power line tested. This line is single circuit with horizontal configuration. The experiment site is on land owned by John Salsbury and used with permission. The land is about three miles east to Moscow, ID and two miles north of the Moscow substation. It is on the intersection point of the Benewah - Moscow line with Robinson Park Rd. The experiment site was chosen to be at the midpoint of the north-south oriented span crossing the Robinson Park Rd. The span length is about 150m and the ground under that span is very flat, which is ideal for conducting the experiments. In Fig. 5-5, photographs of the experiment settings taken from the experiment site are shown.

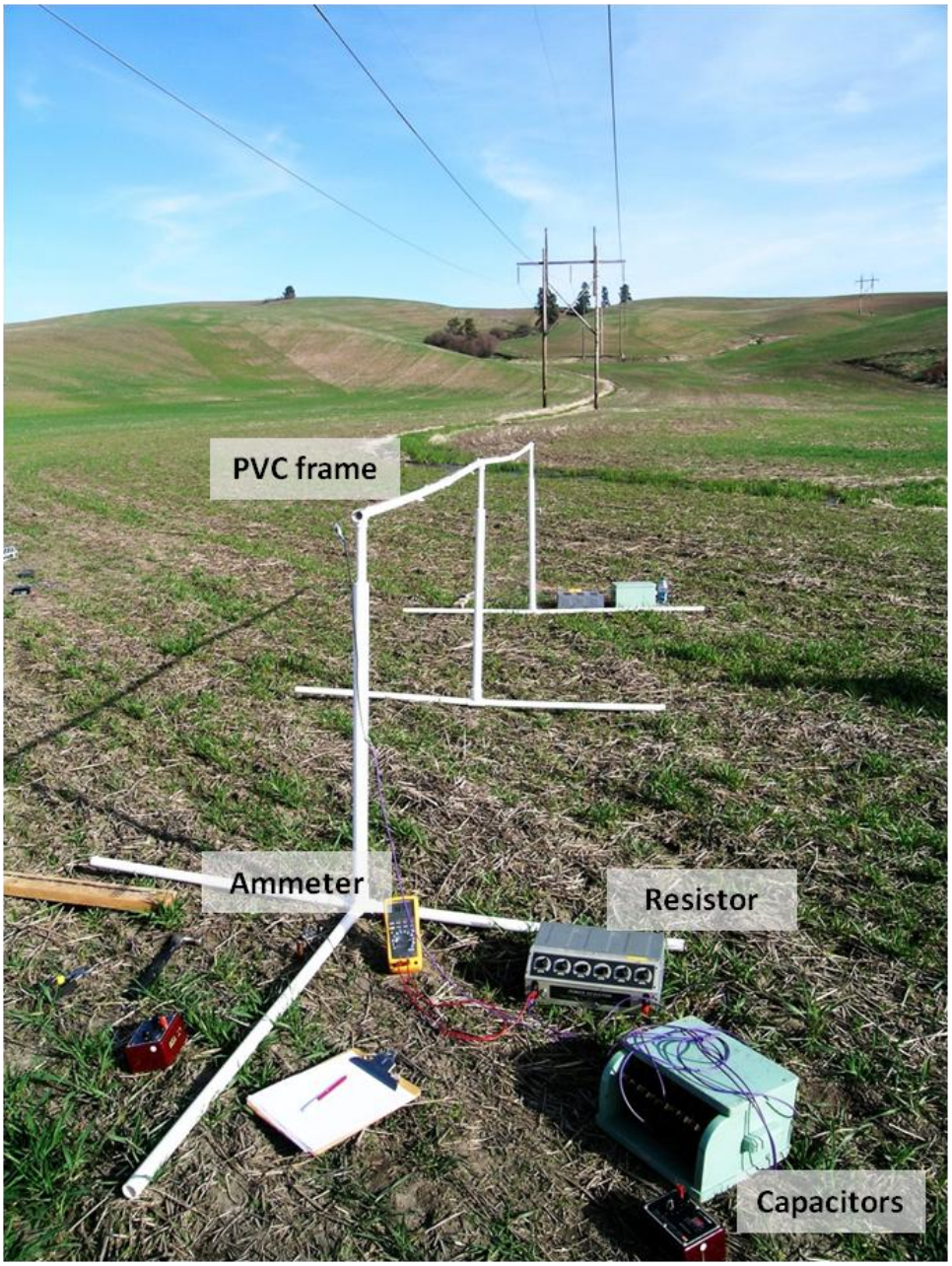

(a) on May 4th, 2011

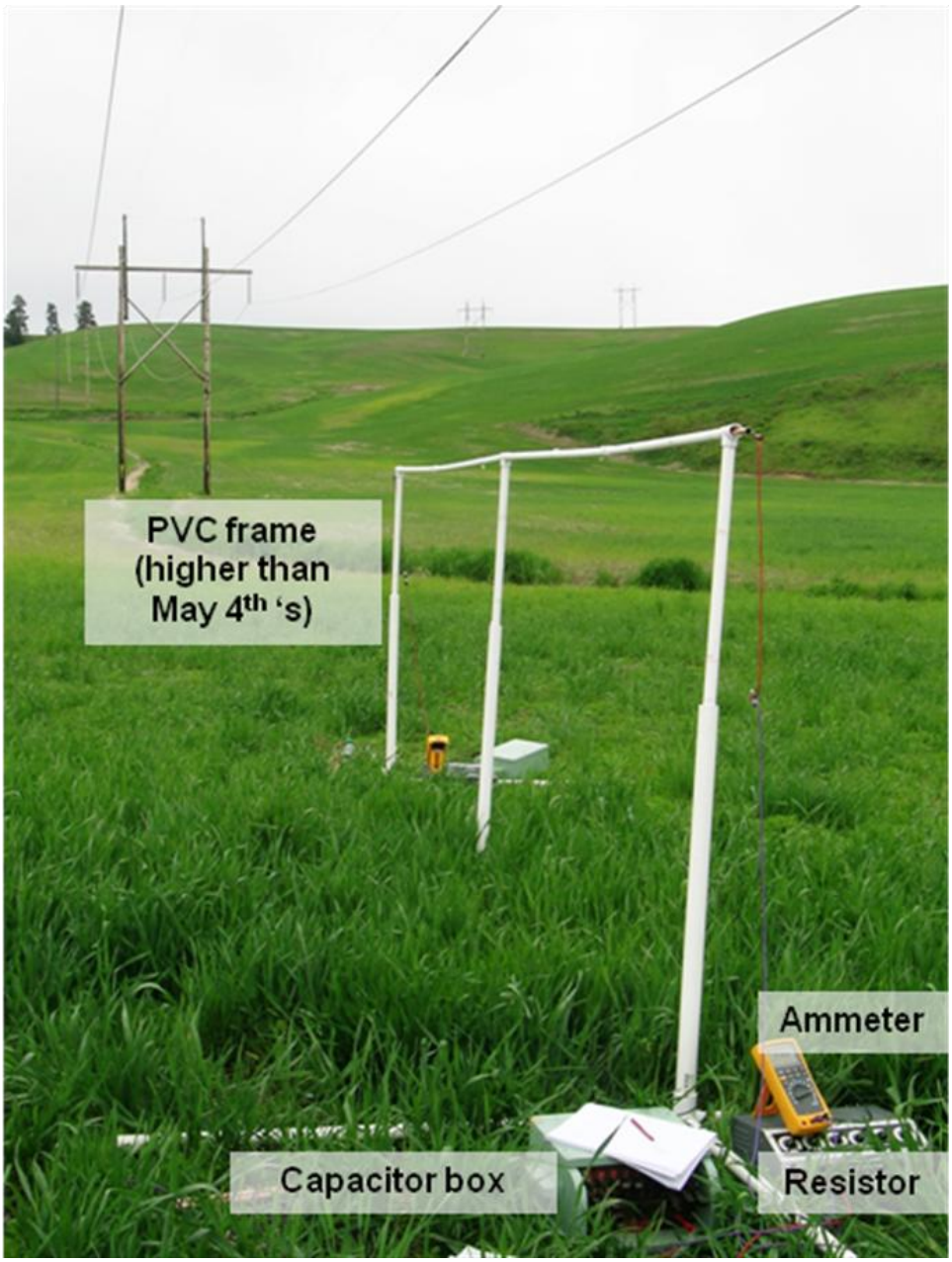

(b) on May 25th, 2011

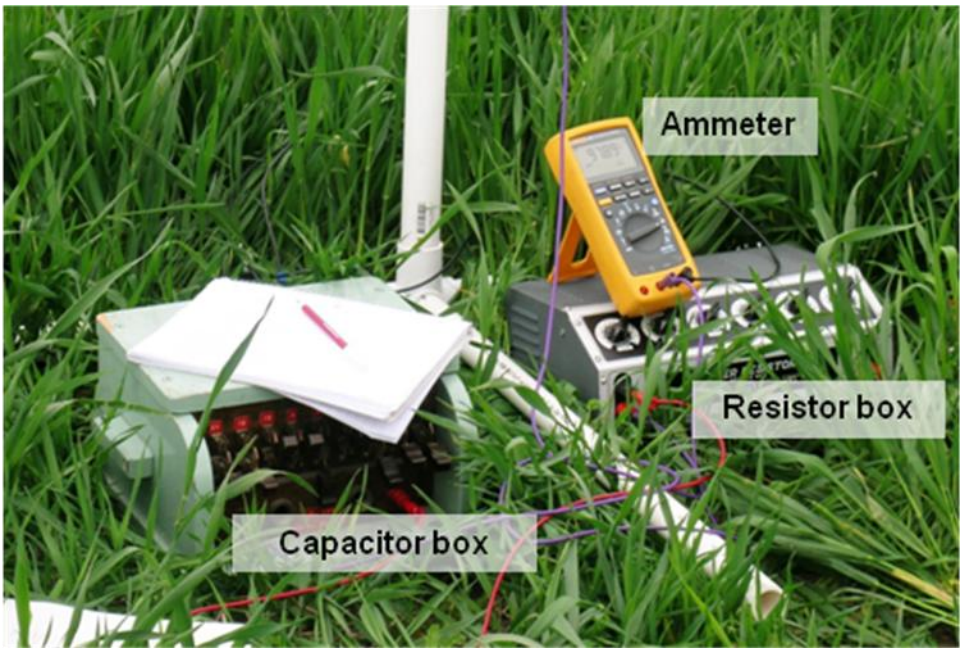

(c) closer look of the resistor box, capacitor box, and ammeter

Fig. 5-5 Experiment site and settings of the experiments for directional couplers.

On May 4th, when conducting the experiment, the voltage of the power line was 242kV and the average phase current was 221A. The parameters of the line configuration are not known, but they can be estimated by some indirect methods such as measuring the electric field produced by the line to estimate the height and spacing of the line conductors. For this reason, the electric field in the vertical direction (E_y) was first measured at a height of one meter above the ground and the height and spacing of the line conductors was estimated by matching the measured data of E_y with the theoretical calculation. The comparison of results of measured and calculated E_y are shown in Fig. 5-6. After multiple calculation attempts, the conductor height at mid-span of 10.4m (34ft) and spacing of 6m was found to give the best match with the measured data. Thus, these two values will be used as the parameters of the power line.

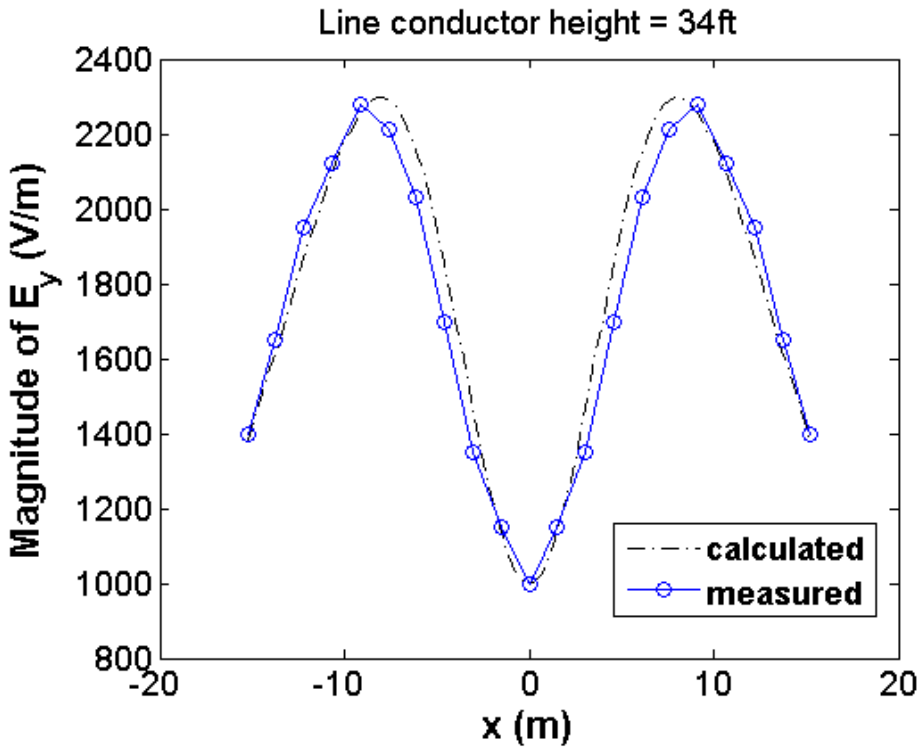

Fig. 5-6 Measurements of E_y compared to the calculated values to estimate the height and spacing of the line conductor, the conductor height of 10.4m (34ft) and spacing of 6m give the best match with the measured data.

In summary, the information about the transmission line under test on May 4th and May 25th is listed in Table 5-1, and will be used in all the simulations for this chapter.

Table 5-1 Information of the tested power transmission line

	May 4th	May 25th
Line-to-line voltage (kV)	242	242
Phase current, three phases (A)	unknown	218, 237, 225
Average phase current (A)	221	225
Mid-span conductor height (m)	10.4 (estimated)	Same as left
Phase spacing (m)	6 (estimated)	Same as left
Diameter of the conductor (cm)	3.5 (typical value)	Same as left

In the first experiment (on May 4th, see Fig. 5-5), the sensor of the directional

coupler was made of copper wires with a diameter of 4.4mm, attached on the top bar of the supporting frame made by PVC pipes. At each of its ends the sensor is connected to the adjustable impedance, the ammeter, and then to the grounding system. The grounding system is formed by single or multiple copper pipes vertically driven into the ground. If multiple rods are used, they were aligned in a line perpendicular to the power line, equally spaced, and connected together. In the second experiment (on May 25th), the sensor was changed to a copper pipe of 1.6cm in diameter (same kind of copper pipes as used for grounding rods) and placed at larger height above the ground in order to increase the capacitive induced current. In Fig. 5-7, the photo of the copper wire and pipes used for the sensors and grounding rods is provided.

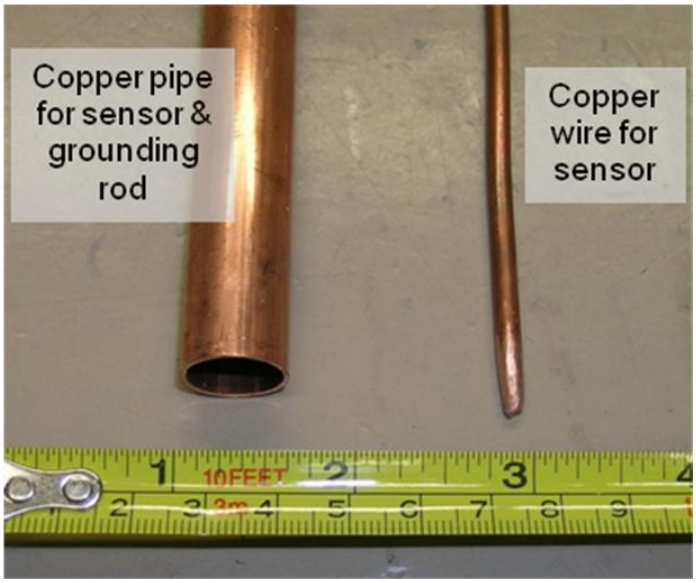

Fig. 5-7 Copper wire (May 4th) and pipes (May 25th) used for sensor and grounding rods

The detailed geometries of the sensor and grounding system are shown in Table 5-2.

Table 5-2 Geometries of the sensor and grounding system

		May 4th	May 25th
Sensor of directional coupler	Diameter (mm)	4.4	16
	Length (m)	4.88 (4ft ×4)	4.57 (2.5ft×6)
	Height (m)	1.2	1.6
Copper rod for grounding system	Diameter (mm)	16	16
	Length of each rod (m)	0.67	0.67
	Depth into earth (m)	0.61	0.61
	Spacing between rods (m)	0.61	0.61

The earth resistance R_g of the grounding system is important for the experiment because it affects the value of the total impedance connected in the circuit. If R_g is too large, by (5.10) and (5.11), Z_1 and Z_2 may be required to have negative real parts, which is physically impossible and means that there is no chance to find the null in the induced current. Therefore, it is necessary to have an estimation of R_g first. During the field experiments, R_g was measured by the Fall of Potential method (also known as the 62% method or Three-pole method) [55], [56], as shown in Fig. 5-8 (a). To measure the earth resistance of the primary grounding rod R (or the grounding system with multiple rods), another two small rods, P and C, are introduced and driven into the ground far enough away from rod R. A DC source was applied between R and C and the I_g (see Fig. 5-8) and the voltage V_g (between R and P) were measured. When the distance D_1 between R and P is 62% of the distance L_1 between R and C, the earth resistance R_g of the primary rod R can be obtained as

$$R_g = V_g / I_g \tag{5.15}$$

A photo of one test using this method to measure the earth resistance is shown in Fig. 5-8 (b). The testing site is on the lawn east to the ETRL building on campus of WSU, Pullman, WA.

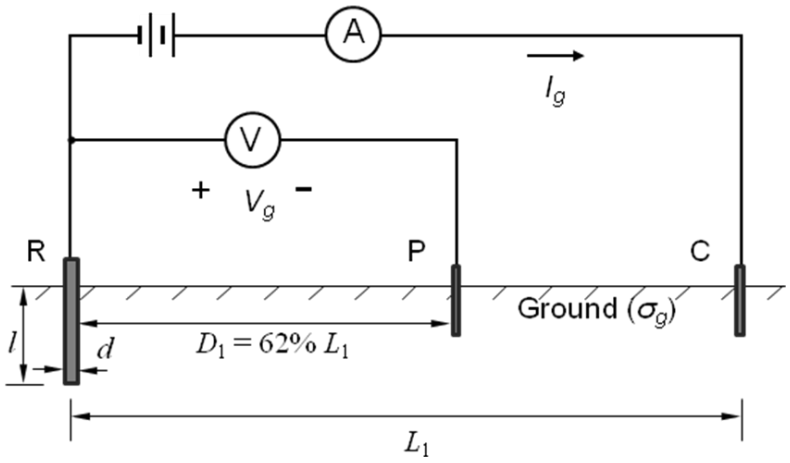

(a) Diagram of measurement settings

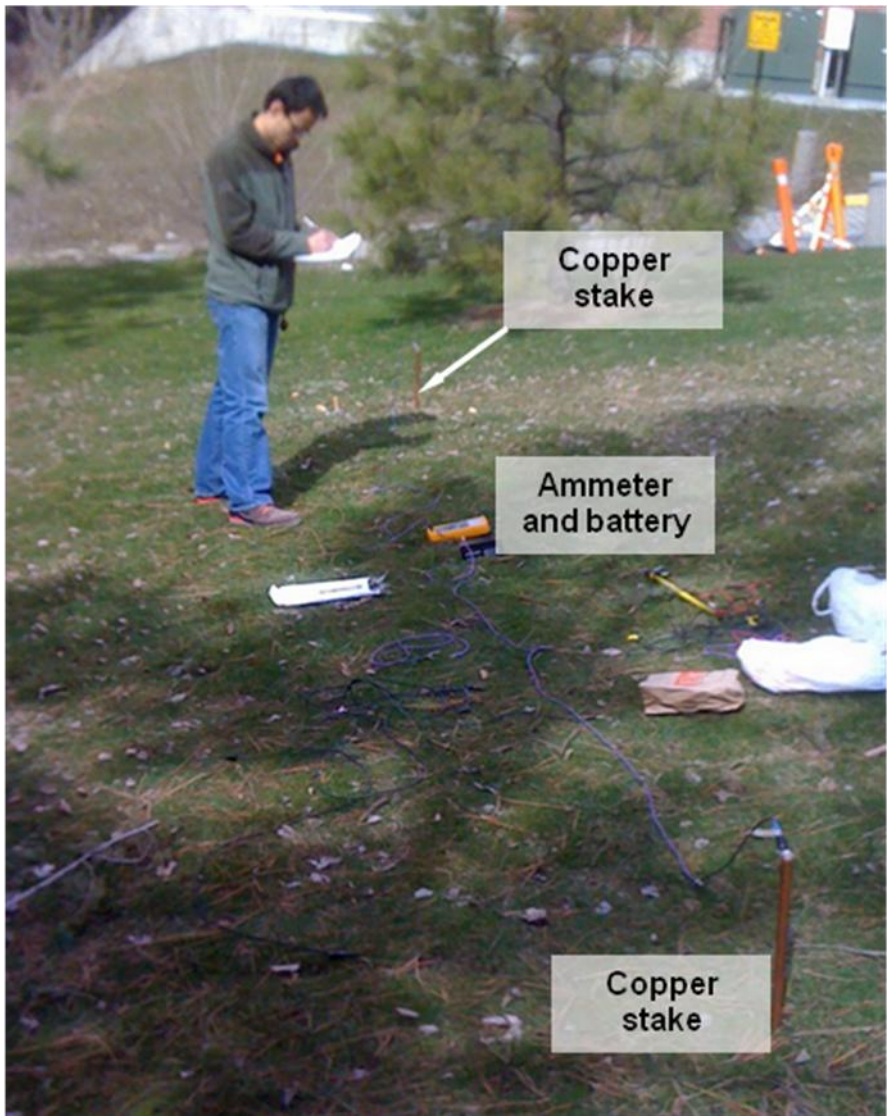

(b) Photo of the testing site

Fig. 5-8 Fall of Potential method to measure the earth resistance of the grounding rod(s). (a) diagram of the method, (b) photo of the settings taken from the testing site.

The results of the R_g measurements are shown in Table 5-3.

Table 5-3 Measurements of earth resistance R_g of the grounding system

	R_g (Ω) on May 4th	R_g (Ω) on May 25th
Single rod	78	75
Two rods	48	---
Three rods	34	---

To successfully conduct this experiment, the reflection coefficient Γ_{TL}, defined in (5.2), should be known in order to divide the current/voltage into forward and backward waves. By using (5.2), (5.3) can be rewritten as

$$\begin{aligned} V_p &= V_f\left(1+\Gamma_{TL}\right) \\ I_p &= \frac{V_f}{Z_{si}}\left(1-\Gamma_{TL}\right) \end{aligned} \tag{5.16}$$

where V_p, I_p, and V_f are all phasors (complex numbers). It is necessary to know both the magnitude and phase angle of V_p and I_p to uniquely determine Γ_{TL}. However, in practice, only the magnitudes of V_p and I_p are available. As a result, Γ_{TL} cannot be uniquely determined. Without adequate knowledge of Γ_{TL}, it is difficult to get a unique prediction of the behavior of the induced current in the sensor because the value of Γ_{TL} affects the incident fields on the sensor, and consequently induced current. Thus, for preparing the experiments, it is important to have good estimates of Γ_{TL}.

It is assumed that the load on the power line is nearly resistive because reactive power is minimized. This means that the phase angle θ_{TL} of Γ_{TL} should not be very large. Taking the magnitude squared of both sides of the two equations in (5.16) and dividing the first equation by the second one results in

$$\left|V_p\right|^2\left|1-\Gamma_{TL}\right|^2 = \left|I_p Z_{si}\right|^2\left|1+\Gamma_{TL}\right|^2$$

After using $\Gamma_{TL} = r_{TL}e^{j\theta_{TL}} = r_{TL}\left(\cos\theta_{TL} + j\sin\theta_{TL}\right)$ and some simplifications, the above equation can be rewritten as

$$\cos\theta_{TL} = \frac{\left(a-b\right)\left(1+r_{TL}^2\right)}{2r_{TL}\left(a+b\right)} \tag{5.17}$$

where $a = |V_p|^2$ and $b = |I_p Z_{si}|^2$. Equation (5.17) shows the relation between the

magnitude and phase angle of the reflection coefficient for specified power line voltage and current. Given r_{TL}, θ_{TL} can be calculated and vice versa. Fig. 5-9 shows some calculations of r_{TL} and phase angle θ_{TL} for different values of $|I_p|$. Each curve in the figure is for a current $|I_p|$ between 150 to 230A (with a 5A step between two adjacent curves). $|V_p|$ = 242kV was assumed for all calculations.

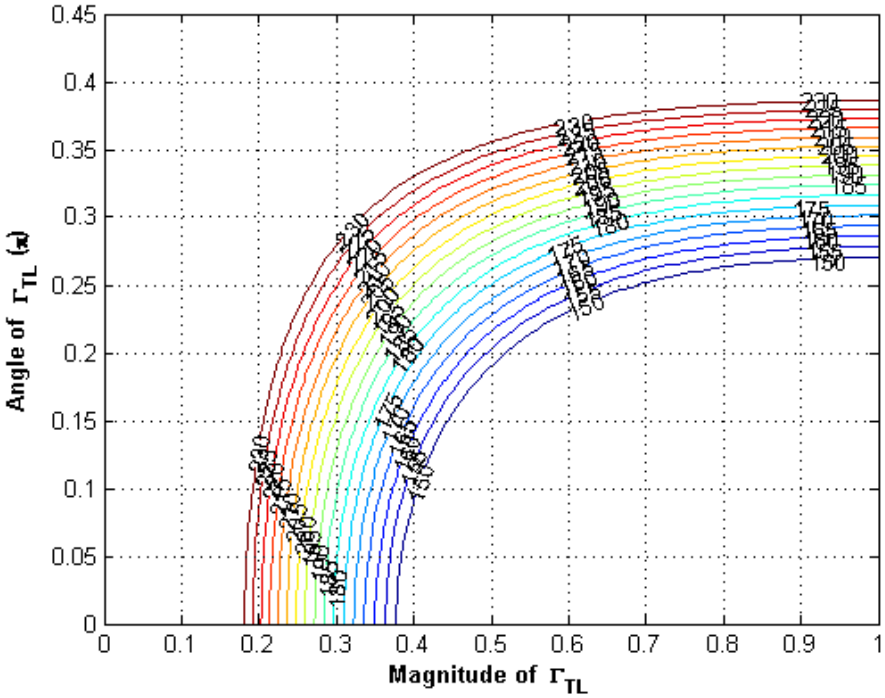

Fig. 5-9 Calculations of magnitude and angle of Γ_{TL} given the line current between 150 and 230A, the unit of phase angle is π.

The beginning part (when r_{TL} is small) of each curve is almost vertical, which means that a large change in θ_{TL} produces only a tiny change in r_{TL}. This will also be evident in the table below. The average power line currents for the first and second experiment are 221A and 225A respectively, for which some values of r_{TL} are chosen and the corresponding values of θ_{TL} are calculated by (5.17) and listed in Table 5-4. These values will be used as the predictions of the actual Γ_{TL} in the simulations for the experiment.

Table 5-4 Some calculated Γ_{TL} for I_p = 221A and 225A

I_p = 221A	r_{TL}	0.21	0.22	0.24	0.26	0.28	0.30	0.40	0.50	0.60	0.80
	θ_{TL} (π)	0.080	0.121	0.172	0.205	0.230	0.250	0.309	0.338	0.354	0.369
I_p = 225A	r_{TL}	0.20	0.22	0.24	0.26	0.28	0.30	0.40	0.50	0.60	0.80
	θ_{TL} (π)	0.074	0.150	0.191	0.221	0.244	0.262	0.317	0.345	0.361	0.375

As mentioned before, the power line at the experiment site is in the north-south direction and the current flows from north to south. During the experiments, the sensor was placed at three positions, which are under the conductor of each of the three phases respectively. If facing north is chosen to be the reference direction, the coordinates on *x*-axis of these three positions are $x = -6$ (west side), $x = 0$ (middle), and $x = +6$ (east side, all units in meters), as shown in cross sectional view in Fig. 5-10. The phase sequence of the three phases is assumed as shown in the figure.

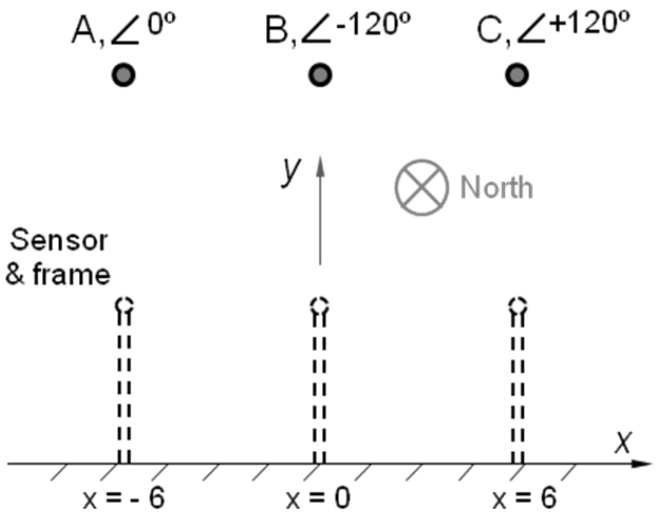

Fig. 5-10 Three positions to place the sensor

The profiles of the incident fields at the three positions are different, causing the differences between the measurements of the induced current.

With all the above preparations completed, the experiments were conducted with

the procedures given below:

1) Run the simulation based on the parameters and predictions previously obtained, calculate the value of Z_1 or Z_2 that could possibly cause the null in any of the induced currents, and use this value as a reference.

2) Using only a identical resistance box at each end of the sensor, the values of the two resistances were kept the same ($Z_1 = Z_2 = R$) and increased step by step. Magnitudes of I_1 and I_2 are recorded for each step.

3) Add the capacitance box(es) in seires, adjust the values of the resistors and capacitors to check whether there is an obvious null in I_1 or I_2. Take the measurement of I_1 and I_2 and record the data.

4) Change the sensor's position (as shown in Fig. 5-10) and redo the processes from 1) to 3).

5.2.3 Results and analysis

All the three positions of the sensor (see Fig. 5-10) were tried on May 4th and only the two positions under the side phase conductors ($x = -6$ and $x = +6$) were tested on May 25th. I_1 is the induced current measured at the south end of the sensor and I_2 is for the north end. First, simulations are conducted for the experiments based on the parameters previously determined. The values of Z_1 (assumed $Z_2 = Z_1$) causing the null in induced current and the resistances and capacitances that can realize these values of Z_1 in series or parallel connections are listed in Table 5-5, where R_s, C_s, R_p, and C_p are the resistance and capacitance for the series and parallel connections,

respectively.

Table 5-5 Simulation results for the value of Z_1 which causes the null in induced current and the resistances and capacitances to realize it in series or parallel connections ($R_g = 80\Omega$)

Date	Γ_{TL}	Sensor position x (m)	Z_1 (Ω, $Z_1 = Z_2$)	R_s (Ω)	C_s (μF)	R_p (Ω)	C_p (μF)
May 4th	$0.28e^{j0.230\pi}$	-6 (west)	767-503j	687	5.27	1056	1.84
		0 (middle)	716-288j	636	9.22	766	1.57
		6 (east)	902-167j	822	15.87	856	0.63
May 25th	$0.28e^{j0.244\pi}$	-6 (west)	523-352j	443	7.54	722	2.92
		6 (east)	617-128j	537	20.65	568	1.11

Fig. 5-11 to 5-13 show the comparisons between the data measured on May 4th and simulation results for the cases that only the resistors are used at the three sensor positions, respectively. The reflection coefficient Γ_{TL} is assumed to be $0.28e^{j0.230\pi}$ (from Table 5-4) for these simulations because the agreement with the data was best.

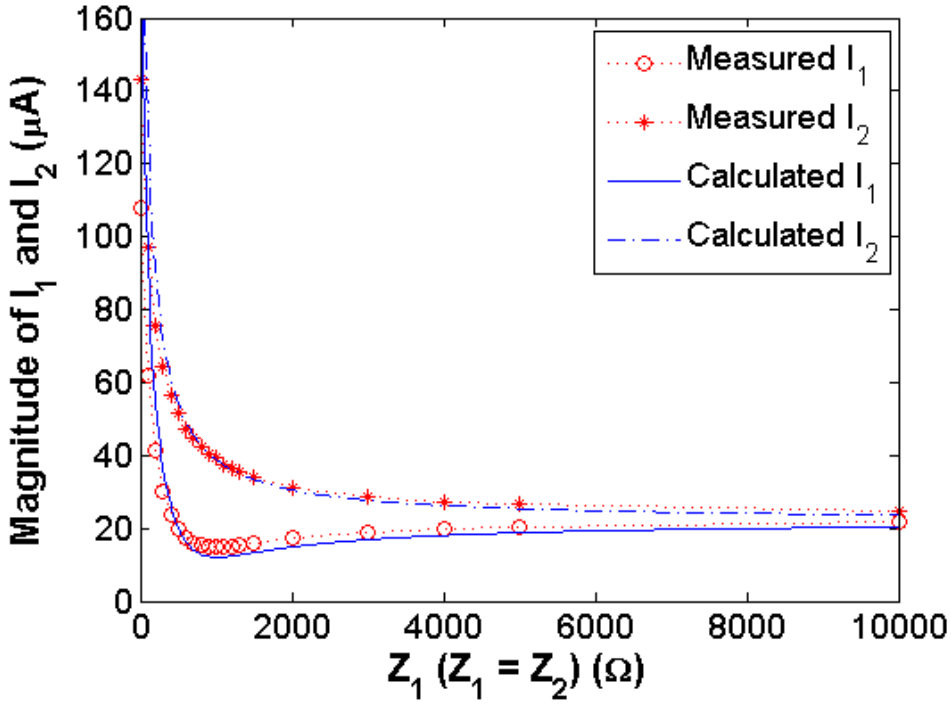

Fig. 5-11 Measured data (on May 4th) for I_1 and I_2 compared with simulations results when only resistance boxes were used, the sensor is under the phase conductor on the west side ($x = -6$m), $\Gamma_{TL} = 0.28e^{j0.230\pi}$.

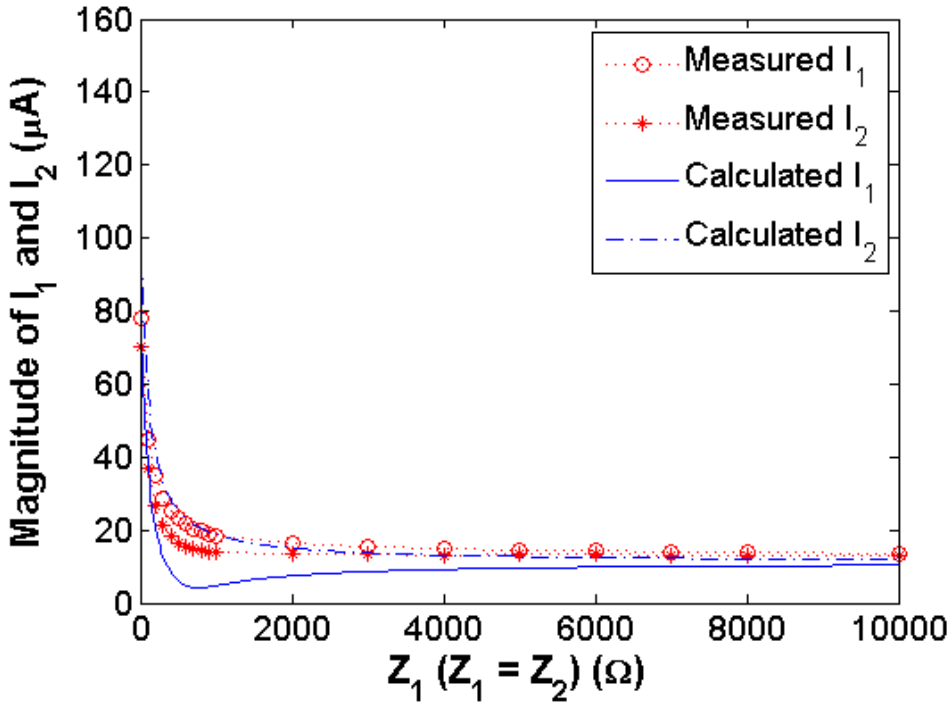

Fig. 5-12 Measured data (on May 4th) for I_1 and I_2 compared with simulations results when only resistance boxes were used, the sensor is under the conductor of the center phase ($x = 0$), $\Gamma_{TL} = 0.28e^{j0.230\pi}$.

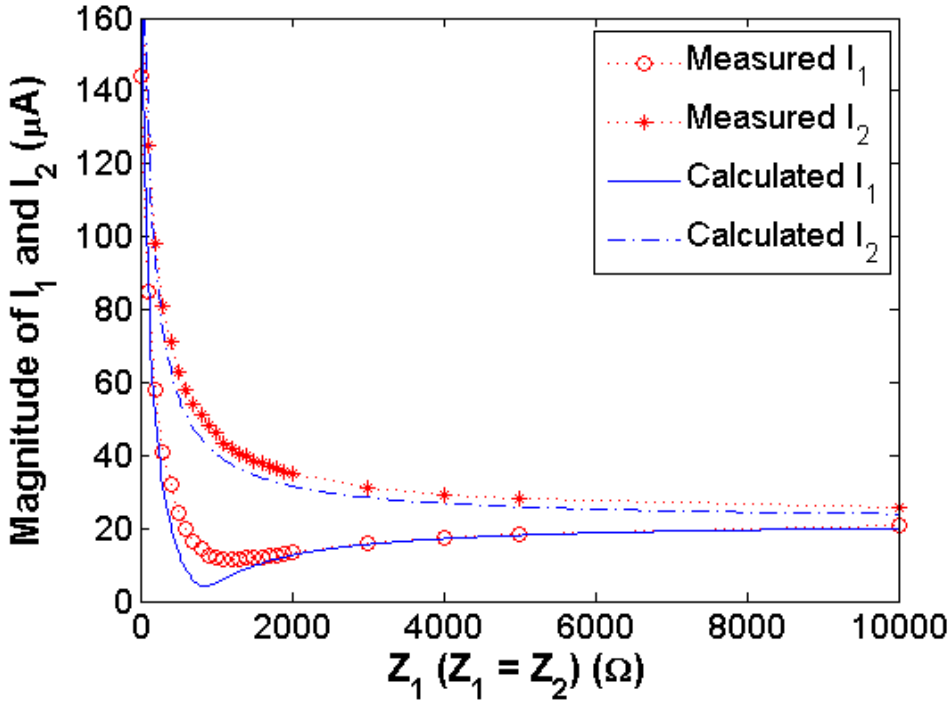

Fig. 5-13 Measured data (on May 4th) for I_1 and I_2 compared with simulations results when only resistance boxes were used, the sensor is under the phase conductor on the east side (x = + 6m), $\Gamma_{TL} = 0.28e^{j0.230\pi}$.

From the figures, it can be observed that the measurements match better in Fig. 11 and Fig. 13 than Fig. 12. In Fig. 11 and Fig. 13, measured data have the same trends as the simulations, except that the calculated I_1 has a deeper minimum than the measured data in Fig. 13. Although the data agreement levels are different in the three figures, no evidence shows that this difference is caused by any known reason. It might be due to the inaccuracy of the parameters such as Γ_{TL}, and coincidently the data have better agreement at one place than the other.

What is consistent in the three figures is that, for both the measured and simulated data, the magnitudes of I_1 and I_2 become closer and closer with increasing resistance. As previously introduced, the induced current is composed of the capacitive and

inductive components. The capacitive component is due to the capacitive (high impedance) coupling, independent of the resistance connected at the sensor's end, and is symmetrical, about the midpoint of the sensor. On the other hand, the inductive component is a loop current and dependent of the impedance in the circuit loop of the sensor. Thus increasing of resistance suppresses the magnitude of the inductive component and ultimately it can be ignored. Therefore, when the resistance is large enough, what remains in the induced current is only the capacitive component and it has same magnitude at the two ends of the sensor wire, i.e., I_1 equals I_2 then. The measurements have proved this point in the three tests, providing the validation for part (the capacitive coupling part) of the theory of the directional coupler.

Another useful result from the measurement is that one of I_1 and I_2 is always larger than the other and it is consistent with the direction of the power line current, which implies that, if the phase sequence is known, by comparing the magnitude of I_1 and I_2 the direction of the power line current can be determined.

The results of the experiment on May 25th are similar to those for May 4th except that magnitude level of the induced currents is higher because the copper pipe (with larger diameter and placed at higher position) was used as the sensor and this enhances the capacitive coupling. Fig. 14 shows the results on May 25th for the sensor being under the phase conductor on the west side. The valley shape of I_1 is more obvious since the capacitive coupling was intentionally enhanced.

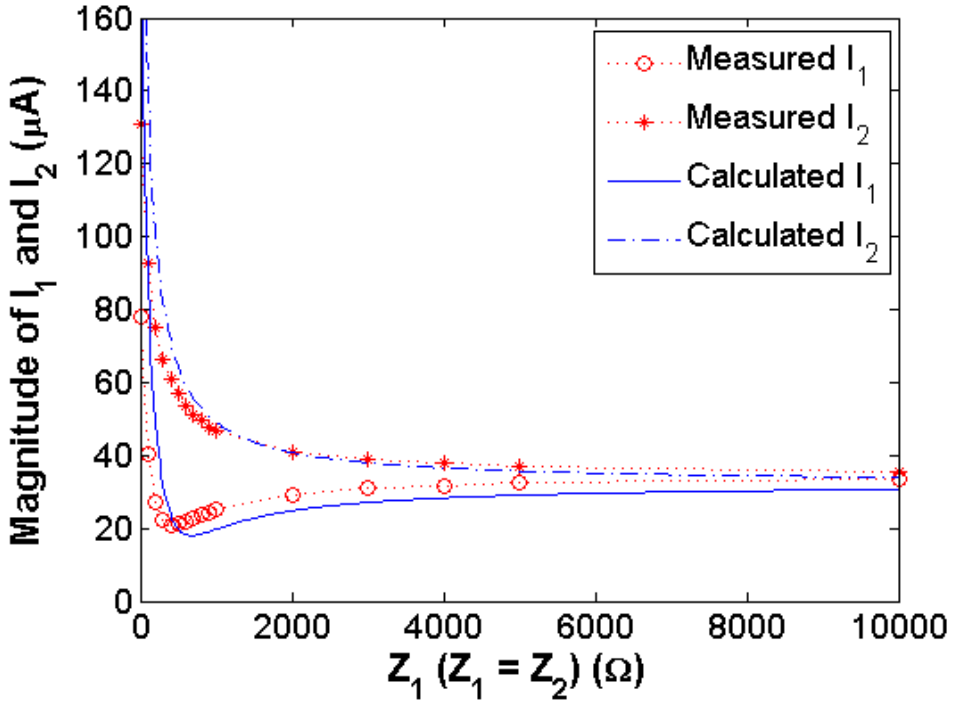

Fig. 5-14 Measured data (on May 25th) for I_1 and I_2 compared with simulations results when only resistance boxes were used, the sensor is under the phase conductor on the west side ($x = -6$m), $\Gamma_{TL} = 0.28e^{j0.244\pi}$.

The next step in the experiment was to add a series or parallel capacitor in an attempt to find the actual null of the induced current. The null of the induced current is expected to be observed by adjusting the resistor and capacitor until the proper values are found. To guide the process, equal magnitude contours (in μA) of the induced current are first drawn on a grid with capacitance (C) and resistance (R) as the x and y axis respectively. The figures, as shown in Fig. 5-15 (a) and (b), are like the maps of the induced current in the C-R coordinates. In the two 'maps' of Fig. 5-15, the induced current gets smaller when closer to the intersection of the vertical and horizontal dashed lines, and reaches the null at the intersection. The C-R coordinates of the two points in the series and parallel cases are (7.54, 443) and (2.92, 722) respectively, which are the theoretical values of the resistance and capacitance which

cause the null, as shown in Table 5-5, for $\Gamma_{TL} = 0.28e^{j0.244\pi}$.

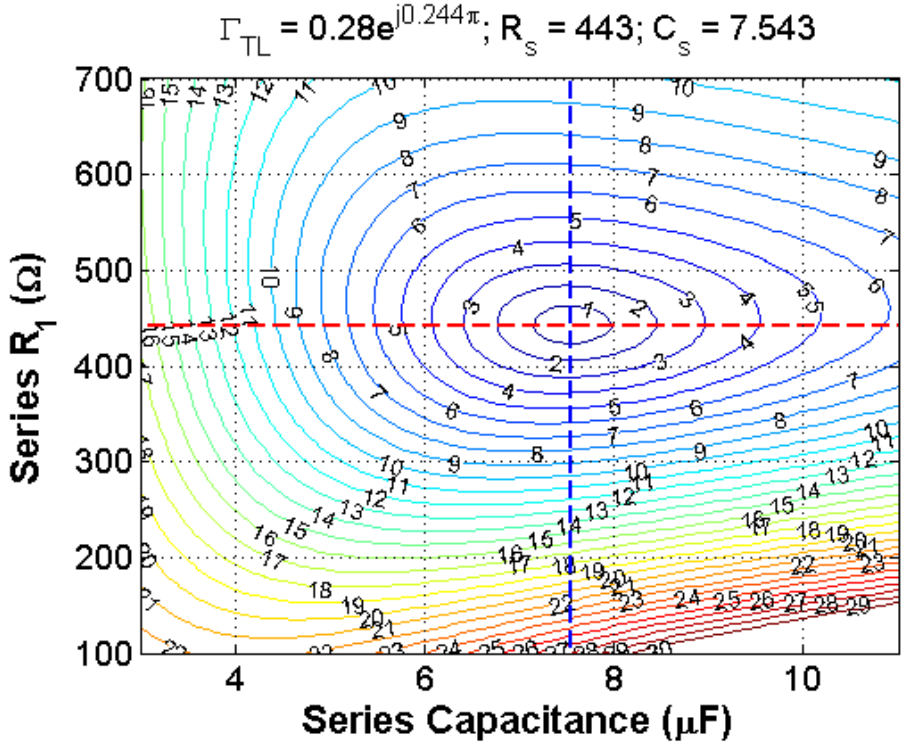

(a) resistance and capacitance connected in series

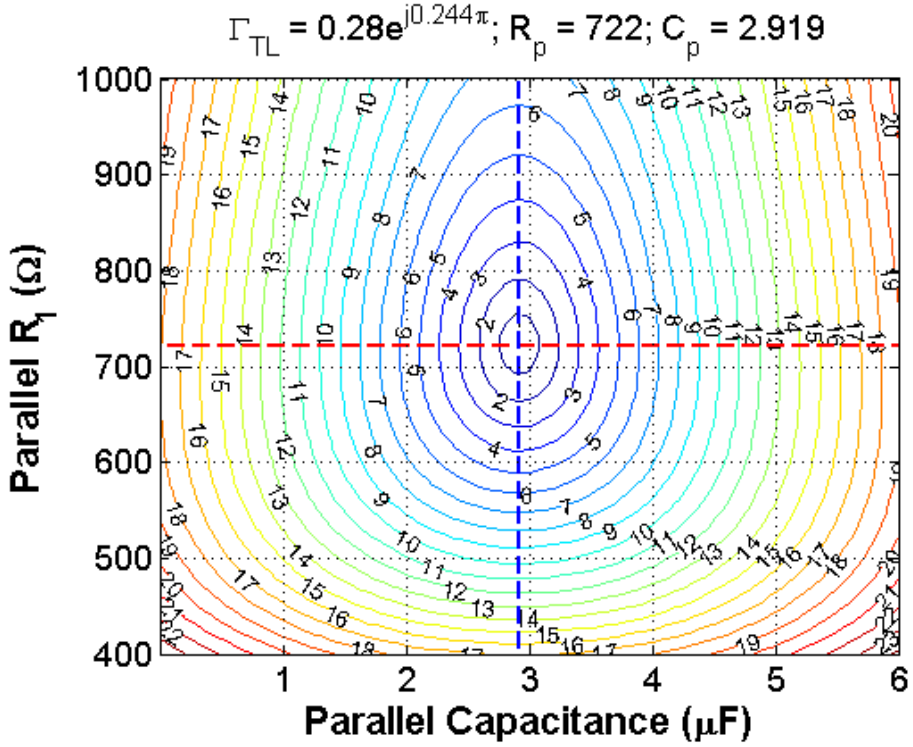

(b) resistance and capacitance connected in parallel

Fig. 5-15 Equal magnitude contours (in μA) for I_1 over the *C*-*R* grid, under the conditions for May 25th's experiment, on the west side ($x = -6$m), $\Gamma_{TL} = 0.28e^{j0.244\pi}$.

From Fig. 5-15, in a fairly large area around each of the intersections, the induced current is significantly less than the minimum 10μA measured in Fig. 5-13. If these predictions are correct, there should be a good chance to find the null when the settings of *C* and *R* are near the intersection. Even if the null cannot be exactly reached, a small induced current should be easily observed over a relatively wide range of resistance and capacitance. In May 25th's experiment, the induced current was checked over a fairly large *C*-*R* grid (at least ±400Ω and ±5μF from the center point) around the theoretical null point and in relatively fine steps (i.e., 10Ω and 0.1μF). However, no obvious null was observed during the experiment. Additionally, by introducing in the capacitance, the minimum of the induced current measured in the experiment was about 17.5μA (the minimum without using capacitance is about 20μA). Since the step changes in *R* & *C* were much smaller than the range over which the current is < 10μA, the possibility that the null was missed is very small. Hence the uncertainty in resistor and capacitor values can also be excluded from the reasons for which the null was not found.

As discussed before, the reflection coefficient Γ_{TL} is among the parameters that is not known. Only some predictions as shown in Table 5-4 can be made for it. Thus, Γ_{TL} could be a factor causing the missed null in the induced current. To validate this, the case for only a resistance load was examined. Under the same conditions as those for Fig. 5-14, several different values of Γ_{TL} were used to calculated the corresponding induced current I_1 and I_2, and the results are compared to the measured data. These are shown in Fig. 5-16.

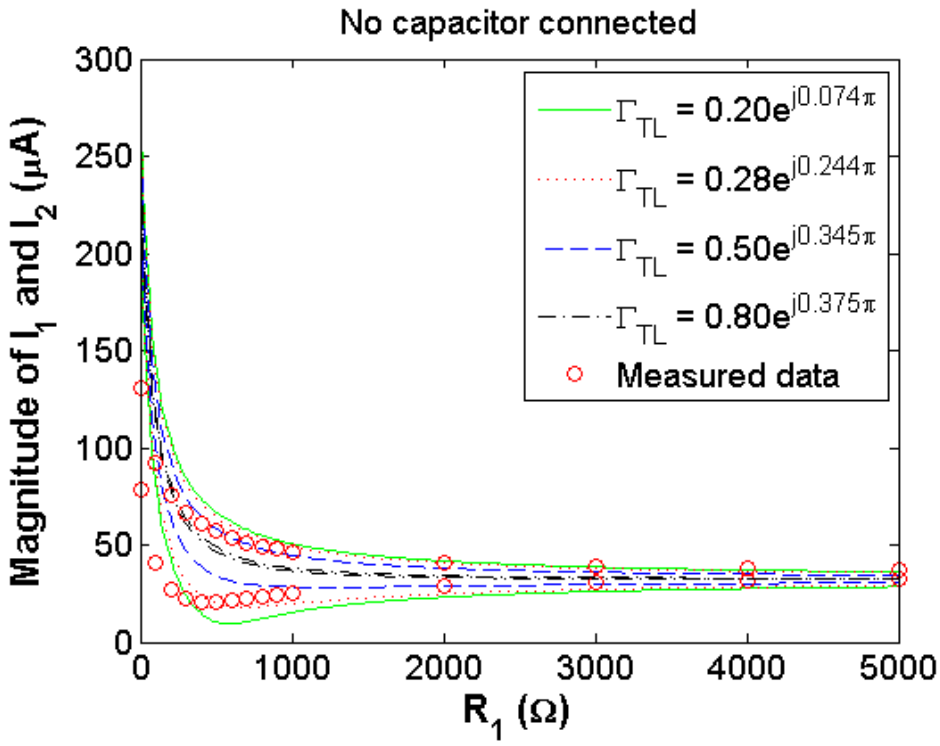

Fig. 5-16 Calculated I_1 and I_2 for different values of Γ_{TL} and compared to the measured data (on May 25th) when only resistance boxes being used, the sensor is under the phase conductor on the west side ($x = -6$m).

Generally speaking, the results for $\Gamma_{TL} = 0.28e^{j0.244\pi}$ have the best agreement with the measured data. This is why 0.28 was chosen to be the magnitude of Γ_{TL} for all the previous simulations. When the magnitude of Γ_{TL} increases, the agreement becomes worse, which validates the prediction made before that Γ_{TL} should have relatively small magnitude. Second, the capacitance is added in the simulations. Similar maps of the induced current as shown in Fig. 5-15 are drawn for the cases that $\Gamma_{TL} = 0.5e^{j0.345\pi}$ and $0.8e^{j0.375\pi}$ (series connection of R and C) and shown in Fig. 5-17 (a) and (b), respectively.

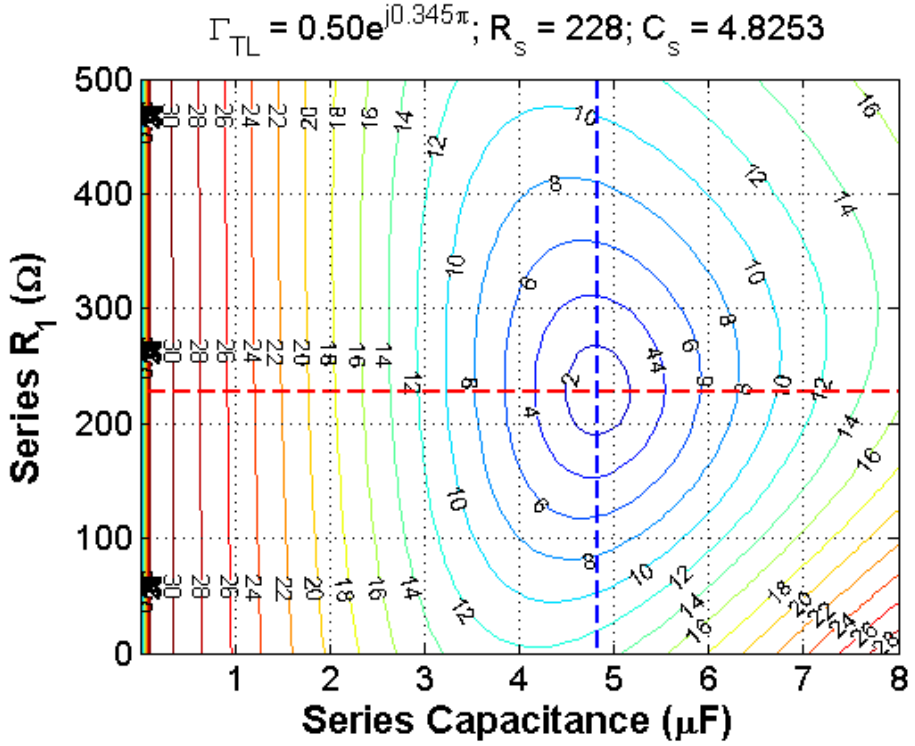

(a) $\Gamma_{TL} = 0.5e^{j0.345\pi}$

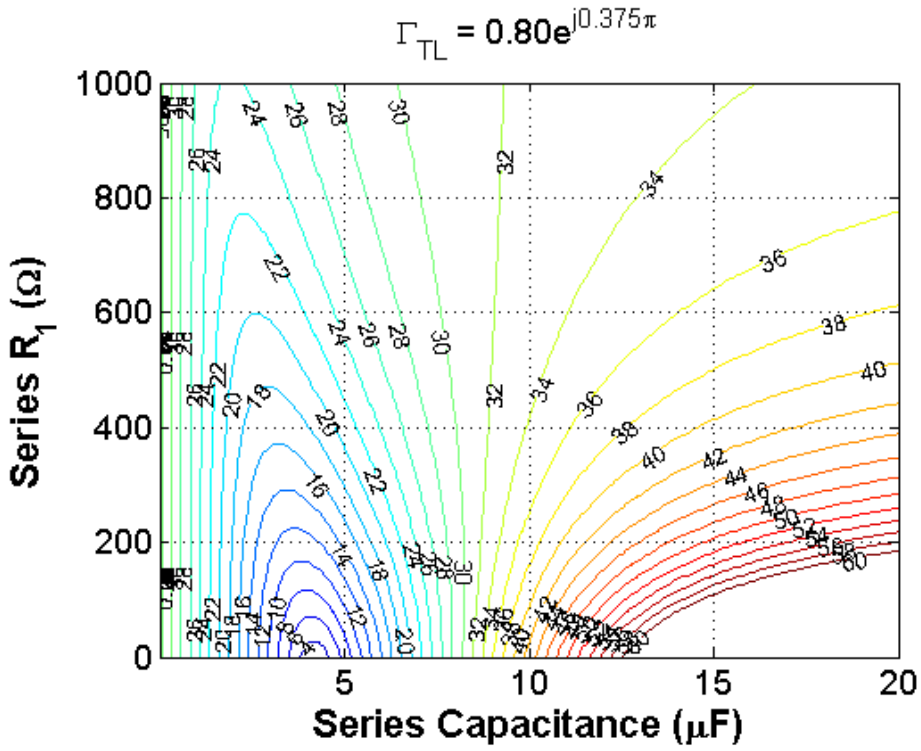

(b) $\Gamma_{TL} = 0.8e^{j0.375\pi}$

Fig. 5-17 Equal magnitude contours (in μA) of I_1 over the *C*-*R* grid for (a) $\Gamma_{TL} = 0.5e^{j0.345\pi}$ and (b) $\Gamma_{TL} = 0.8e^{j0.375\pi}$, on the west side ($x = -6$m).

In Fig. 5-17 (a), the null in I_1 (< 10 μA) still can be observed in a relatively large

area. Thus, similar comments made about Fig. 5-15 can apply here. However, in Fig. 5-17 (b), no null in I_1 exists because the calculated Z_1 for this case has negative real part (the null would occur in the IV quadrant), which is physically impossible. So, when the magnitude of Γ_{TL} is large (0.8 for instance), it is possible that no null of the induced current will occur for any values of the resistor and capacitor. From this point of view, the reflection coefficient Γ_{TL} could be the factor that causes no null to be observed in the experiment. But based on the discussion made for Fig. 5-16, it is not likely that Γ_{TL} could have a large magnitude (close to 1). Therefore, the possibility that Γ_{TL} is the reason for the lack of a null is not strong.

Finally, it was noticed that the current on the power line is a little unbalanced (see Table 5-1) with the three phase currents of 218, 237, and 225A, respectively. Simulation results show that some unbalance situations for the power line current can result in a value for Z_1 that has a negative real part or positive imaginary part (which means inductors instead of capacitors are required to find the null). For example, assume the unbalanced three-phase currents are ($218\angle 18^\circ$, $237\angle -120^\circ$, $225\angle 120^\circ$) rather than the balanced ones ($225\angle 0^\circ$, $225\angle -120^\circ$, $225\angle 120^\circ$), then the Z_1 causing the null is $Z_1 = 124 + j1107\Omega$, requiring inductor to be connected in the system. If that is the case, the unbalance power line current could be the reason why the null is not observed. But, again, the exact situation of the unbalance cannot be calculated due to that the phase angle of the power line current is unknown. For this reason, it cannot be concluded for certain that the unbalance of the power line current is the factor that leads to the absence in a null being found.

Although the null has not been observed during the experiments and the reason causing this is still not very clear, the results of the experiments provide strong (if not perfect) validation for the theory of the directional coupler introduced in section 5.1. The experiments are also helpful for understanding the mechanisms of the directional coupler and revealing the problems related to using the directional coupler for power transmission lines.

CHAPTER 6

LOW FREQUENCY DIPOLE IN THREE-LAYER MEDIUM

The subject of this chapter is independent of the research introduced in the first five chapters. It is written in the dissertation because this project is an important part of my research work during the time in Washington State University and some interesting and useful results have been obtained from the study of the project.

The electromagnetic fields due to a dipole buried in the half-space or layered conducting medium have been well studied for long time [57] – [61] This project is composed by two parts. In the first part, the electromagnetic fields due to a dipole (electric or magnetic, vertical or horizontal) placed above or buried in the upper layer of a two-layer conducting medium are formulated by using the Sommerfeld integrals. That is followed by the numerical validations for the formulations at the extremely low frequency (ELF). In the second part, the ELF wave propagation in the conducting medium when both the dipole and observation point are near the interface between the free space and the conducting medium is studied by simplifying the formulations obtained by the Sommerfeld integral method and interpreting the simplified results by an up-over-and-down propagation model. To conveniently conduct this study, the two layer conducting medium is replaced by a half space conducting medium since the effect of the lower half space conducting medium on the fields can be ignored if the thickness of the upper layer is large enough and the dipole and the observation point are close enough to the upper interface. For this case, the source dipole is, again, chosen to be a HED buried in the half space conducting medium.

6.1 Model

In the model considered in this project, Fig. 6-1, there is a layer of conducting medium (conducting medium #1), with uniform thickness of d meters, between the top half space of free space and the bottom half space of conducting medium (conducting medium #2) with different electric characteristics to the upper one. The two interfaces between the three mediums are horizontal and at $z = 0$ and $z = -d$. As noted in the figure, ε_i and σ_i are the permittivity and conductivity of the conducting medium #i (i = 1 and 2). $\varepsilon_i = \varepsilon_{ri}\varepsilon_0$, where ε_{ri} is the relative permittivity and ε_0 is the permittivity of free space. σ_0 is the conductivity of the free space and $\sigma_0 = 0$. It is assumed that all materials have the permeability of free space μ_0.

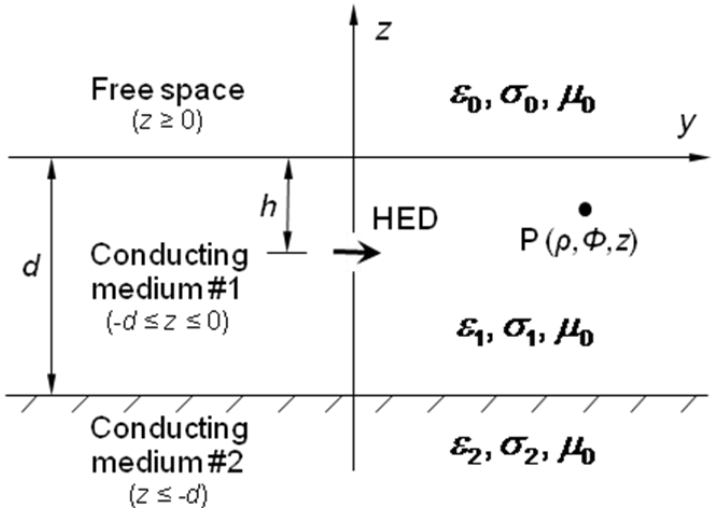

Fig. 6-1 Model of the three-layer medium with a HED buried in the conducting medium #1 (middle layer)

In this project, the dipole source is allowed to be placed above or buried in the conducting medium #1. Therefore, according to the type (electric or magnetic), orientation (vertical or horizontal) and position (in free space or conducting medium

#1) of the dipole, there are eight different cases of dipole source to be studied, the models of which are shown in Table 6-1.

Table 6-1 Models for the eight cases of different dipole sources

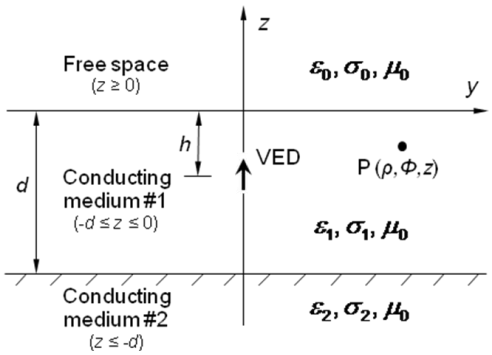 VED in conducting medium #1	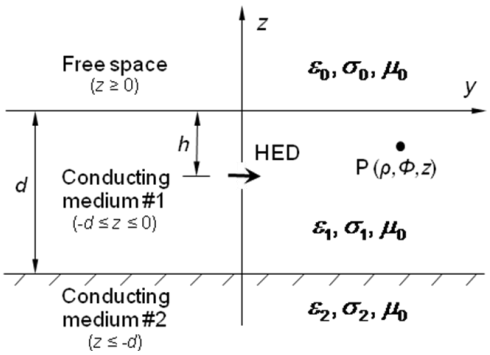 HED in conducting medium #1
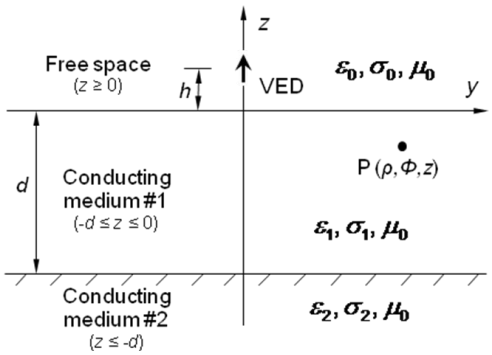 VED in free space	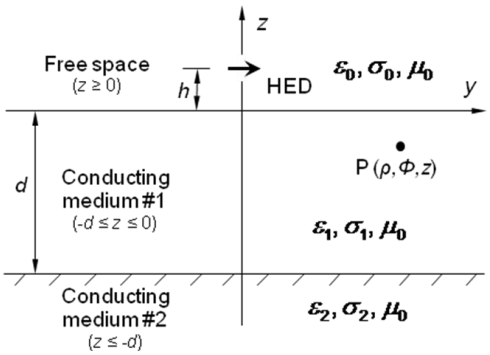 HED in free space
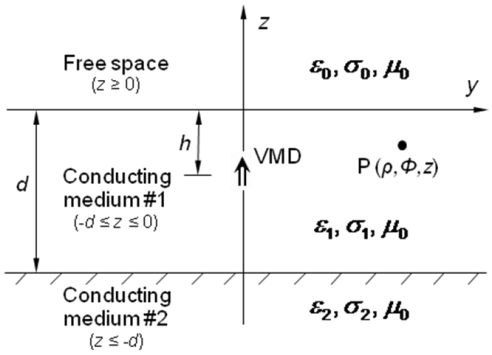 VMD in conducting medium #1	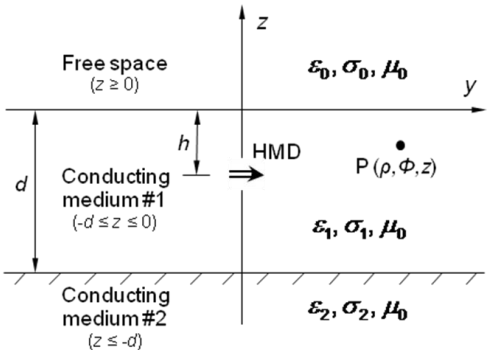 HMD in conducting medium #1
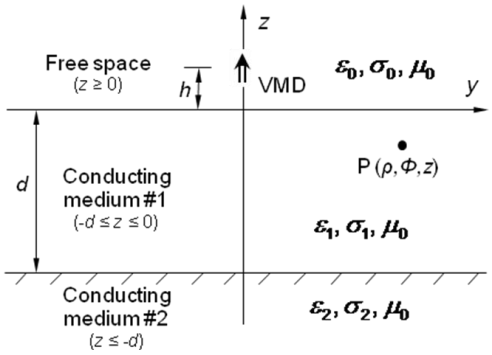 VMD in free space	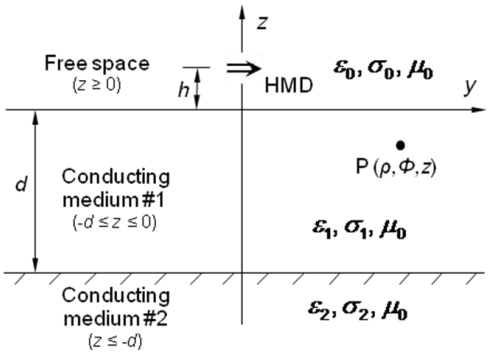 HMD in free space

The cylindrical coordinate system (ρ, φ, z) is used, where $x = \rho\cos\varphi$ and $y = \rho\sin\varphi$. In the eight cases, the vertical and horizontal dipoles are assumed to be oriented in 'z' and 'y' directions, respectively. The vertical distance of the dipole to the interface between the free space and conducting medium #1 is h meters (above or below the interface for different cases). The case for Fig. 6-1, a horizontal electric dipole (HED) buried in the conducting medium #1, will be used as the example to show the formulations of the electromagnetic fields at the observation point P(ρ, φ, z) anywhere in the model. For the other seven cases, similar process applies and only the results will be provided.

6.2 Formulations by Sommerfeld integrals

In Fig. 6-1, the HED, with a dipole moment of Idl (A-m), is on the 'z' axis. Applying Sommerfeld integrals to formulate the electric (E) and magnetic (H) fields uses the integral representations of vector potentials and requires two non-zero components of the vector potential. For the HED in this case, the y and z components of the magnetic vector potential, A_y and A_z, are chosen.

$$A_y^0 = K_1 \int_0^\infty f_1(\lambda) e^{-u_0 z} \lambda J_0(\lambda\rho) d\lambda \quad (z \geq 0) \tag{6.1}$$

$$A_y^1 = K_1 \frac{e^{\gamma_1 R}}{R} + K_1 \int_0^\infty \left[f_2(\lambda) e^{-u_1 z} + f_3(\lambda) e^{u_1 z} \right] \lambda J_0(\lambda\rho) d\lambda \quad (-d \leq z \leq 0) \tag{6.2}$$

$$A_y^2 = K_1 \int_0^\infty f_4(\lambda) e^{u_2 z} \lambda J_0(\lambda\rho) d\lambda \quad (z \leq -d) \tag{6.3}$$

$$A_z^0 = K_1 \frac{\partial}{\partial y} \int_0^\infty g_1(\lambda) e^{-u_0 z} \lambda J_0(\lambda\rho) d\lambda \quad (z \geq 0) \tag{6.4}$$

$$A_z^1 = K_1 \frac{\partial}{\partial y} \int_0^\infty \left[g_2(\lambda) e^{-u_1 z} + g_3(\lambda) e^{u_1 z} \right] \lambda J_0(\lambda\rho) d\lambda \quad (-d \leq z \leq 0) \tag{6.5}$$

$$A_z^2 = K_1 \frac{\partial}{\partial y} \int_0^\infty g_4(\lambda) e^{u_2 z} \lambda J_0(\lambda\rho) d\lambda \quad (z \le -d) \tag{6.6}$$

where $J_0(\lambda\rho)$ is the Bessel function of the first kind of order zero and

$$\gamma_i^2 = -\omega^2 \mu \varepsilon_i' = -\omega^2 \mu (\varepsilon_i - j\frac{\sigma_i}{\omega})$$

$$u_i = \sqrt{(\lambda^2 + \gamma_i^2)}$$

$$K_1 = \frac{\mu_0 I dl}{4\pi}$$

ε_i' is the complex permittivity of the conducting medium #i (i = 1 or 2) and for the free space $\varepsilon_0' = \varepsilon_0$. γ_i is the wave number where Re(γ_i) ≤ 0 and Re(u_i) ≥ 0 define the proper Riemann sheet of the complex plane. The first term $K_1 e^{\gamma_1 R}/R$ in (6.2) is the source term and $R = [\rho^2 + (z + h)^2]^{1/2}$ is the distance from the dipole to the observation point. The source term is the vector potential of the dipole itself in an infinite homogeneous conducting medium. It can be written in integral form as

$$\frac{e^{\gamma_1 R}}{R} = \begin{cases} \int_0^\infty u_1^{-1} e^{-u_1(z+h)} \lambda J_0(\lambda\rho) d\lambda & (z+h) \ge 0 \\ \int_0^\infty u_1^{-1} e^{u_1(z+h)} \lambda J_0(\lambda\rho) d\lambda & (z+h) \le 0 \end{cases} \tag{6.7}$$

Functions $f_1 \sim f_4$ and $g_1 \sim g_4$ are arbitrary coefficient functions of the integral variable λ and determined by matching the boundary conditions on the two interfaces at z = 0 and z = $-d$. To find the solutions to the fields, the first step is to determine these coefficient functions.

Given the magnetic vector potentials, the E and H fields can be calculated by the Maxwell's equations. The expanded expressions of the E and H field components are

$$E_x = -\frac{j}{\omega\mu\varepsilon} \cdot \frac{\partial}{\partial x} (\frac{\partial A_y}{\partial y} + \frac{\partial A_z}{\partial z}) \tag{6.8}$$

$$E_y = -\frac{j}{\omega\mu\varepsilon}\cdot\left[\frac{\partial}{\partial y}\left(\frac{\partial A_y}{\partial y}+\frac{\partial A_z}{\partial z}\right)-\gamma^2 A_y\right] \tag{6.9}$$

$$E_z = -\frac{j}{\omega\mu\varepsilon}\cdot\left[\frac{\partial}{\partial z}\left(\frac{\partial A_y}{\partial y}+\frac{\partial A_z}{\partial z}\right)-\gamma^2 A_z\right] \tag{6.10}$$

$$H_x = \frac{1}{\mu}\left(\frac{\partial A_z}{\partial y}-\frac{\partial A_y}{\partial z}\right) \tag{6.11}$$

$$H_y = -\frac{1}{\varepsilon}\frac{\partial A_z}{\partial x} \tag{6.12}$$

$$H_z = \frac{1}{\varepsilon}\frac{\partial A_y}{\partial x} \tag{6.13}$$

The boundary conditions to be satisfied are that all the tangential fields are continuous on the interfaces at $z = 0$ and $z = -d$ plane. They can be written as

On $z = 0$ plane	On $z = -d$ plane
$\frac{1}{\varepsilon_0'}\left(\frac{\partial A_y^0}{\partial y}+\frac{\partial A_z^0}{\partial z}\right)=\frac{1}{\varepsilon_1'}\left(\frac{\partial A_y^1}{\partial y}+\frac{\partial A_z^1}{\partial z}\right)$	$\frac{1}{\varepsilon_2'}\left(\frac{\partial A_y^2}{\partial y}+\frac{\partial A_z^2}{\partial z}\right)=\frac{1}{\varepsilon_1'}\left(\frac{\partial A_y^1}{\partial y}+\frac{\partial A_z^1}{\partial z}\right)$
$A_y^0 = A_y^1$	$A_y^2 = A_y^1$
$A_z^0 = A_z^1$	$A_z^2 = A_z^1$
$\frac{\partial A_y^0}{\partial z}=\frac{\partial A_y^1}{\partial z}$	$\frac{\partial A_y^2}{\partial z}=\frac{\partial A_y^1}{\partial z}$

Inserting the vector potentials from (6.1) through (6.6) into these boundary conditions and solving for the coefficient functions result in

$$f_1 = \frac{2}{D}\left[\left(u_2-u_1\right)e^{u_1(h-d)}-\left(u_2+u_1\right)e^{-u_1(h-d)}\right] \tag{6.14}$$

$$f_2 = \frac{\left(u_2-u_1\right)}{u_1\cdot D}\left[\left(u_1-u_0\right)e^{-u_1(h+d)}+\left(u_0+u_1\right)e^{u_1(h-d)}\right] \tag{6.15}$$

$$f_3 = \frac{\left(u_0-u_1\right)}{u_1\cdot D}\left[\left(u_1-u_2\right)e^{u_1(h-d)}+\left(u_2+u_1\right)e^{-u_1(h-d)}\right] \tag{6.16}$$

$$f_4 = \frac{2e^{u_2 d}}{D}\left[\left(u_0-u_1\right)e^{-u_1 h}-\left(u_0+u_1\right)e^{u_1 h}\right] \tag{6.17}$$

$$g_1 = \frac{(\varepsilon_1' - \varepsilon_0') f_1 \left[(\varepsilon_2' u_1 - \varepsilon_1' u_2) e^{-u_1 d} + (\varepsilon_2' u_1 + \varepsilon_1' u_2) e^{u_1 d} \right] + 2\varepsilon_0' u_1 (\varepsilon_2' - \varepsilon_1') e^{-u_2 d} f_4}{D_1} \quad (6.18)$$

$$g_2 = \frac{1}{D_1} \cdot \left[(\varepsilon_0' - \varepsilon_1')(\varepsilon_1' u_2 - \varepsilon_2' u_1) e^{-u_1 d} f_1 + (\varepsilon_2' - \varepsilon_1')(\varepsilon_1' u_0 + \varepsilon_0' u_1) e^{-u_2 d} f_4 \right] \quad (6.19)$$

$$g_3 = \frac{1}{D_1} \cdot \left[(\varepsilon_1' - \varepsilon_0')(\varepsilon_2' u_1 + \varepsilon_1' u_2) e^{u_1 d} f_1 + (\varepsilon_2' - \varepsilon_1')(\varepsilon_0' u_1 - \varepsilon_1' u_0) e^{-u_2 d} f_4 \right] \quad (6.20)$$

$$g_4 = \frac{2\varepsilon_2' u_1 (\varepsilon_1' - \varepsilon_0') e^{u_2 d} f_1 + (\varepsilon_2' - \varepsilon_1') f_4 \left[(\varepsilon_0' u_1 + \varepsilon_1' u_0) e^{u_1 d} + (\varepsilon_0' u_1 - \varepsilon_1' u_0) e^{-u_1 d} \right]}{D_1} \quad (6.21)$$

where

$$D = (u_1 - u_0)(u_1 - u_2) e^{-u_1 d} - (u_1 + u_0)(u_2 + u_1) e^{u_1 d}$$

$$D_1 = (\varepsilon_0' u_1 - \varepsilon_1' u_0)(\varepsilon_1' u_2 - \varepsilon_2' u_1) e^{-u_1 d} + (\varepsilon_0' u_1 + \varepsilon_1' u_0)(\varepsilon_1' u_2 + \varepsilon_2' u_1) e^{u_1 d}$$

With the coefficient functions known, the E and H field components in conducting medium #1 can be written in terms of Sommerfeld integrals by inserting (6.2) and (6.5) into (6.8) through (6.13) and evaluating the derivatives. Since the dipole source is buried in this layer of medium, the field components in this layer are formed by two parts: one is the incident field directly from the dipole source and the other one is the field reflected by the two interfaces. They are denoted by '*i*' and '*r*' in the subscript of the corresponding field component. The results are listed below.

$E_x^1 = E_{xi}^1 + E_{xr}^1$	$E_{xi}^1 = \frac{jIdl}{4\pi\omega\varepsilon_1'} \int_0^\infty \lambda^2 B_1 S_1 \sin(\phi)\cos(\phi) d\lambda$ $E_{xr}^1 = \frac{jIdl}{4\pi\omega\varepsilon_1'} \int_0^\infty \lambda^2 B_1 C_1 \sin(\phi)\cos(\phi) d\lambda$
$E_y^1 = E_{yi}^1 + E_{yr}^1$	$E_{yi}^1 = \frac{jIdl}{4\pi\omega\varepsilon_1'} \left[\int_0^\infty \lambda^2 B_2 S_1 d\lambda + \int_0^\infty S_1 \gamma_1^2 \lambda J_0(\lambda\rho) d\lambda \right]$ $E_{yr}^1 = \frac{jIdl}{4\pi\omega\varepsilon_1'} \left[\int_0^\infty \lambda^2 B_2 C_1 d\lambda + \int_0^\infty \left(e^{-u_1 z} f_2 + e^{u_1 z} f_3 \right) \cdot \gamma_1^2 \lambda J_0(\lambda\rho) d\lambda \right]$

$E_z^1 = E_{zi}^1 + E_{zr}^1$	$E_{zi}^1 = \frac{jIdl}{4\pi\omega\varepsilon_1'}\int_0^\infty \lambda^2 S_2 J_1(\lambda\rho)\sin(\phi)d\lambda$ $E_{zr}^1 = \frac{jIdl}{4\pi\omega\varepsilon_1'}\int_0^\infty \lambda^2 C_2 J_1(\lambda\rho)\sin(\phi)d\lambda$
$H_x^1 = H_{xi}^1 + H_{xr}^1$	$H_{xi}^1 = -\frac{Idl}{4\pi}\int_0^\infty \lambda S_1 J_0(\lambda\rho)d\lambda$ $H_{xr}^1 = \frac{Idl}{4\pi}\left[\int_0^\infty \left(u_1 e^{-u_1 z} f_2 - u_1 e^{u_1 z} f_3\right)\lambda J_0(\lambda\rho)d\lambda - \int_0^\infty B_2 C_3 \lambda^2 d\lambda\right]$
$H_y^1 = H_{yi}^1 + H_{yr}^1$	$H_{yi}^1 = 0$; $H_{yr}^1 = \frac{Idl}{4\pi}\int_0^\infty \lambda^2 B_1 C_3 \sin(\phi)\cos(\phi)d\lambda$
$H_z^1 = H_{zi}^1 + H_{zr}^1$	$H_{zi}^1 = -\frac{Idl}{4\pi}\int_0^\infty \lambda^2 S_1 J_1(\lambda\rho)\cos(\phi)d\lambda$ $H_{zr}^1 = -\frac{Idl}{4\pi}\int_0^\infty \left(e^{-u_1 z} f_2 + e^{u_1 z} f_3\right)\lambda^2 J_1(\lambda\rho)\cos(\phi)d\lambda$

where

$B_1 = \lambda J_0(\lambda\rho) - 2J_1(\lambda\rho)/\rho$	$B_2 = \lambda J_0(\lambda\rho)\sin^2(\phi) + J_1(\lambda\rho)\cos(2\phi)/\rho$
$C_1 = e^{-u_1 z} f_2 + e^{u_1 z} f_3 - u_1 e^{-u_1 z} g_2 + u_1 e^{u_1 z} g_3$	$C_3 = e^{-u_1 z} g_2 + e^{u_1 z} g_3$
$C_2 = -u_1 e^{-u_1 z} f_2 + u_1 e^{u_1 z} f_3 + \lambda^2 e^{-u_1 z} g_2 + \lambda^2 e^{u_1 z} g_3$	
$S_1 = \begin{cases} u_1^{-1} e^{-u_1(z+h)} & (z+h \geq 0) \\ u_1^{-1} e^{u_1(z+h)} & (z+h \leq 0) \end{cases}$	$S_2 = \begin{cases} -e^{-u_1(z+h)} & (z+h \geq 0) \\ e^{u_1(z+h)} & (z+h \leq 0) \end{cases}$

In the free space and conducting medium #2, there is no dipole source. Therefore, the field component contains only the transmitted field from the interface. The transmitted field is denoted by a '*t*' in subscript of each field component and the results for all the field components are listed below.

E and H fields in the free space:
$E_x^0 = E_{xt}^0 = \frac{jIdl}{4\pi\omega\varepsilon_0'}\int_0^\infty (f_1 - u_0 g_1) e^{-u_0 z} B_1 \lambda^2 \sin(\phi)\cos(\phi) d\lambda$
$E_y^0 = E_{yt}^0 = \frac{jIdl}{4\pi\omega\varepsilon_0'}\left[\int_0^\infty (f_1 - u_0 g_1) e^{-u_0 z} B_2 \lambda^2 d\lambda + \int_0^\infty \gamma_0^2 e^{-u_0 z} f_1 \lambda J_0(\lambda\rho) d\lambda\right]$
$E_z^0 = E_{zt}^0 = -\frac{jIdl}{4\pi\omega\varepsilon_0'}\int_0^\infty (u_0 f_1 - \lambda^2 g_1) e^{-u_0 z} \lambda^2 J_1(\lambda\rho)\cos(\phi) d\lambda$
$H_x^0 = H_{xt}^0 = -\frac{Idl}{4\pi}\left[\int_0^\infty e^{-u_0 z} g_1 B_2 \lambda^2 d\lambda - \int_0^\infty u_0 e^{-u_0 z} f_1 \lambda J_0(\lambda\rho) d\lambda\right]$
$H_y^0 = H_{yt}^0 = \frac{Idl}{4\pi}\int_0^\infty (e^{-u_0 z} g_1) B_1 \lambda^2 \sin(\phi)\cos(\phi) d\lambda$
$H_z^0 = H_{zt}^0 = -\frac{Idl}{4\pi}\int_0^\infty e^{-u_0 z} f_1 \lambda^2 J_1(\lambda\rho)\cos(\phi) d\lambda$

E and H fields in conducting medium #2:
$E_x^2 = E_{xt}^2 = \frac{jIdl}{4\pi\omega\varepsilon_2'}\int_0^\infty (f_4 + u_2 g_4) e^{u_2 z} B_1 \lambda^2 \sin(\phi)\cos(\phi) d\lambda$
$E_y^2 = E_{yt}^2 = \frac{jIdl}{4\pi\omega\varepsilon_2'}\left[\int_0^\infty (f_4 + u_2 g_4) e^{u_2 z} B_2 \lambda^2 d\lambda + \int_0^\infty \gamma_2^2 e^{u_2 z} f_4 \lambda J_0(\lambda\rho) d\lambda\right]$
$E_z^2 = E_{zt}^2 = \frac{jIdl}{4\pi\omega\varepsilon_2'}\int_0^\infty (u_2 f_4 + \lambda^2 g_4) e^{u_2 z} \lambda^2 J_1(\lambda\rho)\cos(\phi) d\lambda$
$H_x^2 = H_{xt}^2 = -\frac{Idl}{4\pi}\left[\int_0^\infty e^{u_2 z} g_4 \cdot B_2 \lambda^2 d\lambda + \int_0^\infty u_2 e^{u_2 z} f_4 \lambda J_0(\lambda\rho) d\lambda\right]$
$H_y^2 = H_{yt}^2 = \frac{Idl}{4\pi}\int_0^\infty (e^{u_2 z} g_4) B_1 \lambda^2 \sin(\phi)\cos(\phi) d\lambda$
$H_z^2 = H_{zt}^2 = -\frac{Idl}{4\pi}\int_0^\infty e^{u_2 z} f_4 \lambda^2 J_1(\lambda\rho)\cos(\phi) d\lambda$

The formulas of the E and H fields obtained in section 6.2 are evaluated by numerical integrations conducted by programs written in Matlab. Under certain

conditions, the calculation results are compared to the quasi-static fields due to a HED immersed in infinite medium for validation. The values of the parameters used in the following simulations are listed in Table 6-2. The conductivity and permittivity of the conducting medium #1 and #2 represent typical fresh lake water and lake bottom, respectively.

Table 6-2 Parameters used in the simulations for the numerical validation

Medium	Free space	Conducting medium #1	Conducting medium #2
Relative permittivity, ε_r	1	1	1
Conductivity, σ (S/m)	0	0.018	0.012
Permeability, μ (H/m)	$4\pi\times10^{-7}$	$4\pi\times10^{-7}$	$4\pi\times10^{-7}$
d (m)	300		
h (m)	vary from 0 to 300		
Dipole moment *Idl* (A-m)	1		
Dipole frequency *f* (Hz)	10 to 3000		

The method chosen for numerical integration is the composite Simpson's rule [62], which is used to obtain the integration of a given integrand *f(x)* over interval [*a*, *b*]. The integral formula of the Simpson's rule can be written as

$$\int_a^b f(x)dx = \frac{h}{3}\left[f(a) + 4f(x_1) + f(b)\right] - \frac{h^5}{90} f^{(4)}(\xi) \tag{6.22}$$

where x_1 is the middle point of [*a, b*] and $a \le \xi \le b$. The Simpson's rule is usually inaccurate if used over a large integration interval. To avoid this problem, a piecewise approach, the composite Simpson's rule, is often applied (see Fig. 6-2).

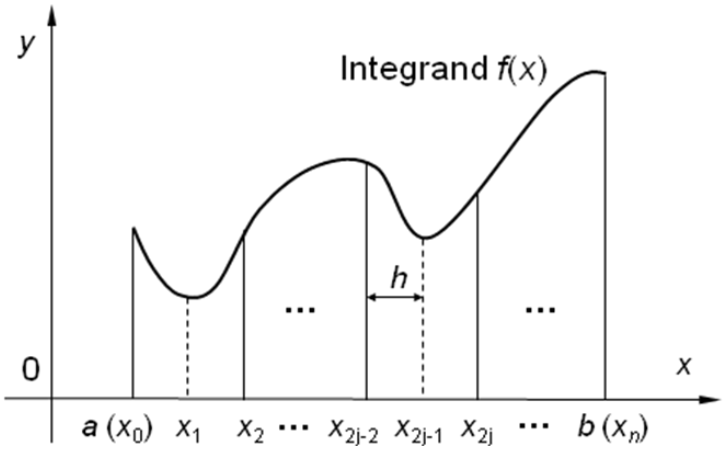

Fig. 6-2 Integration intervals for the composite Simpson's rule

The integration interval [*a*, *b*] is equally divided into *n* subintervals, where *n* must be an even number. Then apply the Simpson's rule on each subinterval and combine all the integrations over each subinterval to get the final integration. In formula, the composite Simpson's rule is described as

$$\int_a^b f(x)dx = \frac{h}{3}\left[f(x_0) + 2\sum_{j=1}^{(n/2)-1} f(x_{2j}) + 4\sum_{j=1}^{n/2} f(x_{2j-1}) + f(x_n) \right] - \frac{h^5}{90}\sum_{j=1}^{n/2} f^{(4)}(\xi_j) \quad (6.23)$$

where $x_{2j-2} \le \xi_j \le x_{2j}$, for each $j = 1, 2, \ldots, n/2$. When the numerical integration is carried out, the error term is usually truncated.

$$\int_a^b f(x)dx \approx \frac{h}{3}\left[f(x_0) + 2\sum_{j=1}^{(n/2)-1} f(x_{2j}) + 4\sum_{j=1}^{n/2} f(x_{2j-1}) + f(x_n) \right] \quad (6.24)$$

Theoretically, the exact formulas of the fields will be given by the integration from zero to infinity. But it is not possible to do this in a numerical manner. The computer program can only deal with integration over finite intervals. To make the calculation possible, some approximation should be made. First, an integral can be separated into two parts

$$\int_0^{\infty} f(x)dx = \int_0^{b} f(x)dx + \int_b^{\infty} f(x)dx \tag{6.25}$$

If a bound number '*b*' can be found such that the second integral on the right hand side is small enough compared to the first integral, then the total integral can be approximated by the first term. Since the integrands in the formulas of the fields have attenuation characteristics, it is not difficult to find the bound number and the exact integrals can be approximated by

$$\begin{aligned} \int_0^{\infty} FI(\lambda)d\lambda &= \int_0^{\lambda\max} FI(\lambda)d\lambda + \int_{\lambda\max}^{\infty} FI(\lambda)d\lambda \\ &\approx \int_0^{\lambda\max} FI(\lambda)d\lambda \end{aligned} \tag{6.26}$$

where *FI(λ)* represents integrand for field integration, λ_{max} is the upper limit of the integration interval to be used in numerical calculation. In practice, for the parameters given in Table 6-2, λ_{max} is about 50 to 100 for the integrals due to the term

$$\frac{e^{\gamma_1 R}}{R} = \begin{cases} \int_0^{\lambda_{\max}} u_1^{-1} e^{-u_1(z+h)} \lambda J_0(\lambda\rho)d\lambda & (z+h) \geq 0 \\ \int_0^{\lambda_{\max}} u_1^{-1} e^{u_1(z+h)} \lambda J_0(\lambda\rho)d\lambda & (z+h) \leq 0 \end{cases}$$

Usually, this value of λ_{max} will give us enough accuracy for calculation. For the reflected field integrals, which contain the coefficient functions $f_1 \sim f_4$ and $g_1 \sim g_4$, the value of λ_{max} is limited by the computation number limit of Matlab (about 10^{324}). Usually, its range is from 1.0 to 2.5 for stable and acceptably accurate computation.

The integral step *h* is another important factor to the numerical integration. Too large steps not only bring big error but also cause bad behavior (strong oscillation) of the calculation. Small steps, however, slow down the speed of computation. The Bessel functions are the major source of the oscillation. The integral step *h* is usually determined by avoiding the oscillation of the Bessel functions and assuring the

computation speed at the same time. Typical value of h is chosen based on the rule that the number of sample points on a wavelength of the Bessel function is between 30 to 50.

With the parameters of the integration being determined, the E and H fields due to the HED shown in Fig. 6-1 are calculated by a Matlab program conducting the composite Simpson's rule for the numerical integrations. The near-field results for the case in which the HED is place at the middle of the conducting medium #1 are compare to the quasi-static fields of the HED immersed in infinite conducting medium #1. This is reasonable because the thickness of the conducting medium #1 is large (300m) and the reflected fields due to the interfaces are very small and ignorable if the HED is far away from the interfaces (such as at the middle of the layer).

Fig. 6-3 (a) and (b) show the results of Ex and Hz by the integration compared to the corresponding quasi-static field components. The HED is 150 meters below the upper interface (h = 150). The observation points are at z = -149m and on the axis having a 'φ' angle of $\pi/4$. The frequency of the dipole is 1000Hz.

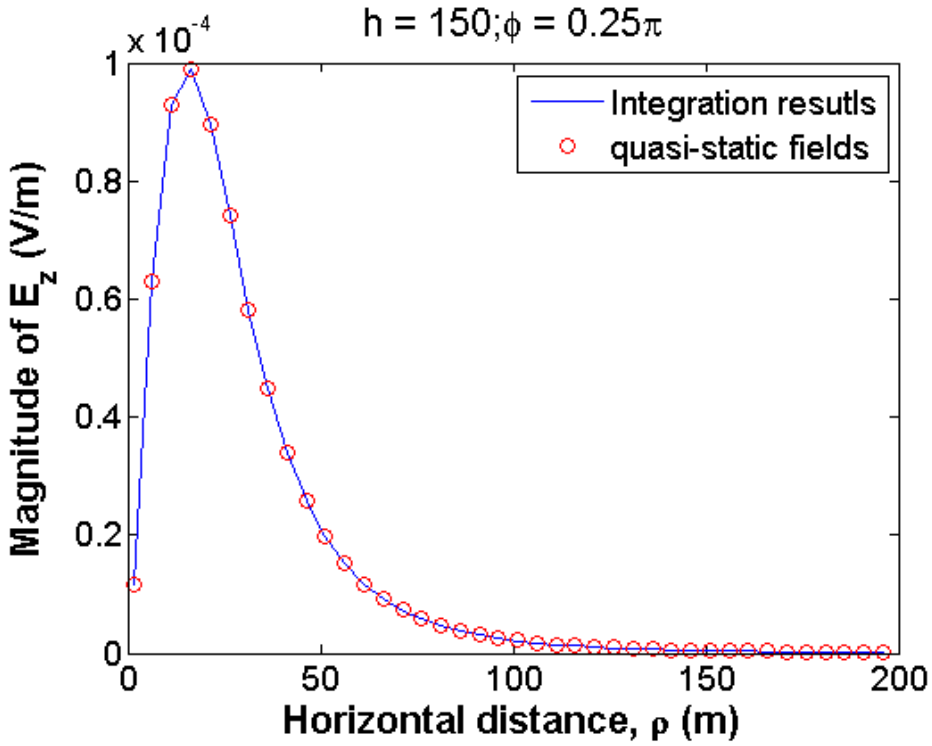

(a) E_z

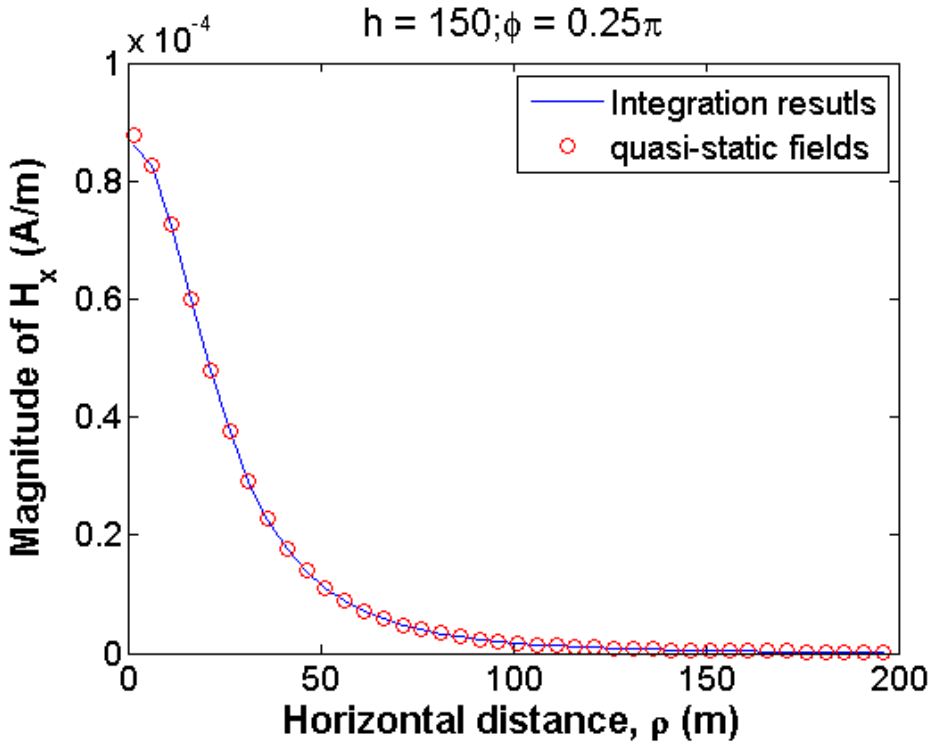

(b) H_x

Fig. 6-3 Comparisons between the fields by integration and the quasi-static fields for (a) E_z and (b) H_x

In these figures, the solid lines represent the results by the integration method s and the circles are for the quasi-static results. It is clear that, as expected, the two sets of the results match each other very well when ρ is small.

6.3 Up-over-and-down interpretation of the field propagations

When the thickness of the conducting medium #1shwon in Fig. 6-1 is large and the HED and the observation point are relatively close to the upper interface (free space – medium #1 interface), i.e., $d >> h, |z|$, the half space of conducting medium #2 has little effect on the fields at the observation point due to the lossyness of medium #1. For this case, medium #2 can be ignored and the model in Fig. 6-1 reduces to a HED buried in half space of conducting medium #1, as shown in Fig. 6-4. All the parameters here, if applicable, are the same as defined for the model in Fig. 6-1.

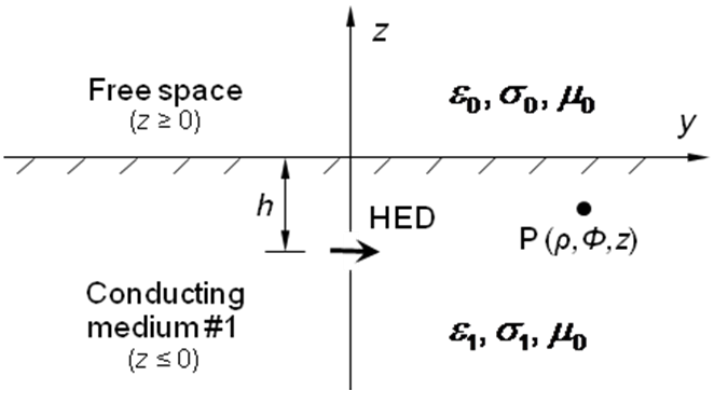

Fig. 6-4 Model of a HED buried in lower half space of conducting medium #1

Further, when the horizontal spacing between the dipole and the observation point is much larger than their vertical distance from the interface and the frequency is “low”, it is possible to interpret the propagation mechanism as a simple up-over-and- down process. Here, up-over-and-down, as illustrated in Fig. 6-5, means that the field

propagates vertically up crossing the interface to the free space medium, then propagates horizontally along the interface, and finally propagates vertically down to the observation point. While this behavior is somewhat similar to the high frequency phenomenon observed by previous authors [63], it is also different because the fields in the free space region are quasi-static.

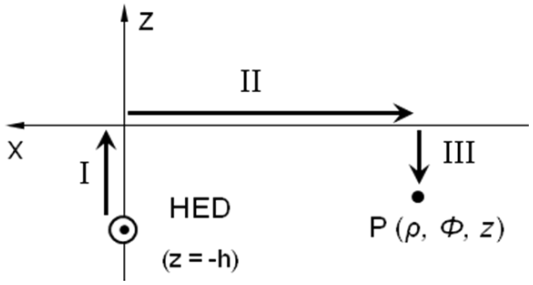

Fig. 6-5 Illustration of the up-over-and-down path.

For this case, the formulations for the E and H fields at the observation point can be obtained by the same method of Sommerfeld integral as introduced in previous section. Although the results are simpler because of the simpler model used, they are still complicated enough to keep one from readily seeing the physical process, behind those formulas, of wave propagation. Therefore, first, the Sommerfeld integrals of the vector potentials (similar to those shown in (6.1) to (6.6)) are simplified by using some reasonable assumptions given the range of parameters of interest. Then a set of simple but very good approximations to the electric and magnetic fields are derived from the Maxwell's equations using the simplified vector potentials. Based on these approximations, the up-over-and- down behavior is observed and interpreted. The dipole source here is chosen to be a HED because, using achievable dipole moments and commonly available receiving equipment, it can be shown that the HED fields are

detectable at larger distances than those of other dipole types (VED, VMD, and HMD). To be more specified, it was assumed from this study that the maximum dipole moments for electric and magnetic dipoles are 50 A-m and 2500 A-m^2 respectively and that the minimum detectable electric and magnetic fields are 1μV/m and 40μA/m respectively. Using these values, the horizontal electric field component that is perpendicular to the HED direction can be detected to a distance of 800 meters to the source. No other field component from any other dipole can be detected beyond about 200 meters.

The vector potentials for using the Sommerfeld integral method are chosen to be the *y* and *z* components of the magnetic vector potential, A_y and A_z. They can be written as

$$A_y^0 = K_1 \int_0^\infty f_1(\lambda) e^{-u_0 z} \lambda J_0(\lambda\rho) d\lambda \quad (z \geq 0) \tag{6.27}$$

$$A_y^1 = K_1 \frac{e^{-jk_1 R}}{R} + K_1 \int_0^\infty f_2(\lambda) e^{u_1 z} \lambda J_0(\lambda\rho) d\lambda = K_1 \frac{e^{-jk_1 R}}{R} + K_1 I_{y1} \quad (z \leq 0) \tag{6.28}$$

$$A_z^0 = K_1 \frac{\partial}{\partial y} \int_0^\infty g_1(\lambda) e^{-u_0 z} \lambda J_0(\lambda\rho) d\lambda \quad (z \geq 0) \tag{6.29}$$

$$A_z^1 = K_1 \frac{\partial}{\partial y} \int_0^\infty g_2(\lambda) e^{u_1 z} \lambda J_0(\lambda\rho) d\lambda = K_1 \frac{\partial}{\partial y} I_{z1} \quad (z \leq 0) \tag{6.30}$$

where $J_0(\lambda\rho)$ is the Bessel function of the first kind of order zero and

$$k_i^2 = \omega^2 \mu_0 \varepsilon_i' = \omega^2 \mu_0 (\varepsilon_i - j \frac{\sigma_i}{\omega})$$

$$u_i = \sqrt{(\lambda^2 - k_i^2)}$$

$$K_1 = \frac{\mu_0 I dl}{4\pi}$$

ε_i' is the complex permittivity of the i^{th} half space (i = 0 or 1 for free space and

conducting medium, respectively, and $\varepsilon_i' = \varepsilon_0$). k_i is the wave number where $\mathrm{Re}(k_i) \geq 0$ and $\mathrm{Re}(u_i) \geq 0$ define the proper Reimann sheet of the complex plane. The first term in (6.28) is the source term and $R = [\rho^2 + (z + h)^2]^{1/2}$ is the distance from the dipole to the observation point. I_{y1} and I_{z1} represent the integral terms in (6.28) and (6.30), respectively. The source term $K_1 e^{-jk_1 R}/R$ in (6.28) is the vector potential of the dipole itself in an infinite homogeneous conducting medium. It can be written in integral form as

$$\frac{e^{-jk_1 R}}{R} = \begin{cases} \int_0^\infty u_1^{-1} e^{-u_1(z+h)} \lambda J_0(\lambda\rho) d\lambda & (z+h) \geq 0 \\ \int_0^\infty u_1^{-1} e^{u_1(z+h)} \lambda J_0(\lambda\rho) d\lambda & (z+h) \leq 0 \end{cases} \tag{6.31}$$

The coefficient functions f_1, f_2, g_1 and g_2 are determined by matching the boundary conditions at $z = 0$.

$$f_1 = \frac{2e^{-u_1 h}}{u_0 + u_1} \tag{6.32}$$

$$f_2 = \frac{(u_1 - u_0) e^{-u_1 h}}{u_1 \cdot (u_0 + u_1)} \tag{6.33}$$

$$g_1 = g_2 = \frac{2(\varepsilon_1' - \varepsilon_0) e^{-u_1 h}}{(u_0 + u_1)(\varepsilon_1' u_0 + \varepsilon_0 u_1)} \tag{6.34}$$

6.3.1 Simplification of the integral of I_{z1} and I_{y1}

The objective here is to derive simple but acceptable approximations for the fields, which can be interpreted to provide good insight into the physical behavior of the wave propagating from source to receiver. One fundamental problem with evaluating the integrals shown in (6.27) to (6.30) is that, for large values of ρ compared to h and z, the rapid oscillations of the Bessel function cause difficulties with the numerical

integration. To remedy this problem, the contours of integration will be deformed in the complex plane so that the integrand decays exponentially for large values of ρ. This transformation will also allow other simplifying approximations that will lead to a simple interpretation of the final result.

If (6.34) is inserted into the integral portion of (6.30) and the exponential term is removed from $g_2(\lambda)$, this integral becomes

$$I_{z1} = \int_0^{\infty} g_2'(\lambda) e^{u_1(z-h)} \lambda J_0(\lambda\rho) d\lambda \tag{6.35}$$

where

$$g_2'(\lambda) = \frac{2(\varepsilon_1' - \varepsilon_0)}{(u_0 + u_1)(\varepsilon_1' u_0 + \varepsilon_0 u_1)} \tag{6.36}$$

Using the identities $J_0(x) = \frac{1}{2}\left[H_0^{(1)}(x) + H_0^{(2)}(x)\right]$ and $H_0^{(1)}(-x) = -H_0^{(2)}(x)$, where $H_0^{(1)}(x)$ and $H_0^{(2)}(x)$ are the Hankel functions of the first and second kind of order zero, respectively, the integral range in (6.35) can be expanded to (-∞, +∞). Since u_0, u_1, and $g_2'(\lambda)$ are all even functions of λ

$$I_{z1} = \frac{1}{2}\int_{-\infty}^{+\infty} g_2'(\lambda) e^{u_1(z-h)} \lambda H_0^{(2)}(\lambda\rho) d\lambda \,. \tag{6.37}$$

For the function $g_2'(\lambda)$, there is one pole, λ_p, and two branch points, k_0 and k_1, in the complex λ plane. The branch cuts are selected to be vertical lines from the branch points to negative infinity. Then the integral contour in (6.37) can be deformed into a contour C_B which is illustrated with the dashed line in Fig. 2.

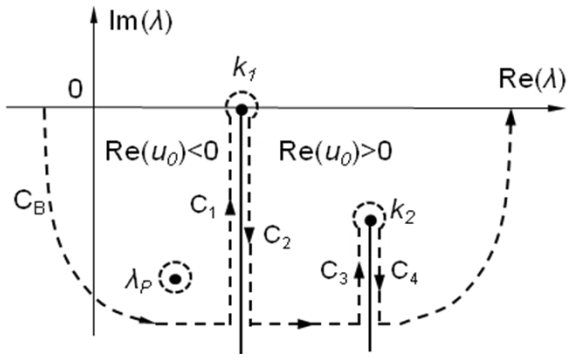

Fig. 6-6 Deformation of the integral contour for the integration of I_{z1}

With this deformation and the fact that the Hankel function goes to zero exponentially along the infinite semi-circle, the integral along the real axis is converted to the residue of the pole, $R_{\lambda p}$, plus the integrations along $C_1 \rightarrow C_4$, which encompass the two branch cuts. Thus

$$I_{z1} = \frac{1}{2}\int_{C_1+C_2+C_3+C_4} g_2'(\lambda) e^{u_1(z-h)} \lambda H_0^{(2)}(\lambda\rho) d\lambda + R_{\lambda p} \tag{6.38}$$

For $|k_1| >> |k_0|$, the integral along the branch cut of k_1 is much smaller than that of k_0 and can be ignored. Note that, in the complex plane, the sign of u_0 will change when crossing the branch cut associated with k_0. Given the choice of branch cut, $\mathrm{Re}(u_0)<0$ and $\mathrm{Re}(u_0)>0$ on the left and right sides, respectively, as shown in Fig. 6-6. In addition while the pole is in the proximity of the branch cut integration and is evident in the integrand, its contribution to the integral is negligible for the low frequencies considered here. Thus the pole residue can be ignored. Therefore

$$I_{z1} \approx \frac{1}{2}\int_{C_1+C_2} g_2'(\lambda) e^{u_1(z-h)} \lambda H_0^{(2)}(\lambda\rho) d\lambda \tag{6.39}$$

Fig. 6-7 shows the comparisons between the magnitude of the total integration of I_{z1} (6.38), the integration along the branch cut of k_0 (6.39), and the residue. The depth of the HED and observation point are assumed to be 20m and 10m for this and all the

following simulations.

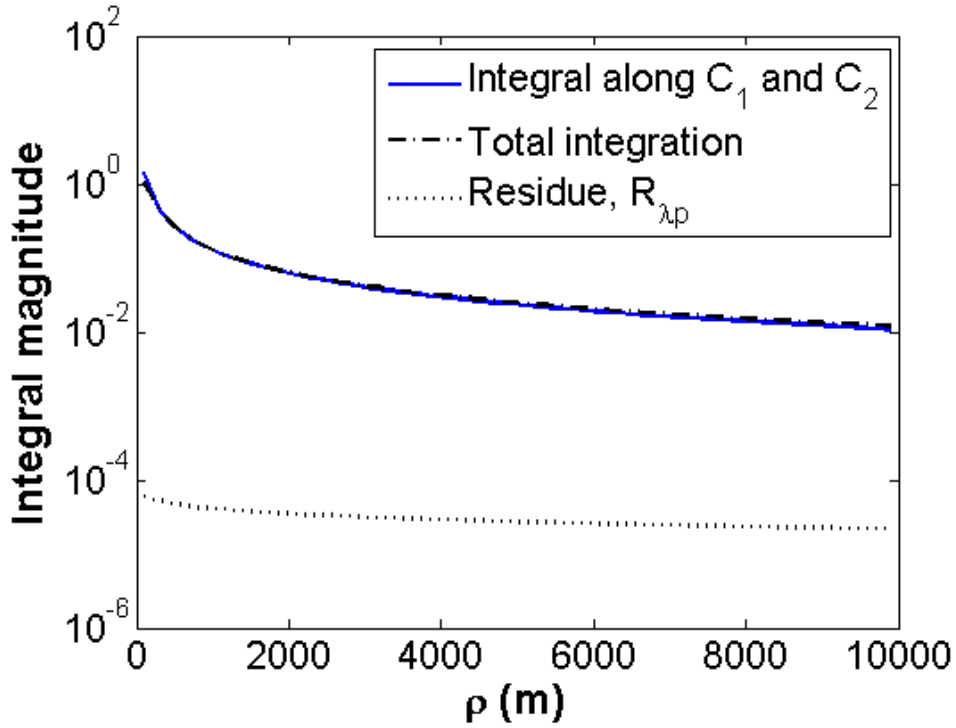

Fig. 6-7 Comparisons of magnitude between total integration, integration along branch cut of k_0, and the residue. (h = 20, z = -10)

Obviously, the integration along the branch cut of k_1 and the residue are so small that (6.39) has very good agreement with (6.38). Generally, (6.39) is valid when $h, z << \rho$, $|k_1| >> |k_0|$ and $|k_1\rho| >> 1$.

Since $\rho >> |h|, |z|$, the decay of the integrand along C_1 and C_2 is controlled by the value of $|\lambda\rho|$, the integral can be truncated at $|\lambda\rho| = 10$ and since we assume $|\lambda\rho| >> 1$

$$u_1 = (\lambda^2 - k_1^2)^{1/2} \approx jk_1 \tag{6.40}$$

With (6.40) the exponential term in (6.39) can be extracted from the integral, which leads to

$$I_{z1} \approx \frac{e^{jk_1(z-h)}}{2} \int_{C_1+C_2} g_2'(\lambda)\lambda H_0^{(2)}(\lambda\rho)d\lambda \tag{6.41}$$

Further since $|k_0\rho| << 1$ (i.e., quasi-static for $z > 0$), it is reasonable to assume that

$$u_0 = \pm(\lambda^2 - k_0^2)^{1/2} \approx \pm\lambda \tag{6.42}$$

because $|k_0|$ is very small compared to $|\lambda|$ over the largest portion of the integral. The approximations have been made here can be summarized as $\rho >> |h|$ and $|z|$, $|k_0\rho| << 1$, and $|k_1\rho| >> 1$. Now, if the approximations (6.40), (6.42) and $|\varepsilon'_1| >> |\varepsilon_0|$ are made in (6.36) then

$$g'_2(\lambda) \approx \frac{2(\varepsilon'_1)}{(\pm\lambda + jk_1)(\pm\varepsilon'_1\lambda)} = \frac{2}{\lambda^2 \pm jk_1\lambda}$$

If $g_2'^{(+)}(\lambda) = \dfrac{2}{\lambda^2 + jk_1\lambda}$ and $g_2'^{(-)}(\lambda) = \dfrac{2}{\lambda^2 - jk_1\lambda}$, represent $g'_2(\lambda)$ on the right side and left side of the branch cut of k_0, respectively, then the integral in (6.41) can be approximated as

$$I'_{z1} \approx \int_{C_1} \frac{2}{\lambda - jk_1} H_0^{(2)}(\lambda\rho)d\lambda + \int_{C_2} \frac{2}{\lambda + jk_1} H_0^{(2)}(\lambda\rho)d\lambda \tag{6.43}$$

Using the asymptotic approximation $H_0^{(2)}(\lambda\rho) \approx \sqrt{2j/(\pi\lambda\rho)} \cdot e^{-j\lambda\rho}$ for large $|\lambda\rho|$ (i.e., most of the integral), letting $\lambda = k_0 - js$, and changing the integral variable from λ to s, I'_{z1} finally becomes

$$I'_{z1} \approx 2\sqrt{\frac{2j}{\pi\rho}} \cdot e^{-jk_0\rho} \left[\int_0^\infty \frac{je^{-\rho s}ds}{\sqrt{k_0 - js}\,(k_0 - js - jk_1)} - \int_0^\infty \frac{je^{-\rho s}ds}{\sqrt{k_0 - js}\,(k_0 - js + jk_1)} \right] \tag{6.44}$$

Ignoring k_0 in both the denominators of the two integrands, which is reasonable because $|k_0|$ is very small compared to $|s|$ over most of the integral, I'_{z1} reduces to

$$I'_{z1} \approx -2j\sqrt{2/(\pi\rho)} \cdot e^{-jk_0\rho}(I_1 - I_2) \tag{6.45}$$

where $I_1 = \int_0^\infty \dfrac{e^{-\rho s}ds}{\sqrt{s}\,(s + k_1)}$ and $I_2 = \int_0^\infty \dfrac{e^{-\rho s}ds}{\sqrt{s}\,(s - k_1)}$. Therefore, the calculation of the complicated integral in (6.39) is reduced to the problem of evaluating the two

relatively simple integrals in (6.45). I_1 can be analytically evaluated as [64]

$$I_1 \approx \sqrt{\pi}\Big/\left(k_1\sqrt{\rho}\right)$$

Similarly for I_2

$$I_2 \approx -\sqrt{\pi}\Big/\left(k_1\sqrt{\rho}\right).$$

Therefore, the integral in (6.45) is

$$I'_{z1} \approx -4\sqrt{2}\,j\,\frac{e^{-jk_0\rho}}{k_1\rho}$$

The integral I_{z1} then can be approximated as

$$I_{z1} \approx -2\sqrt{2}\,j e^{jk_1(z-h)}\cdot\frac{e^{-jk_0\rho}}{k_1\rho} \tag{6.46}$$

It can be shown that (6.46) is approximately a factor of 1.4 larger than the exact result in (6.35) and that this difference is relatively stable over a wide range of parameters. Given this and the fact that an attempt to find a missing $\sqrt{2}$ factor did not succeed, a further study of the approximation used to derive (6.46) was carried out. This study indicated that the dominant part of the error resulted from the replacement of the Hankel function by its asymptotic expansion. Given this, a correction term can be written as

$$I_C \approx 2e^{-jk_0\rho}\int_0^B\left[\frac{1}{s-k_1}-\frac{1}{s+k_1}\right]\left[H_0^{(2)}(-j\rho s)e^{jk_0\rho}-\sqrt{\frac{-2}{\pi\rho s}}e^{-\rho s}\right]ds$$

Clearly most of the contribution to this integral comes from small values of ρs. Thus the integral is (somewhat arbitrarily) truncated at $\rho s = B = 0.3$ and the Hankel function is replaced by small argument expansion. Given this, the correction term is written as

$$I_C \approx 2e^{-jk_0\rho}\int_0^M\left[\frac{1}{s-k_1}-\frac{1}{s+k_1}\right]\left[1-\frac{2j}{\pi}\ln\left(\frac{-j1.781\rho s}{2}\right)-\sqrt{-2\Big/(\pi\rho s)}\right]ds \tag{6.47}$$

where inside the integral $e^{jk_0\rho} \approx e^{-\rho s} \approx 1$ and $M = B/\rho$. The integral in (6.47) can be analytically evaluated and the result is

$$I_C \approx I_{C1} + I_{C2} + I_{C3} \tag{6.48}$$

where

$$I_{C1} = c \cdot \ln\left(\frac{k_1 - B}{k_1 + B}\right) e^{-jk_0\rho}$$

$$I_{C2} = -\frac{8jB}{\pi k_1} e^{-jk_0\rho}$$

$$I_{C3} = 2je^{-jk_0\rho}\sqrt{\frac{-2}{\pi k_1 \rho}}\left[\ln\left(\frac{k_1 - B + 2j\sqrt{k_1 B}}{k_1 + B}\right) + j\ln\left(\frac{k_1 + B - 2j\sqrt{-k_1 B}}{k_1 - B}\right)\right]$$

$$c = 2\left[1 - \frac{2j}{\pi}\ln\left(\frac{-j1.781B\rho}{2}\right)\right].$$

I_{C1} and I_{C3} can be further simplified by expanding the natural logarithm function in Taylor series.

$$I_{C1} \approx -2c\frac{M}{k_1\rho}e^{-jk_0\rho} \quad \text{and} \quad I_{C3} \approx 8\sqrt{\frac{2}{\pi M}}\frac{jM}{k_1\rho}e^{-jk_0\rho}$$

The correction term is then rewritten as

$$I_C \approx \frac{jN}{k_1\rho}e^{-jk_0\rho} \tag{6.49}$$

where $N = M\left[-2c - 8/\pi + 8\sqrt{2/(\pi M)}\right]$ is a constant. It is interesting to note that the functional dependence of (6.49) is almost identical to that of (6.46). Hence adding (6.49) to (6.46) results in

$$I_{z1} \approx \frac{e^{jk_1(z-h)}}{2} \cdot \frac{je^{-jk_0\rho}}{k_1\rho}\left[-4\sqrt{2} + N\right] \tag{6.50}$$

which is identical to (6.46) except for the constant and that this constant is approximately 1/1.4 times the constant in (6.46) when M = 0.3 (i.e., $N \approx 1.72$). Then

(6.50) becomes

$$I_{z1} \approx -2je^{jk_1(z-h)} \cdot \frac{e^{-jk_0\rho}}{k_1\rho} \tag{6.51}$$

When h, $z << \rho$, $|k_1| >> |k_0|$ and $|k_1\rho| >> 1$, (6.51) approximates the exact integral very well. These conditions are roughly mapped to the following range of parameters: h, z < 100m, 100Hz < f < 3000Hz, 500m < ρ < 10000m and 0.001S/m < σ < 100S/m. The error of (6.51) compared to the exact integral of I_{z1} in (6.35) is less than 10% when 100Hz < f < 3000Hz and 500m < ρ < 10000m. Fig. 6-8 shows the comparisons of magnitude and phase angle between the approximation in (6.51) and the exact integral in (6.35), with dipole frequency of 1000Hz.

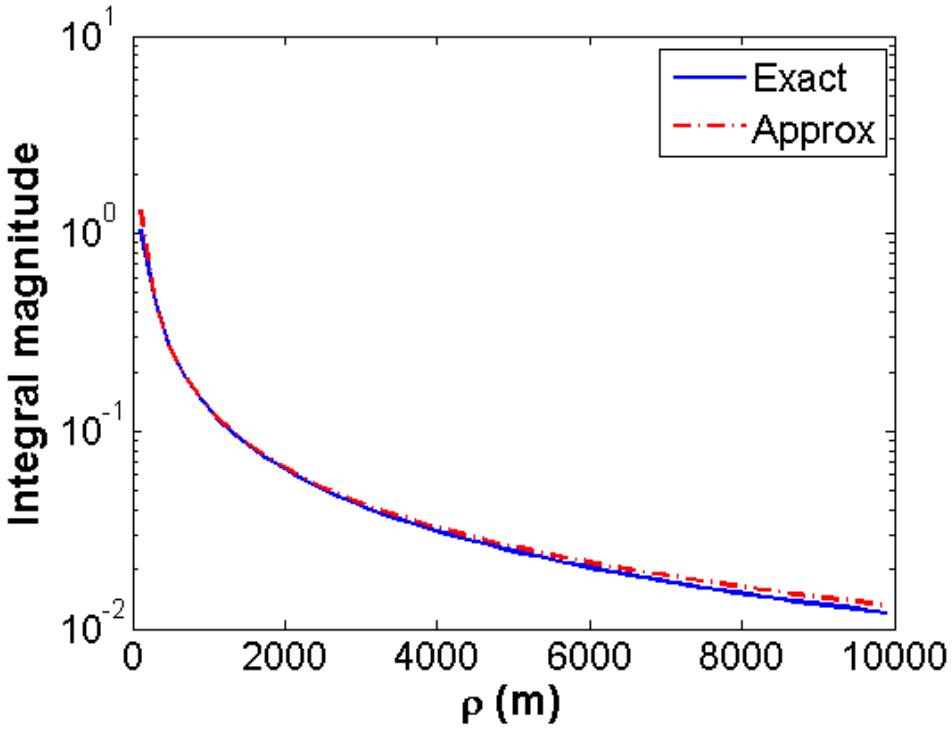

(a)

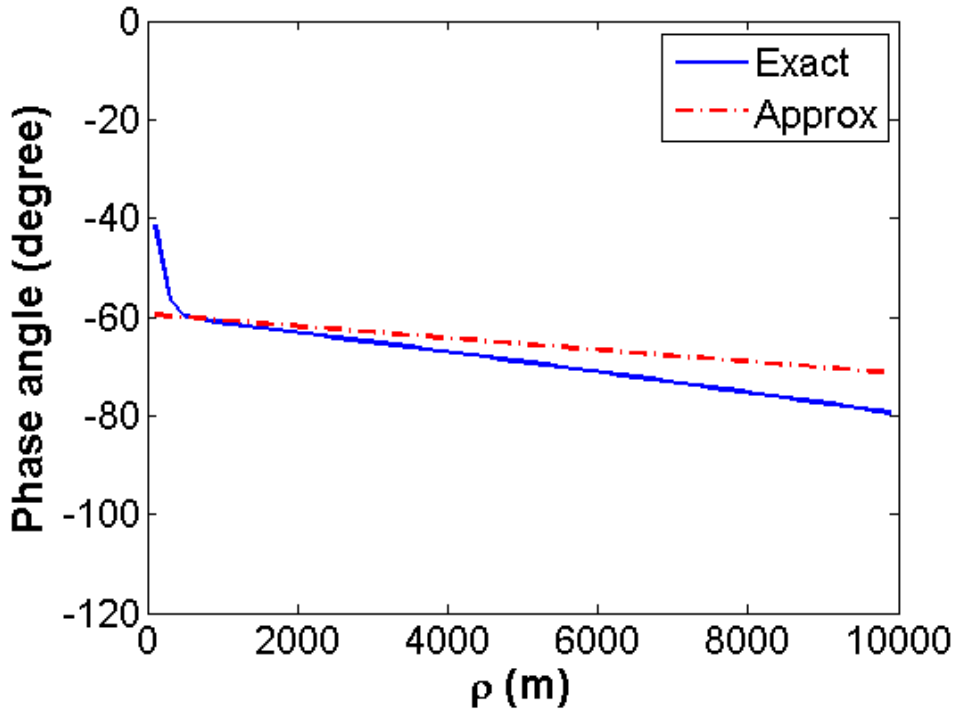

(b)

Fig. 6-8 Exact integral of I_{z1}, (6.35), vs. approximation, (6.51), f = 1000Hz: (a) magnitude, (b) phase angle.

This analysis is helpful for understanding the error incurred during the derivation of the approximation for (6.35). Further, the correction term significantly reduces the error and can be easily calculated. It is shown in (6.51) and can be used to derive simple results for the E and H fields. Therefore, (6.51) will be used as the approximation of I_{z1}.

For the integral of I_{y1} in (6.28), strategy for simplifying is the same as that used for I_{z1}. I_{y1} can be rewritten as

$$I_{y1} = \int_0^\infty f_2'(\lambda) e^{u_1(z-h)} \lambda J_0(\lambda\rho) d\lambda \tag{6.52}$$

where $f_2'(\lambda) = \dfrac{u_1 - u_0}{u_1 \cdot (u_0 + u_1)}$. The deformation of the integral contour is the same as that illustrated in Fig. 6-5 except that there is no pole in this case.

$$I_{y1} = \frac{1}{2}\int_{C_B} f_2'(\lambda) e^{u_1(z-h)} \lambda H_0^{(2)}(\lambda\rho) d\lambda$$

Again, using the argument that the integral along the branch cut of k_0 dominates the total integral, I_{y1} can be approximated as the sum of the integrals along C_1 and C_2

$$I_{y1} \approx \frac{1}{2}\int_{C_1+C_2} f_2'(\lambda) e^{u_1(z-h)} \lambda H_0^{(2)}(\lambda\rho) d\lambda \tag{6.53}$$

The approximations given in (6.40) and (6.42) still work and given these the function reduces to $f_2'(\lambda) \approx \frac{jk_1 \mp \lambda}{jk_1 \cdot (jk_1 \pm \lambda)}$. The change of signs in it is due to that u_0 takes different signs on the left and right sides of the branch cut of k_0. The integral in (6.53) becomes

$$I_{y1} \approx \frac{e^{jk_1(z-h)}}{2jk_1}\left[\int_{C_1} \frac{jk_1+\lambda}{jk_1-\lambda} \lambda H_0^{(2)}(\lambda\rho) d\lambda + \int_{C_2} \frac{jk_1-\lambda}{jk_1+\lambda} \lambda H_0^{(2)}(\lambda\rho) d\lambda\right]$$

Combining the two integrals on the right hand side results in

$$I_{y1} \approx \frac{e^{jk_1(z-h)}}{2}\int_{C_2} \frac{4\lambda^2}{k_1^2+\lambda^2} H_0^{(2)}(\lambda\rho) d\lambda .$$

Use the asymptotic approximation of Hankel function, the variable change $\lambda = k_0 - js$, and ignoring k_0's except in exponential terms, I_{y1} becomes

$$I_{y1} \approx 2\sqrt{\frac{2}{\pi\rho}} e^{jk_1(z-h)} e^{-jk_0\rho} \cdot I_3$$

where $I_3 = \int_0^\infty \frac{s^{3/2}}{s^2-k_1^2} e^{-\rho s} ds$. From the table of integrals [64], I_3 can be analytically evaluated and further simplified as $I_3 \approx -\frac{3\sqrt{\pi}}{4k_1^2} \cdot \frac{1}{\rho^{5/2}}$ and the integral I_{y1} is

$$I_{y1} \approx -\frac{3\sqrt{2}}{2k_1^2} e^{jk_1(z-h)} \frac{e^{-jk_0\rho}}{\rho^3} \tag{6.54}$$

Numerical calculations indicate that the approximation, (6.54), is approximately

6% larger in magnitude than the exact integral, (6.52). This error is relatively stable over the parameter range 100Hz < f < 3000Hz and ρ > 500m. Since the error is small for this case, it is not necessary to add a correction term to (6.54). Rather the factor of $3\sqrt{2}/4 \approx 1.06$ is simply set equal to 1 resulting in:

$$I_{y1} \approx -\frac{2}{k_1^2} e^{jk_1(z-h)} \frac{e^{-jk_0\rho}}{\rho^3} \tag{6.55}$$

Again, when h, $z << \rho$, $|k_1| >> |k_0|$ and $|k_1\rho| >> 1$, (6.55) approximates the exact integral (6.52) very well. Fig. 4 (a) and (b) give the comparisons of the magnitude and the phase angle between the exact integral of (6.52) and its approximation (6.55). For this case, the magnitude error of (6.55) is even less than 6% when ρ > 500m.

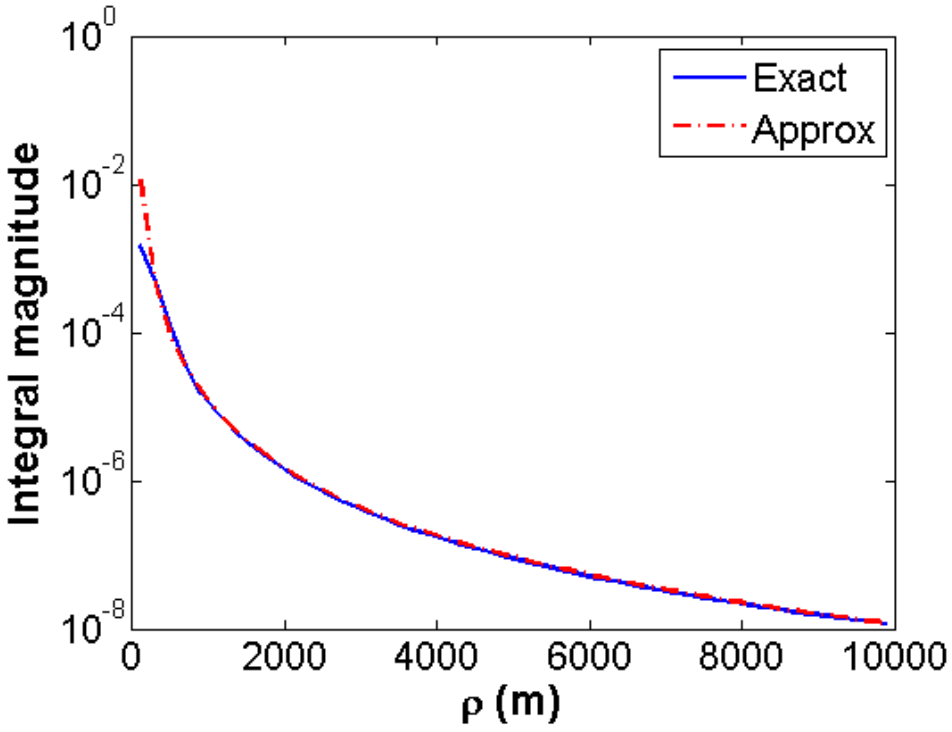

(a)

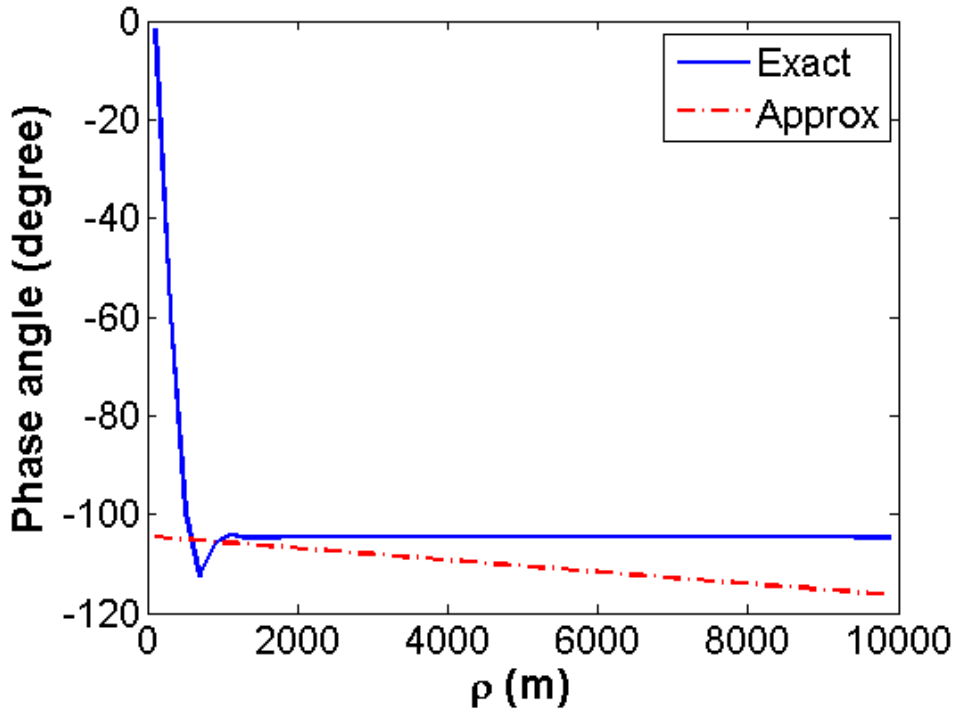

(b)

Fig. 6-9 Exact integral of I_{y1}, (6.52), vs. approximation, (6.55), f = 1000Hz: (a) magnitude, (b) phase angle.

6.3.2 Approximations for E and H fields

Given the approximations (6.51) and (6.55) for the integral portions of the vector potentials A_z^1 and A_y^1, respectively, the electromagnetic fields can be found by solving the Maxwell's equations. At any observation point P, (ρ, φ, z), in the lower conducting medium ($z < 0$), the total field is the combination of the incident field directly from the dipole and the reflected field due to the interface. The total E and H fields can be written as

$$E_x^1 = E_{xs}^1 + E_{xr}^1; \quad E_y^1 = E_{ys}^1 + E_{yr}^1; \quad E_z^1 = E_{zs}^1 + E_{zr}^1;$$
$$H_x^1 = H_{xs}^1 + H_{xr}^1; \quad H_y^1 = H_{ys}^1 + H_{yr}^1; \quad H_z^1 = H_{zs}^1 + H_{zr}^1;$$

where the components with 's' in the subscript refer to the source terms of the fields and those with 'r' in the subscript refer to the reflected fields. The source terms of the

fields are

$$E_{xs}^1 = A_1 \cdot \frac{e^{-jk_1R}}{R^3}\left(k_1^2R^2 - 3jk_1R - 3\right)\cdot \sin\phi\cos\phi \tag{6.56a}$$

$$E_{ys}^1 = A_1 \cdot \frac{e^{-jk_1R}}{R^3}\left[\left(-k_1^2R^2 + jk_1R + 1\right) + \left(k_1^2R^2 - 3jk_1R - 3\right)\cdot\left(\sin\phi\right)^2\right] \tag{6.56b}$$

$$E_{zs}^1 = A_1 \cdot \frac{(z+h)e^{-jk_1R}}{R^5}\left(k_1^2R^2 - 3jk_1R - 3\right)\cdot \sin\phi \tag{6.56c}$$

$$H_{xs}^1 = \frac{Idl}{4\pi}\cdot\frac{(z+h)e^{-jk_1R}}{R^3}\left(jk_1R + 1\right) \tag{6.56d}$$

$$H_{ys}^1 = 0 \tag{6.56e}$$

$$H_{zs}^1 = -\frac{Idl}{4\pi}\cdot\frac{e^{-jk_1R}}{R^3}\left(jk_1R + 1\right)\cdot\cos\phi \tag{6.56f}$$

where $A_1 = \dfrac{jIdl}{4\pi\omega\varepsilon_1'}$. The simplified reflected fields are

$$E_{xr}^1 \approx 2jA_1k_0^3\cdot e^{jk_1(z-h)}\frac{e^{-jk_0\rho}}{\left(jk_0\rho\right)^3}\left[3 + \frac{15}{\left(jk_1\rho\right)^2}\right]\cdot\sin\phi\cos\phi \tag{6.57a}$$

$$E_{yr}^1 \approx -2jA_1k_0^3\cdot e^{jk_1(z-h)}\frac{e^{-jk_0\rho}}{\left(jk_0\rho\right)^3}\left[2 + \frac{3-15\left(\sin\phi\right)^2}{\left(jk_1\rho\right)^2}\right] \tag{6.57b}$$

$$E_{zr}^1 \approx -\frac{6jA_1k_0^4}{k_1}\cdot e^{jk_1(z-h)}\frac{e^{-jk_0\rho}}{\left(jk_0\rho\right)^4}\cdot\sin\phi \tag{6.57c}$$

$$H_{xr}^1 \approx \frac{Idl\cdot k_0^3}{2\pi k_1}\cdot e^{jk_1(z-h)}\frac{e^{-jk_0\rho}}{\left(jk_0\rho\right)^3}\left[2 - 3\left(\sin\phi\right)^2\right] \tag{6.57d}$$

$$H_{yr}^1 \approx \frac{Idl\cdot k_0^3}{2\pi k_1}\cdot e^{jk_1(z-h)}\frac{3e^{-jk_0\rho}}{\left(jk_0\rho\right)^3}\cdot\sin\phi\cos\phi \tag{6.57e}$$

$$H_{zr}^1 \approx \frac{Idl\cdot k_0^4}{2\pi k_1^2}\cdot e^{jk_1(z-h)}\frac{3e^{-jk_0\rho}}{\left(jk_0\rho\right)^4}\cdot\cos\phi \tag{6.57f}$$

In the far field of the conducting medium (i.e., $|k_1\rho| >> h, z$), the incident field decays much faster than the reflected field, which suggests that the propagation

mechanism may involve some fields propagating in the low loss free space region. For the set of parameters considered previously the source term can be ignored beyond approximately 500m. The approximated reflected field E^1_{yr} given by (6.57) are compared to the total field calculated by the exact Sommerfeld integrals in Fig. 6-10. They match each other very well for about ρ > 500m. For the reflected magnetic field, similar result can be obtained.

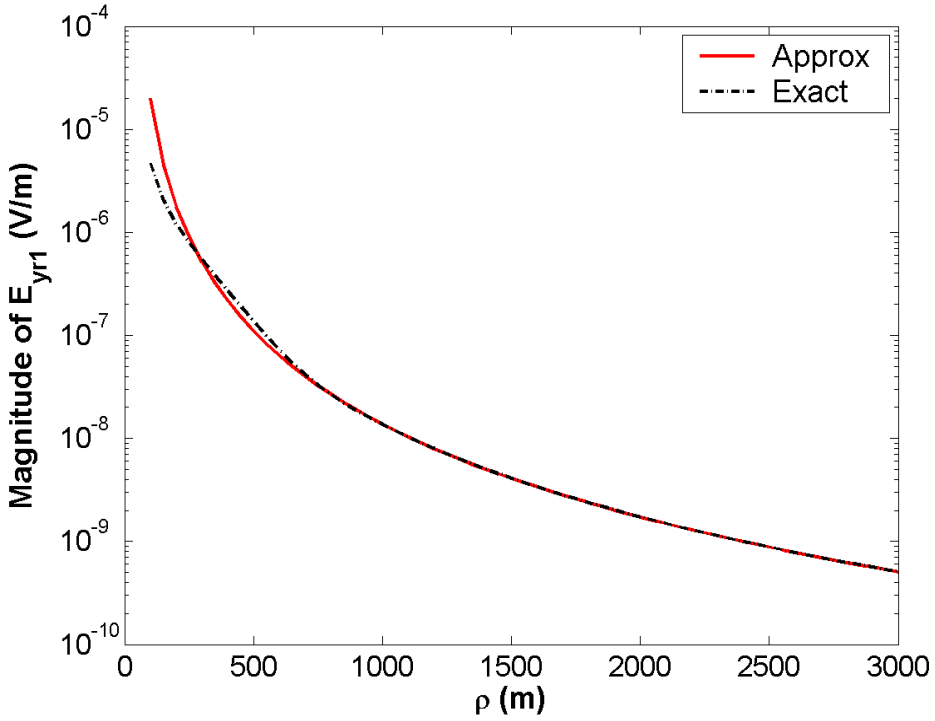

Fig. 6-10 Exact reflected field E^1_{yr} vs. its approximation (6.57b), $\varphi = \pi$.

6.3.3 Up-over-and-down interpretation of wave propagation near interface

In fact, the approximations (6.57a) – (6.57f) can be interpreted to have an up-over-and-down behavior, similar (but not identical) to the mechanism that has been studied in propagation of high frequency radio waves near a boundary [63]. The extremely low frequency (ELF) case is different because the fields in air are quasi-static. Here, some insight into this behavior will be given.

At the observation point P (ρ, φ, z), consider the E_x component, which is perpendicular to the HED's orientation and the easiest component to detect. As discussed, the total field can be approximated by the corresponding reflected field component in the far field (i.e., 6.57a). In the far field of the conducting medium the second term in the bracket is small compared to the constant '3' and can be ignored. Given this, the right hand side of (6.57a) can be rewritten as

$$E_x^1 \approx -\frac{3j\eta_1 Idl \cdot e^{-jk_1 h}}{2\pi k_1} \cdot \frac{e^{-jk_0\rho}}{\rho^3} \sin\phi \cos\phi \cdot e^{jk_1 z} \tag{6.58}$$

where η_1 is the intrinsic impedance of the conducting medium and $\eta_1 = (\mu/\varepsilon'_1)^{1/2}$.

For the up-over-and-down process as illustrated in Fig. 6-5, the field generated by the dipole (HED) first propagates upward (Part I) and crosses the interface into the free space region. Second, the wave spreads out horizontally (Part II) along the interface. Note that since the upper medium is free space and for the whole range of ρ considered here (i.e., 100 < ρ < 10,000m), $|k_0\rho| << 1$, the fields in free space are quasi-static. Finally, at the position on the interface right above P, the wave crosses the interface again and propagates vertically down (Part III) to the observation point.

To identify (6.58) as an up-over-and-down process, it is important to show how the different terms have functional dependencies that are characteristic to different portions of the process. For example, it will be shown that in the 'up' part of (6.58) corresponds to propagation in medium #1 and the effect of crossing the interface can be explained by image theory for dielectric-dielectric boundaries. To begin, it is helpful to show how a quasi-static field in the air can be excited by the buried HED.

Since it is assumed that $|k_1 h| << 1$, the fields near the interface are quasi-static and can be calculated using the electrostatic theory with charge dipole source as shown in Fig.6-11 (a). The dipole moment is *qdl* (C-m) where *q* is related to the current, *I*, of the original HED by

$$I = \frac{dq}{dt} = j\omega q \;\Rightarrow\; q = -jI/\omega \tag{6.59}$$

Image theory for static charges near a dielectric-dielectric interface can be used to find an expression for the electric field in the upper half space (air region). The lower region is replaced by free space and the charges replaced by equivalent charges at the same positions [65], as shown in Fig. 6-11 (b).

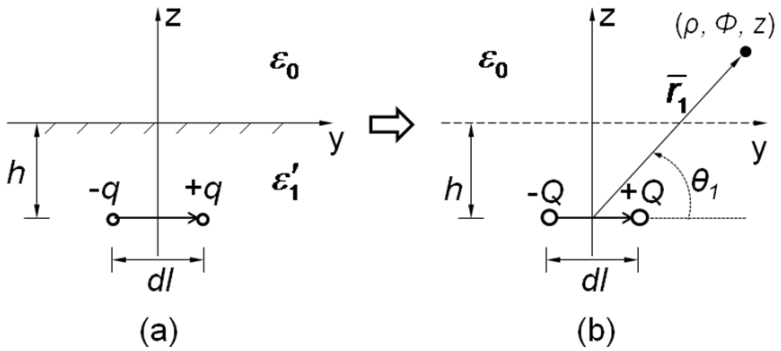

Fig. 6-11. (a) The static charge dipole replacing the HED and (b) the image of the static dipole.

The equivalent charges are [65]

$$Q = \frac{2\varepsilon_0}{\varepsilon_0 + \varepsilon_1'} \cdot q \tag{6.60}$$

and since $\varepsilon_0 << \varepsilon'_1$ (6.60) can be approximated by

$$Q = 2\varepsilon_0 q/\varepsilon_1' \tag{6.61}$$

The image charges form a new equivalent dipole with a moment *Qdl*, oriented in *+y* direction that can be used to find the fields in the upper free space region. Using (6.59) and (6.61) and known expressions for the fields of static dipoles, the electric field

above the interface ($z = 0$) can be found as

$$E_x = \frac{3\omega q dl \eta_1 e^{-jk_1 h}}{2\pi k_1} \cdot \frac{\rho^2}{r_1^5} \sin\phi \cos\phi \tag{6.62a}$$

$$E_y = \frac{\omega q dl \eta_1 e^{-jk_1 h}}{2\pi k_1} \cdot \frac{\left(2\rho^2 \sin^2\phi - \rho^2 \cos^2\phi - h^2\right)}{r_1^5} \tag{6.62b}$$

$$E_z = \frac{3\omega q dl \eta_1 e^{-jk_1 h}}{2\pi k_1} \cdot \frac{h\rho \sin\phi}{r_1^5} \tag{6.62c}$$

where $r_1 = (\rho^2 + h^2)^{1/2}$ and θ_1 is defined as shown in Fig. 6-11. Here, the factor $\exp(-jk_1h)$ has been included to account for the small attenuation between the HED and the surface and to correspond to (6.58). Equation (6.62) could be used to calculate the electric field anywhere in the upper region, but here, an alternative approach will be taken that leads more directly to an up-over-and-down interpretation for the field expression.

The field in (6.62) is used to find an equivalent surface charge directly above the source dipole and this will in turn be used to identify an equivalent source on the interface. The surface charge can be determined from the discontinuity of the normal electric flux density between the two sides of the interface [66], as shown in Fig. 6-12. The surface charge on the interface can be found by integrating the normal component of electric flux density, i.e., $\varepsilon_0 E_z$, over the whole interface (x-y plane)

$$q_s = \int_0^{2\pi} \int_0^{\infty} \varepsilon_0 E_z \rho d\rho d\phi \tag{6.63}$$

where E_z is given by (6.62c) and the much smaller electric field in the water is ignored.

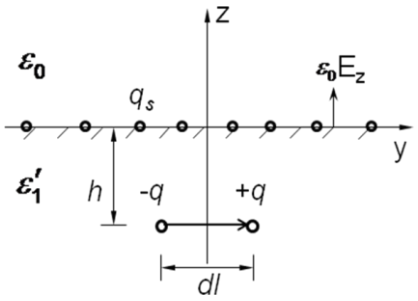

Fig. 6-12. Equivalent surface charges q_s on the interface ($z = 0$ plane).

Inserting (6.62c) into (6.63) results in

$$q_s = \frac{3\omega q dl \varepsilon_0 \eta_1 h e^{-jk_1 h}}{2\pi k_1} \int_0^{2\pi} \sin\phi d\phi \int_0^{\infty} \frac{\rho^2 d\rho}{\left(\rho^2 + h^2\right)^{5/2}} \tag{6.64}$$

Of course, (6.64) equals zero because the net surface charge over the whole interface is zero. But the equivalent dipole moment of this charge distribution is non-zero and determined by

$$P_S = \iint_{z=0\,\text{plane}} l_S dq_s \tag{6.65}$$

where P_S, Fig. 6-13 (a), is the moment of the equivalent dipole, l_S, Fig. 6-13 (b), is the distance between two equal and opposite infinitesimal surface charges at symmetrical positions about the x-axis. By using $l_S = 2\rho\sin\varphi$ and (6.62c), (6.65) can be rewritten as

$$P_S = \frac{3\omega q dl \varepsilon_0 \eta_1 h e^{-jk_1 h}}{2\pi k_1} \int_0^{2\pi} \int_0^{\infty} \frac{2\rho^3 \sin^2(\phi) d\rho d\phi}{\left(\rho^2 + h^2\right)^{5/2}} \tag{6.66}$$

This can be analytically evaluated [64] and (6.66) becomes

$$P_S = 2\omega q dl \varepsilon_0 \eta_1 / k_1 \tag{6.67}$$

Inserting (6.59) into (6.67) results in

$$P_S = -Idl \cdot (2j\varepsilon_0 \eta_1 / k_1) \tag{6.68}$$

From (6.68) it is clear that the moment of the equivalent dipole at the surface is just the moment of the original HED multiplied by a constant coefficient. The factor

of 2 is due to imaging of the equivalent dipole in the "nearly perfectly conducting" medium. Therefore, the 'up' (Part I in Fig. 6-5) part of the propagation process can be understood by noting that the fields from the original HED create an equivalent dipole just above the interface.

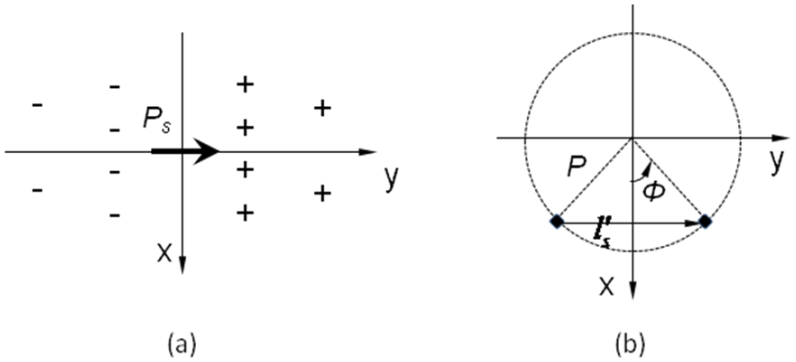

Fig. 6-13 (a) Nonuniform distribution of the equivalent surface charge on the interface (z = 0 plane); (b) geometry to find the moment of the dipole effect due to the surface charge.

The fields in free space region can be calculated by assuming that the equivalent dipole is in free space so that (on the z = 0 plane)

$$E_{x,u}^{0}(\rho,\phi,0)=\frac{3P_S\cdot e^{-jk_1h}e^{-jk_0\rho}}{4\pi\varepsilon_0\rho^3}\sin\phi\cos\phi \tag{6.69}$$

This is the 'over' (Part II in Fig. 6) part of the propagation process. Finally, the field in free space passes across the boundary with no attenuation due to the continuity of tangential electric fields. Then, since the field is approximately constant on the interface across a length much larger than the depth of P, the downward propagation must be approximately e^{jk_1z} (i.e., the 'down' part of the propagation). Finally, the expression of electric field component E_x at the observation point P is

$$E_{x,u}^{1}(\rho,\phi,z)=-\frac{3j\eta_1Idl\cdot e^{-jk_1h}}{2\pi k_1}\frac{e^{-jk_0\rho}}{\rho^3}\sin\phi\cos\phi\cdot e^{jk_1z} \tag{6.70}$$

which shows the complete up-over-and-down propagation. Equation (6.70) is identical to (6.58).

For a summary, in this chapter, the formulations for the electric and magnetic fields due to a low frequency HED buried in the middle layer of a three-layer medium are derived based on the Sommerfeld integrals. The results are validated analytically and numerically. Then, a method to simplify the Sommerfeld integrals for a HED buried near an interface between free space and a conducting half space is introduced (the lower two layers of the three-layer medium are reduced to half-space conducting medium for convenience of analysis). Using this method, a simple approximation for its electric fields in the conducting half space is obtained that is valid for distances that are electrically small in free space and electrically large in the conducting medium. The resulting approximation has been shown to be accurate within 10% over a wide range of parameters for which $h, z << \rho$, $|k_1| >> |k_0|$ and $|k_1\rho| >> 1$. Finally, the approximation can be interpreted as having up-over-and-down behavior for the propagation path from the conducting medium to free space and vice versa.

REFERENCES

[1] Richard S. Nichols, "The first electric power transmission line in North America-Oregon City, Oregon," *IEEE Industry Applications Magazine*, vol. 9, no. 4, pp. 7-10, July, 2003.

[2] U.S. Department of Energy report, Five-Year Program Plan for Fiscal Years 2008 to 2012 for Electric Transmission and Distribution Programs, August, 2006.

[3] S. Chakrabarti, E. Kyriakides, T. Bi, D. Cai, and V. Terzija, "Measurements get together," *IEEE Power & Energy Magazine*, vol. 7, no. 1, pp. 41-49, January, 2009.

[4] A. Phillips, "Staying in shape," *IEEE Power & Energy Magazine*, vol. 8, no. 2, pp. 27-33, March, 2010.

[5] A. Phillips, "Sensing the future," *IEEE Power & Energy Magazine*, vol. 8, no. 6, pp. 61-68, November, 2010.

[6] E. Fontana, S. C. Oliveira, *et al*., "Novel system for leakage current detection on insulator strings of overhead transmission lines," *IEEE Trans. on Power Del*., vol. 21, no. 4, pp. 2064-2070, October, 2006.

[7] S. C. Oliveira, E. Fontana, and F. J. M. M. Cavalcanti, "Leakage current activity on glass-type insulators of overhead transmission lines in the northeast region of Brazil," *IEEE Trans. on Power Del*., vol. 24, no. 2, pp. 822-827, April, 2009.

[8] S. Han, R. Hao, and J. Lee, "Inspection of insulators on high-voltage power transmission lines," *IEEE Trans. on Power Del*., vol. 24, no. 4, pp. 2319-2327, October, 2009.

[9] X. Chen, C. Li, X. Huang, and *et al*., "On-line estimating the level of hydrophobicity of composite insulators using the digital images," *Proc. Electrical Insulation Conf.*, pp. 216-221, 2005.

[10] J. Katrasnik, F. Pernus, and B. Likar, "A survey of mobile robots for distribution power line inspection," *IEEE Trans. on Power Del*., vol. 25, no. 1, pp. 485-493, October, 2010.

[11] Y. Kobayashi, G. G. Karady, G. T. Heydt, and R. G. Olsen, "The utilization of satellite images to identify trees endangering transmission lines," *IEEE Trans. on Power Del*., vol. 24, no. 3, pp. 1703-1709, July, 2009.

[12] W. Villiers, J. H. Cloete, L. M. Wedepohl, and A. Burger, "Real-time sag monitoring system for high-voltage overhead transmission lines based on power-

line carrier signal behavior," *IEEE Trans. on Power Del.*, vol. 23, no. 1, pp. 389-395, January, 2008.

[13] Silva J. M. and R. G. Olsen, "Use of Global Positioning System (GPS) Receivers Under Power Line Conductors." *IEEE Trans. on Power Del.*, vol. PWRD-17. pp. 938-944. October, 2002.

[14] S. S. Komaragiri and S. M. Mahajan, "A sag monitoring device based on a cluster of code based GPS receivers," Power & Energy Society General Meeting, PES '09, pp. 1-7, 2009.

[15] R. A. Leon, V. Vittal, and G. Manimaran, "Applications of sensor network for secure electric energy infrastructure," *IEEE Trans. on Power Del.*, vol. 24, no. 3, pp. 1703-1709, July, 2009.

[16] R. G. Olsen and K. S. Edwards, "A new method for real-time monitoring of high-voltage transmission-line conductor sag," *IEEE Trans. on Power Del.*, vol. 17, no. 4, pp. 1142-1152, October, 2002.

[17] R. G. Olsen, "Space potential probe for real-time monitoring of conductor sag and average core temperature," *North American Power Symposium*, 2004.

[18] W. L. Weeks, *Antenna Engineering*. NY: McGraw-Hill, Inc., 1968.

[19] EPRI, *Transmission Line Reference Book: 345 kV and Above*. Second Ed., Electric Power Research Institute, Palo, Alto, CA 1982.

[20] Pogorzelski. R. J. and D. C. Chang 1977. "On the Validity of the Thin Wire Approximation in Analysis of Wave Propagation Along a Wire Over a Ground," *Radio Science*, pp. 699-707, Sept./Oct.

[21] Wait, J. R. and K.P. Spies, "On the Image Representation of the Quasi-Static Fields of a Line Current Source Above Ground," *Canadian Journal of Physics*, Vol. 47, pp. 2731-2733, December, 1969.

[22] J. R. Wait, "Theory of Wave Propagation Along a Thin Wire Parallel to an Interface," *Radio Science*, Vol. 7, pp. 675-679, June 1972.

[23] D. C. Chang and R. G. Olsen, "Excitation of an infinite horizontal wire above a dissipative earth," *Radio Science*, vol. 10, pp. 823-831, August-September, 1975.

[24] E. F. Kuester, D. C. Chang and R.G. Olsen, "Modal Theory of Long Horizontal Wire Structures Above the Earth, 1, Excitation," *Radio Science*, vol. 13, pp.605-613, July, 1978.

[25] R. G. Olsen, E. F. Kuester and D. C. Chang, "Modal Theory of Long Horizontal Wire Structures Above the Earth, 2, Properties of Discrete Modes," *Radio Science*, Vol. 13, No. 4, pp. 615–623, July-August, 1978.

[26] R. G. Olsen and T. A. Pankaskie, "On the Exact, Carson and Image Theories for Wires at or Above the Earth's Interface," *IEEE Trans. on Power Apparatus and Systems*, Vol. PAS-102, pp. 769-774, March, 1983.

[27] R. G. Olsen, D. Deno, and R. S. Baishiki, "Magnetic fields from electric power lines – Theory and comparison to measurements," *IEEE Trans. on Power Del.*, Vol. 3, No. 4, pp 2127-2136, October, 1988.

[28] R. G. Olsen, J. L. Young, and D. C. Chang, "Electromagnetic Wave Propagation on a Thin Wire Above Earth", *IEEE Trans. on Antennas and Propagation*, vol. 48, no.9, pp. 1413-1419, December 1984.

[29] A. Ramirez and F. Uribe, "A broad range algorithm for the evaluation of Carson's integral," *IEEE Trans. on Power Del.*, Vol. 22, No. 2, pp 1188-1193, April, 1992.

[30] J. C. Salari, A. Mpalantinos, and J. I. Silva, "Comparative analysis of 2- and 3-D methods for computing electric and magnetic fields generated by overhead transmission lines," *IEEE Trans. on Power Del.*, vol. 24, no. 1, pp. 338-344, January, 2009.

[31] A. Z. E. Dein, M. A. A. Wahab, *et al.*, "The effect of the span configurations and conductor sag on the electric-field distribution under overhead transmission lines," *IEEE Trans. on Power Del.*, vol. 25, no. 4, pp. 2891-2902, October, 2010.

[32] A. E. Tzinevrakis, D. K. Tsanakas, and E. I. Mimos, "Analytical calculation of the electric field produced by single-circuit power lines," *IEEE Trans. on Power Del.*, vol. 11, no. 3, pp. 1571-1576, July, 1996.

[33] A. V. Mamishev, R. D. Nevels, and B. D. Russell, "Effects of conductor sag on spatial distribution of power line magnetic field, "*IEEE Trans. on Power Del.*, vol. 23, no. 3, pp 1495-1505, January, 2008.

[34] A. Z. E. Dein, "Magnetic-field calculation under EHV transmission lines for more realistic cases," *IEEE Trans. on Power Del.*, vol. 24, no. 4, pp. 2214-2222, October, 2009.

[35] R. G. Olsen and P. S. Wong, "Characteristics of low frequency electric and magnetic fields in the vicinity of electric power lines", *IEEE Trans. on Power Del.*, vol. 7, no. 4, pp 2046-2055, October, 1992.

[36] R. G. Olsen, "Power-transmission electromagnetic", *IEEE Antennas and Propagation Magazine*, Vol. 36, No. 6, December, 1994.

[37] J. R. Wait and K. P. Spies, "On the image representation of the quasi-static fields of a line current source above ground," *Canadian Journal of Physics*, vol. 47, pp. 273 1-2733, December, 1969.

[38] R. F. Harrington, *Introduction to Electromagnetic Engineering*. New York: Dover Publications Inc., 2003.

[39] W. R. Smythe, *Static and Dynamic Electricity*. NY: McGraw-Hill, 1968.

[40] R. P. Winch, *Electricity and Magnetism*. New Jersey: Prentice-Hall, 1957.

[41] C. A. Balanis, *Advanced Engineering Electromagnetics*. NJ: John Wiley & Sons, Inc., 1989.

[42] C. R. Paul, *Introduction to Electromagnetic Compatibility*. NJ: John Wiley & Sons, Inc., 1992.

[43] J. J. Goedbloed, "Reciprocity and EMC Measurements", network resource: http://www.ieee.org/organizations/pubs/newsletters/emcs/summer03/jasper.pdf

[44] K. F. Sander and G. A. Reed, *Transmission and Propagation of Electromagnetic Waves*. Cambridge: Cambridge University Press, 1986.

[45] R. G. Olsen, "An Improved Model for the Electromagnetic Compatibility of All-Dielectric Self-Supporting Fiber-Optic Cable and High-Voltage Power Lines", *IEEE Transaction on Electromagnetic Compatibility*, Vol. 41, No. 3, pp. 180-192, August 2002.

[46] A. A. Smith, *Coupling of External Electromagnetic Fields to Transmission Lines*. NJ: John Wiley & Sons, Inc., 1977.

[47] J. R. Harvey, "Effect of Elevated Temperature Operation on the Strength of Aluminum Conductors", *IEEE Transactions on Power Apparatus and Systems*, Vol. PAS-91, No. 5, pp.1769-1772, September 1972.

[48] Vincent T Morgan, "Effect of elevated temperature operation on the tensile strength of overhead conductors", *Trans. on Power Del.*, Vol. 11, No. 1, pp. 345-352, January 1996.

[49] M. Keshavarzian and C. H. Priebe, "Sag and Tension Calculations for Overhead Transmission Lines at High Temperatures—Modified Ruling Span Method", *IEEE Trans. on Power Del.*, Vol. 15, No. 2, April 2000.

[50] L. Makkonen, "Modeling Power Line Icing in Freezing Precipitation", *7th International Workshop on Atmospheric Icing of Structures*, 1996, Canada. 1952200.

[51] C. Meng and Y. Cheng, "A New Ice Covering Model", *2008 International Conference on High Voltage Engineering and Application*, Chongqing, China, November, 2008.

[52] M. W. Tuominen and R. G. Olsen, "Electrical Design Parameters of All-Dielectric-Self-Supporting Fiber Optic Cable", IEEE Transaction on Power Delivery, Vol. 15, No. 3, pp. 940-947, July 2000.

[53] Internet resource, http://www.answers.com/topic/directional-coupler

[54] G. Metzger and J. Vabre, *Transmission Lines With Pulse Excitation*. NY: Academic Press, 1969.

[55] Biddle Instruments, *Getting Down to Earth: Manual on Earth-Resistance Testing for the Practical Man*, Fourth Edition, 1982.

[56] E. R. Sverko, "Ground measuring techniques: electrode resistance to remote earth & soil resistivity**",** online resource:

[57] A. Baños, *Dipole radiation in the presence of a conducting half-space*. New York: Pergamon, 1966.

[58] P. R. Bannister, "Extension of finitely conducting earth-image-theory results to any range", Naval Underwater Systems Center, New London, CT, Tech. Rep., Jan. 1984.

[59] J. R. Wait and L. L. Campbell, "The fields of an oscillating magnetic dipole immersed in a semi-infinite conducting medium", *J. Geophys. Res*., vol. 58, no. 2, pp. 167-178, 1953.

[60] A. K. Sinha and P. K. Bhattacharya, "Vertical magnetic dipole buried inside a homogeneous earth", *Radio Sci.*, vol. 1, no. 3, pp. 379-395, 1966.

[61] J. R. Wait, "The electromagnetic fields of a horizontal dipole in the presence of a conducting half-space", *Can. J. Phys.*, vol. 39, no. 7, pp. 1017-1028, 1961.

[62] R. L. Burden and J. D. Faires, *Numerical Analysis*. MA: Brooks/Cole, 7th edition, 2000.

[63] T. Tamir, "Radio wave propagation along mixed paths in forest environments", *IEEE Trans. Antennas Propagat.*, vol. 25, no. 4, pp. 471-477, Jul. 1977.

[64] I. S. Gradshteyn and I. M. Ryzhik, *Table of integrals series and products*. New York: Academic Press, 1965.

[65] E. D. Torre and C. V. Longo, *The Electromagnetic Field*. Boston: Allyn and Bacon, Inc., 1969.